Université de Neuchâtel
Institut de Physique

Unusual Aspects of Surface Electronic Structure studied with Photoelectron Spectroscopy

Travail de thèse présenté à l'Institut de Physique de l'Université de Neuchâtel pour l'obtention du titre de "docteur ès sciences".

Matthias Hengsberger

Neuchâtel, janvier 2000

IMPRIMATUR POUR LA THÈSE

Unusual Aspects of Surface Electronic Structure studied with Photoelectron Spectroscopy

de M. Matthias Hengsberger

UNIVERSITÉ DE NEUCHÂTEL

FACULTÉ DES SCIENCES

La Faculté des sciences de l'Université de Neuchâtel sur le rapport des membres du jury,

MM. Y. Baer (directeur de thèse), H. Beck,
D. Malterre (Uni. Nancy F) et
S. Hüfner (Uni. Saarbrücken D)

autorise l'impression de la présente thèse.

Neuchâtel, le 22 février 2000

Le doyen:

J.-P. Derendinger

This work is dedicated to
Cynthia and Lucas.

Abstract

In the present thesis, the surface electronic structure of several metals has been studied by means of angle-resolved photoelectron spectroscopy. The spectrometer set up by the group of Prof. Yves Baer reaches an unprecedented energy resolution of 5 meV, which allows the low-energy excitations, responsible for the thermodynamic properties, to be observed.

The thesis has three main chapters:

- The first chapter concerns the (111)-surfaces of the semimetals bismuth and antimony. Due to their peculiar electronic structure, these two elements allow the influence of dimensionality on the excitation spectra to be studied in mesoscopic dimensions. The goal of this work has been to check whether the conduction bands were observable in photoemission spectra, and whether the surface electron structure corresponded to that of the bulk. An experimental study of bismuth represents a challenge, since the band width of the electron band and the overlap between electron and hole bands are of the order of 20-30 meV. In the case of bismuth, strong deviations of the surface electronic structure with respect to that of the bulk have followed from the results of our measurements. The changes are probably due to a relaxation of the atoms in the outermost layers. The influence of the surface has therefore to be taken into account, if one were to study the electronic behaviour in low dimensions. On the other hand, antimony is the more promising element for such experiments since the observed electronic structure of the surface agrees with bulk band structure calculations. Moreover, the occupied width of the electron band, much larger in antimony than in bismuth, facilitates the observation of electronic excitations.

- In the second experiment, the behaviour of a surface state, submitted to an array of equidistant steps, has been studied. Such an arrangement of steps is produced by miscut of a sample surface with respect to a low-index crystalline plane. In our case, the surface employed is vicinal to the (100)-face of copper. It exhibits a regular array of (100)-oriented terraces separated by monatomic steps. Our aim has been to observe the behaviour of a surface state confined within the terraces owing to repulsion of the electrons by the potential perturbation at the step edges. The findings of this experiment show that the step potential represents a rather permeable barrier allowing the electrons on adjacent terraces to couple. The surface state dispersion on the vicinal surface reflects the reciprocal lattice of the superstructure, giving evidence for only partial localisation of the electrons. The behaviour can be analyzed within the framework of the Kronig-Penney-model or within a tight-binding approach. As a result, the observed energy shift of the surface state peak is due to the potential perturbation,

depending on the width of the terraces. Consequently, the measured peak broadening can be explained by an integration of contributions from terraces of different sizes.

- The last chapter covers the influence of electron-phonon coupling on surface state electrons. The nearly free-electron-like surface state on the (0001)-face of beryllium was known to show some exceptional behaviour near the Fermi surface. Owing to our photoemission measurements, we have been able to show the strong coupling to phonon modes to be at the origin of this behaviour. The unique lineshape and its exceptional evolution near the Fermi surface have been experimentally observed for the first time. Based on calculations, carried out some decades ago, a simple model has been developed and the results have been compared to the experimental spectra. The agreement between theory and experiment is excellent. Beside the electron-phonon coupling parameters, this model yields an estimation of the strength of electronic correlations and of the defect concentration of the sample surface.

Résumé

Dans le cadre de ce travail de thèse, la structure électronique de différentes surfaces métalliques a été étudiée à l'aide de la photoémission angulaire. Le spectromètre mis au point par le groupe du Prof. Yves Baer, qui atteint une résolution en énergie sans précédent de 5 meV, a permis d'observer les excitations de basse énergie, c'est-à-dire les excitations électroniques responsables des propriétés thermodynamiques des matériaux.

La thèse se divise en trois chapitres distincts:

- Le premier concerne les surfaces (111) des semi-métaux bismuth et antimoine. En raison de leurs structures électroniques particulières, ces deux éléments permettent une étude, à l'échelle mésoscopique, des effets de dimensionalité sur le spectre d'excitations. Le but de ce travail était de vérifier si les bandes de conduction étaient observables par photoémission et si la structure électronique de la surface représentait celle du volume. Dans le cas du bismuth, ceci représente un défi sur le plan expérimental puisque la largeur de bande occupée par les électrons conducteurs ainsi que le recouvrement entre la bande des électrons et celle des trous sont de l'ordre de 20-30 meV. Les mesures ont démontré que la dispersion des électrons et des trous dans la surface déviait fortement de celle du volume. Ce changement est très probablement dû à une relaxation des atomes formant les couches extérieures du cristal. Dans une étude du comportement électronique dans un système à basse dimension, il serait donc nécessaire de tenir compte de l'influence de la surface. Pour une telle expérience, l'antimoine s'est révélé plus prometteur que le bismuth. En effet, la structure électronique observée correspond aux calculs de bandes pour le cristal volumique, et sa largeur de bande, dix fois plus grande que celle du bismuth, facilite l'observation des excitations électroniques.

- La deuxième expérience a consisté à mesurer le comportement d'un état de surface perturbé par une superstructure en escalier d'atomes. En coupant un cristal de cuivre en biais par rapport au plan (100), on obtient une face "vicinale" qui peut être imaginée comme un arrangement de terrasses (100) régulières, séparées par des marches équidistantes d'une hauteur correspondant à la distance inter-atomique. Le but était d'observer le confinement d'un état de surface dans les terrasses, conséquence de la répulsion des électrons par les barrières de potentiel formées par le ré-arrangement de la charge libre près des marches. Les résultats obtenus dans cette expérience démontrent que les électrons localisés dans des terrasses voisines communiquent à travers ces barrières partiellement perméables. La dispersion de l'état de surface reflète le nouveau réseau réciproque imposé par la superstructure. La localisation des électrons n'est donc que partielle. Le comportement des électrons soumis à un tel arrangement de barrières peut être analysé dans le cadre du modèle de Kronig-Penney ou d'un

modèle des liaisons fortes ("tight-binding"). Il apparaît que le déplacement en énergie du pic observé est la conséquence de la perturbation du potentiel de surface et qu'il dépend de la largeur moyenne des terrasses. De surcroît, l'élargissement du pic dans les spectres de photoémission s'explique non pas par une hybridation avec les états du volume, mais par une intégration des contributions provenant des terrasses de largeurs différentes.

- Dans le dernier chapitre, l'effet du couplage entre électrons et phonons, a été étudié. Il est connu que, près de la surface de Fermi, l'état de surface quasi libre de la face (0001) du béryllium a un comportement exceptionel. Or, grâce à nos mesures de photoémission, il a été possible de conclure que ce comportement etait la conséquence d'un couplage fort entre électrons et phonons. La forme de ligne unique et son évolution pour des vecteurs d'onde proches de la surface de Fermi ont été observées expérimentalement pour la première fois. Des calculs effectués il y a déjà plusieurs décennies ont permis de développer un modèle simple et de comparer les résultats aux spectres expérimentaux. La comparaison qualitative et quantitative entre calculs et mesures est plus que satisfaisante. En plus des informations concernant le couplage électron-phonon, ces calculs fournissent des paramètres qui permettent une estimation des interactions entre les électrons d'une part, et la densité de défauts présents à la surface du réseau cristallin d'autre part.

Contents

List of Acronyms iv
Notation of Frequently Used Symbols v

1 Introduction: Photoemission on Low-Dimensional Metals **1**

2 Photoemission and Spectral Functions **5**
2.1 Angle-Resolved Photoemission 5
2.2 Landau's Concept of Interacting Fermions 8
2.3 Many-Body Effects 11

3 Experimental Setup **17**
3.1 The Vacuum System 17
3.2 The Preparation Chamber 19
3.2.1 Sample Preparation: Generalities 19
3.2.2 Low-Energy Electron Diffraction (LEED) 20
3.2.3 Auger Electron Spectroscopy (AES) 21
3.3 The Spectrometer 22
3.3.1 The x-Ray Source 23
3.3.2 The vuv-Lamp 24
3.3.3 The vuv-Monochromator 25
General Setup of the Monochromator 25
Optical Properties 26
Measured Characteristics of the Monochromator 28
3.3.4 The Electron Analyser 31

4 The Surface Electronic Structure of the Group-V Semimetals **35**
4.1 Motivation: One-Dimensional Metal in Mesoscopic Dimensions 35
4.2 Why Bismuth and Antimony? 36
4.3 Bulk Properties 37
4.3.1 Lattice and Brillouin Zone 37

4.3.2 Bulk Electronic Structure 40
4.4 Preparation of the Single Crystals 43
4.5 Bi(111) 46
4.5.1 Valence Band Structure 46
4.5.2 Electrons 49
4.5.3 Temperature Dependence 51
4.5.4 Holes 53
4.5.5 Surface Electronic Structure of Bi(111) 55
4.6 Sb(111) 57
4.6.1 Valence Band Structure 58
4.6.2 Electrons 60
4.6.3 Holes 62
4.6.4 Surface Electronic Structure of Sb(111) 66
4.7 Bismuth and Antimony in Mesoscopic Dimensions 66

5 Step Potentials on Vicinal Surfaces: Barriers for Surface States 67
5.1 Short Review of Surface States and Goal of our Experiment 67
5.2 Surface Mesh and Brillouin Zone 69
5.3 Sample Preparation and LEED Analysis 70
5.4 Interfering Electron Waves 72
5.5 The $\overline{\text{M}}$-Tamm State on Cu(100) 74
5.6 Dispersion Parallel and Perpendicular to the Step Edges: Cu(610) 76
5.7 Lineshape Analysis and Comparison to Cu(811) 81
5.8 Summary: Superlattice Effects 83

6 Electron-Phonon Coupling: Be(0001) 85
6.1 Beryllium Bulk Properties 85
6.2 The "Specimen": Exotic Behaviour at E_F 87
6.3 Sample Preparation 90
6.4 Experimental Results 91
6.5 Comparison of the Spectra with Calculations 97
6.6 Different Approach, Discrepancies, and Improved Calculations 104
6.7 Summary: Electron-Phonon Coupling in Two Dimensions 107

Appendices 109

A Spectral Functions and Finite Temperature 109

B Example Calculation of a Photoemission Spectrum 111

List of Acronyms

AES	Auger Electron Spectroscopy
ARUPS	Angle-Resolved Ultraviolet Photoemission Spectroscopy
bcc	Body-Centered Cubic (lattice)
BIS	Bremstrahlung-Isochromat Spectroscopy
BZ	Brillouin Zone
D	Dimension(al)
DOS	Density Of States
ECR	Electron Cyclotron Resonance
ENP	Ellipsoidal Non-Parabolic (model)
ESCA	Electron Spectroscopy for Chemical Analysis
fcc	Face-Centered Cubic (lattice)
FL	Fermi-Liquid
FS	Fermi Surface
FSM	Fermi Surface Mapping
FWHM	Full Width at Half Maximum
HeI, HeII, ...	excitation lines of He
hcp	Hexagonal Close Packed (structure)
LEED	Low-Energy Electron Diffraction
MCP	Multi-Channel Plate
ML	Mono-Layer
NFE	Nearly-Free Electron (like)
PE	Photoemission
PES	Photoelectron Spectroscopy/Spectrum
PID	Proportional-Integral-Differential (controler)
QP	Quasi-Particle
QSE	Quantum Size Effects
SBZ	Surface Brillouin Zone
sc	Simple Cubic (lattice)
SCLS	Surface Core Level Shift
SPALEED	Spot-Profile Analysis in Low-Energy Electron Diffraction
STM	Scanning Tunneling Microscopy
UPS	Ultraviolet Photoemission Spectroscopy
vuv	Vacuum UltraViolet (radiation)
XPS	X-ray Photoemission Spectroscopy

Notation of Frequently Used Symbols

$\mathbf{A}_{(s,p)}$	Vector potential of the light subscript s refers to $\mathbf{A}$ being perpendicular to the mirror plane, p to $\mathbf{A}$ lying within the mirror plane
$A(\omega, \mathbf{k})$	Spectral function at energy ω and wave vector $\mathbf{k}$
$\alpha^2F(\tilde{\omega})$	Eliashberg function at phonon energy $\tilde{\omega}$
E_B	binding energy (with respect to E_F)
E_F	Fermi energy
$\varepsilon(\mathbf{k})$	band energy at wavevector $\mathbf{k}$ (independent electron approximation)
E_{kin}	kinetic energy
$f(\omega, T)$	Fermi-Dirac distribution function at energy ω and temperature T
$G(\omega, \mathbf{k})$	Green's function at energy ω and wave vector $\mathbf{k}$
γ	inverse lifetime (width of lorentzian)
Γ, L, X, N, ...	symmetry points of the bulk Brillouin zone
$\overline{\Gamma}$, $\overline{\mathrm{M}}$, ...	symmetry points of the surface Brillouin zone
h, $\hbar$	Planck's constant
k_B	Boltzmann's constant
$h\nu$	photon energy
k_F	Fermi momentum
$k_\parallel$	momentum component parallel to the surface
$k_\perp$	momentum component perpendicular to the surface
λ	wave length or average electron-phonon coupling strength
λ_{mfp}	electron mean free path
m_0	Free electron rest mass
m^*	effective mass
μ	chemical potential
σ	standard deviation or width of a gaussian
$\Sigma(\omega, \mathbf{k})$	self-energy at energy ω and wave vector $\mathbf{k}$
T	absolute temperature
τ	lifetime (of a quasi-particle)
Θ, φ	photoelectron emission angles
V_{ee}, $V_{e\varphi}$	coupling matrix element (electron-electron or electron-phonon)
$v_{(F)}$	group velocity (at the Fermi surface)
ω	energy with respect to E_F ($\hbar$ is often omitted)
$\tilde{\omega}$	phonon energy ($\hbar$ is often omitted)

Chapter 1

Introduction: Photoemission on Low-Dimensional Metals

One of the most fundamental tasks of the modern theory of metals is to establish a link between their properties and their electronic structure. Important properties are the electrical conductivity, heat capacity, susceptibilities, to note only a few. Of particular interest are metals which exhibit strong anisotropies in conductivity, so-called low-dimensional metals. These metals were first essentially of theoretical interest, because they often allow given problems to be solved analytically. However, the discovery of real low-dimensional organic and inorganic conductors in line with the miniaturization in the technological sector renewed the interest in the last decades.
Surface states are the main subject of the present thesis. Different "unusual aspects" will be presented in this work, as the electron-lattice interaction and the influence of superstructure and surface atom relaxation on electronic properties. Surface states are localized in the topmost layers of a crystal and possess by nature only two degrees of freedom. They constitute therefore a valuable object in the study of electronic correlations in low dimensions.

Due to the fermionic character of the electrons, quantum theory implies that the electrons, whose energies are close to the Fermi energy E_F on the scale of the temperature k_BT, mainly determine the characteristics of a metal [1]. Hence, the understanding of the macroscopic properties requires knowledge of the low-energy excitations. In non-interacting systems the electronic excitation spectrum can be directly deduced from the energy vs momentum relation $\varepsilon(\mathrm{k})$ and the density of states (DOS). An extension of this concept of independent particles to real metals fails if the correlations between the electrons or the interaction with lattice vibrational modes become important. In order to account for interactions, Landau introduced the concept of quasi-particles (QP), which may be seen as bare particles (electrons or holes) *dressed* by a cloud of low-energy excitations of the interacting system [2]. A gas of QPs is usually called Fermi-liquid, and its excitations are in one-to-one-correspondence to those of a non-interacting system [3–5]. The achievements of the QP-description in its

application to simple metals, like e.g. the alkalis and the noble metals, allow the one-particle description to be recovered in many cases despite the presence of many-body effects [6]. Due to the interactions, the effective mass m^* and the spectral weight Z of the QPs are renormalized with respect to the corresponding properties of the non-interacting electron gas. If the interactions are weak, the renormalization can be calculated using perturbation theory. Collective excitations will appear in the excitation spectra as a consequence of the interactions [7,8]. The coupling to phonons and the electron-electron correlation determine the quasi-particle dispersion close to the Fermi energy. The investigation of these effects is part of the present thesis.

With increasing correlation strength, the QP contribution Z to the excitation spectra decreases, and the Fermi-liquid model reaches its formal limit of validity in the case $Z = 0$. Surprisingly, most Heavy Fermion systems can be considered as Fermi liquids despite the presence of strong electronic interactions [9]. The most spectacular breakdown of the QP-concept may be expected to occur in one-dimensional (1D) metals. In such metals, the electronic response to a perturbation exhibits singularities at momenta 0 and $2k_F$ (k_F = Fermi momentum), which cause instabilities of the electron gas [10,11]. Such an interacting 1D electron gas is commonly called a Luttinger liquid. The low-energy excitation spectrum consists solely of collective excitations [12]. A description of the properties and excitation spectra is beyond the scope of this work and can be found in numerous articles, e.g. the reviews given in Refs. [13,14]. Experimental evidence for Luttinger-liquid behaviour is difficult to obtain, and most results are still subject of controversial discussion [15–22]. The main problems are the sample quality and effects of the cleavage, which is difficult to control. More convincing spectroscopic evidence of such behaviour could therefore only be observed very recently [23] from artificial atomic chains. For these reasons, one of the chapters of this thesis is dedicated to the search of a suitable material for the study of 1D localization in mesoscopic dimensions.

Photoemission is the most suitable tool to look at electronic correlations, since it gives direct access to the spectral function, an important property of interacting electrons. Moreover, in low-dimensional systems the crucial parameters *energy* and *momentum* are exactly defined by experiment. Modern electron analysers reach a resolution in energy and angle, which allows to measure very accurately the dispersion of low-energy excitations in the region around the Fermi energy, where correlations play a dominant role. Using photoemission, one can therefore follow the evolution of the electronic behaviour with increasing correlation strength and in low dimensions [18,24,25].

The present thesis is organized as follows: after a short introduction to the theory and the presentation of the experimental setup, the experimental results are shown and analysed in three chapters. The first one deals with the characterization of the semi-metallic band structures of bismuth and antimony. These materials are candidates for 1D-metals in mesoscopic dimensions. Vicinal copper surfaces are studied in the second part. Goal of this experiment

was to observe 1D localization of surface state electrons on an atomic length scale. The confining potential is produced by a superstructure of atomic steps. The last part concerns the coupling between surface state electrons and surface phonon modes on the (0001)-face of beryllium. For the sake of convenience, some of the more detailed calculations will be presented in the appendices. Parts of this work are published in the references [26–29].

Chapter 2

Photoemission and Spectral Functions

The goal of this chapter is to introduce the notion of many-body effects and to define the spectral function, which is measured directly as function of energy and momentum in an angle-resolved photoemission experiment. We will see that, in the case of a Fermi liquid, the structure of the spectral function becomes quite simple, and the one-particle picture preserves its meaning.

2.1 Angle-Resolved Photoemission

Since its discovery by Hertz at the end of the 19th century and its explanation by Einstein in 1905, the photoelectric effect became a very powerful tool in the study of electronic structure. In this chapter, I will restrict the outline to angle-resolved photoemission (PE) in the vuv-regime (angle-resolved ultra-violet photoelectron spectroscopy, ARUPS), and to the relation between the photoemission spectra and the spectral function introduced in the following sections. More details and descriptions of related techniques can be found in numerous review articles and books, e.g. Refs. [30–33].

The photoemission experiment is sketched in Fig. 2.1. Photons incident onto the sample surface are absorbed by electrons. The latter are excited into final states under strict momentum conservation (the momentum of vuv-photons can be neglected). If their energy in the final state is higher than the vacuum level, given by the Fermi energy plus work function, they can leave the sample. Amongst the parameters, which can be chosen in the experiment, are the polarization vector, energy, and angle of incidence of the light, the sample orientation and temperature. Electrons are then collected according to their kinetic energy in vacuum, the emission angle, and eventually their spin.

For the sake of simplicity, the so-called one-step model of photoemission [30] will be used in the following of this outline. Within this model, the electron final state is approximated by a time-reversed LEED-state (LEED = low-energy-electron diffraction), i.e. an electron

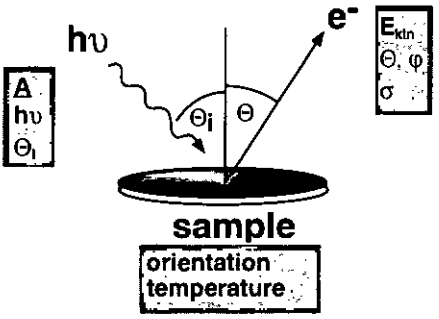

Figure 2.1: *Sketch of a photoemission experiment. Light of frequency ν and polarization vector* **A** *is incident onto the sample under an angle Θ_i with respect to the surface normal. The sample is held at temperature T. Electrons are detected according to their kinetic energy E_{kin} and their emission angle relative to the crystal axes of the sample.*

impinging onto the surface with wavevector $-\mathbf{p}$. The electron wave is refracted at the solid-vacuum interface due to the broken translational symmetry. The wavevector component perpendicular to the surface is altered, whereas the component parallel to the surface $\mathbf{k}_\parallel$ is conserved modulo a reciprocal lattice vector of the surface $\mathbf{G}_\parallel$: $\mathbf{k}_\parallel + \mathbf{G}_\parallel = \hbar^{-1}\mathbf{p}_\parallel$. If $G_\parallel \neq 0$, one speaks of a surface *umklapp* process [32]. A discussion of different methods to determine the absolute momentum can be found in the review articles cited at the beginning of this chapter. Inside the solid, the LEED-electron can be "absorbed" in a high-lying empty state, or be reflected due to a gap in the band structure. In the latter case, the LEED-wave has only a strong contribution at the surface and decays very fast inside the solid ("gap emission" [30]). The photoemission (PE) process can finally be described as a momentum-conserving optical transition of an electron from its initial state into the time-reversed LEED-state. Since the escape depth of the electrons is additionally limited by inelastic processes, PE is only sensitive to the near-surface region of the sample (typical values of the inelastic mean-free path range from 5 to 10 Å for photon energies of the order of 20-40 eV [32,33]). With known kinetic energy E_{kin} of the electron outside the sample (work function ϕ), emission angle Θ, and photon energy $h\nu$, we can calculate the wavevector $\mathbf{k}_\parallel$ and the "binding energy" of the electron in the initial state E_i:

$$E_i = E_{kin} - h\nu - \phi \tag{2.1.1}$$

$$k_\parallel = \sqrt{\tfrac{2m}{\hbar^2} E_{kin}}\,\sin\Theta. \tag{2.1.2}$$

For the following discussion, it is more convenient to identify E_i with the energy of the photohole state. The interaction between the electromagnetic wave field $\mathbf{A}(\mathbf{r},t)$ and the

electron wave function ψ can be written down to be [33,34]:

$$H_{int}\psi = \frac{e}{2mc}\left[2\mathbf{A}\cdot\mathbf{p} + i\hbar\, div\mathbf{A} + \mathcal{O}(|\,\mathbf{A}\,|^2)\right]\psi, \tag{2.1.3}$$

where $\mathbf{p} = i\hbar\nabla$ is the electron momentum operator. The term quadratic in $|\,\mathbf{A}\,|$ is usually neglected. In the following, we choose the Coulomb gauge of the electro-magnetic field $div\mathbf{A} \propto \nabla\cdot\mathbf{A} = 0$, although this term was shown in recent experiments to influence the line shape of bulk transitions in PE spectra [35,36]. The interaction hamiltonian reduces then to $H_{int} \propto \mathbf{A}\cdot\nabla$. The transition rate from the initial state $|i\rangle$ to the finale state $|f\rangle$ is given in the dipole approximation[a] by Fermi's Golden Rule [32–34]:

$$w_{fi} \propto |\langle f|\, H_{int}\,|i\rangle|^2\, \delta(E_f - E_i - h\nu). \tag{2.1.4}$$

In the *sudden approximation*, the excitation process $|i\rangle \rightarrow |f\rangle$ can be decomposed into two parts: First, an electron of wavevector $\mathbf{k}$ is removed and instantaneously decoupled from the ground state of the N-electron system. Then, the electron undergoes an optical transition into its final state, in which it is detected. It leaves behind a $(N-1)$-electron system in one of the possible excited states s. We write:

$$\begin{aligned} |f_s\rangle &= a^\dagger_{\mathbf{k_f}}\,|N-1,s\rangle \\ |i\rangle &= \quad |N\rangle\,. \end{aligned}$$

$a^\dagger_{\mathbf{k_f}}$ denotes the creation of a photoelectron of wavevector $\mathbf{k_f}$. Relation 2.1.4 then becomes [32,34]

$$\begin{aligned} w_{fi} \propto \quad & \sum_{\mathbf{G},\mathbf{k}} |\langle \mathbf{k}_f|\, H_{int}\,|\mathbf{k}\rangle|^2\, \delta(\mathbf{k_f} - \mathbf{k} - \mathbf{G}) \times \\ & \times \sum_s |\langle N-1, s|\, a_{\mathbf{k}}\,|N\rangle|^2\, \delta\left[E(\mathbf{k_f}) + E_s(N-1) - E(N) - h\nu\right]. \end{aligned} \tag{2.1.5}$$

Note that the momentum in the optical transition is conserved modulo a reciprocal lattice vector of the crystal. The sum on the right-hand-side of Eq. (2.1.5) is the projection of the hole state onto all possible final states. It can be identified with the spectral function A, which will be introduced below in section 2.3 (see Appendix A for more detail). Finally, abbreviating $M_{\mathbf{k}_f,\mathbf{k}} \equiv \langle \mathbf{k}_f|\, H_{int}\,|\mathbf{k}\rangle$, we obtain for the photoelectron current at energy E_{kin} and momentum $\mathbf{k}_f$:

$$\begin{aligned} I(E_{kin}, \mathbf{k_f}) \propto \quad & \sum_{\mathbf{G},\mathbf{k}} \int d\omega\; |M_{\mathbf{k}_f,\mathbf{k}}|^2\, A(\mathbf{k},\omega) f(\omega) \times \\ & \times \delta\left[\omega - (E_{kin} + \phi - h\nu)\right]\, \delta(\mathbf{k_f} - \mathbf{k} - \mathbf{G}), \end{aligned} \tag{2.1.6}$$

[a] Here, we assume that the wavelength of the light is large compared to the excitation volume [32].

where $f(\omega)$ denotes the Fermi-Dirac distribution. Up to this point we "abused" of an important simplification: the influence of the electron final state. The lifetime broadening of this state can be considerably larger than the extent in energy of the spectral function of the photohole. One expects therefore that fine structure be smeared out. In order to get an estimate of the additional broadening, we set the width of the spectral function equal to Γ_i. It was shown that the final state width Γ_f contributes to the observed width by [37–39]

$$\Gamma_{\text{obs}} \simeq \frac{v_i^{\perp}}{v_f^{\perp}} \Gamma_f + \Gamma_i \,,$$

where the factors $v^{\perp}$ denote the group velocities of the corresponding band states *perpendicular* to the surface. Since we are mostly concerned with surface states, $v_i^{\perp} = 0$ [39]. Hence, aside effects of the optical matrix elements and of the density of final states, spectra obtained from surface states directly reflect the spectral function of the photohole, broadened solely due to the dispersion of the initial state parallel to the surface (the corresponding factor has been dropped in the formula given above for the sake of clarity).

To conclude this section, I will briefly enter into particulars of the selection rules, inherent in the optical matrix elements. Consider a photoemission experiment in which photoelectrons are detected, which are emitted within a mirror plane of the crystalline sample. The symmetry of the photoelectron outside the sample implies that the final state in the photoemission process must be even under reflection at the mirror plane. If the light is polarized perpendicular to the mirror plane (s-polarization), then only transitions from initial states with odd symmetry with respect to the mirror plane into even final states are possible. In the case of p-polarized light, i.e. with the light polarization vector lying within the mirror plane, the matrix element is only finite if the initial state wave function is even. Thus, by means of the light polarization, the symmetry of the electron wave function can be probed in the PE experiment. More details can be found in Refs. [31, 40, 41].

2.2 Landau's Concept of Interacting Fermions

The spectral function exhibits generally more or less pronounced structure. The calculation and analysis of such spectra is often far from being obvious, and the attribution of structures to distinct excitations is very difficult. For this purpose, the concept of quasi-particles (Fermi-liquid theory), developed by Landau [2], is very useful. It resides on three assumptions [5]:

1. The one-to-one correspondence: each excitation of the non-interacting system corresponds to one excitation of the interacting system. The latter are named quasi-particles (QP). They can be seen as bare particles *dressed* with a cloud of excitations.

2. The momentum distribution: the state of an interacting system is completely characterized by the QP distribution function in momentum $\zeta(\mathbf{k})$[b]. In particular, the total energy is then given as function of $\zeta(\mathbf{k})$. The QP distribution may not be confused with the spectral weight distribution $n(\mathbf{k})$, which will be defined later [Eq. (2.2.12)]. Both are, however, identical in a non-interacting system. We are interested in the change in total energy, when we change the distribution function by $\delta\zeta(\mathbf{k})$ (as in a photoemission experiment) [3]:

$$\delta E = \sum_{\mathbf{k}} \epsilon[\zeta(\mathbf{k})]\delta\zeta(\mathbf{k}) + \frac{1}{2}\sum_{\mathbf{k},\mathbf{k}'} f(\mathbf{k},\mathbf{k}')\delta\zeta(\mathbf{k}')\delta\zeta(\mathbf{k}).$$

$\epsilon[\zeta(\mathbf{k})]$ and $f(\mathbf{k},\mathbf{k}')$ are the first and second functional derivative of the total energy with respect to the distribution $\zeta(\mathbf{k})$, calculated at equilibrium [3]. For our purpose, it is sufficient to consider only the first term and to define the QP energy as [5]

$$E_{\mathbf{k}} = \epsilon[\zeta(\mathbf{k})]. \tag{2.2.7}$$

3. A QP reacts to an external field with charge $-e$. The number of QPs is therefore conserved due to charge conservation.

Due to the presence of interactions, the excitation spectrum is, loosely spoken, a superposition of excitations of type

$$Z_m\, e^{i\omega_m t}\, e^{-\Gamma_m t}.$$

Z_m, ω_m, and Γ_m denote the weight, the energy and the inverse lifetime of excitation m, respectively. The excitation energy ω_m has to be calculated from Eq. (2.2.7). The many-body correction to the excitation energy and the inverse lifetime Γ_m respectively correspond to the real and the imaginary part of the self-energy $\Sigma(\mathbf{k},\omega)$. Close to E_F, the line shape of the QP excitation (often called the "coherent" part of the spectrum) can be represented as [9]:

$$A^{\mathrm{coh}}(\mathbf{k},\omega) = \frac{Z_k}{\pi}\frac{\Gamma_{\mathbf{k}}}{[\omega - E_{\mathbf{k}}]^2 + \Gamma_{\mathbf{k}}^2}. \tag{2.2.8}$$

By comparison of Eq. (2.2.8) and the relation between the spectral function $A(\mathbf{k},\omega)$ and the self-energy Eq. (2.3.19), given in section 2.3, the self-energy receives a physical meaning:

$$E_{\mathbf{k}} = \epsilon(\mathbf{k}) + Re\Sigma(\mathbf{k},\omega)\,|_{\omega=E_{\mathbf{k}}} \quad \text{QP energy,} \tag{2.2.9}$$

$$\tau_{\mathbf{k}} = [2\Gamma_{\mathbf{k}}]^{-1} = [2Z_{\mathbf{k}} Im\Sigma(\mathbf{k},\omega)\,|_{\omega=E_{\mathbf{k}}}]^{-1} \quad \text{QP lifetime,} \tag{2.2.10}$$

$$Z_{\mathbf{k}} = \left[1 - \frac{\partial}{\partial\omega} Re\Sigma(\mathbf{k},\omega)\,|_{\omega=E_{\mathbf{k}}}\right]^{-1} \quad \text{QP weight.} \tag{2.2.11}$$

[b]The dependence on position $\mathbf{r}$ is neglected here for the sake of clarity.

Moreover, if we are sufficiently close to E_F for that $\Gamma_{\mathbf{k}} \ll E_{\mathbf{k}}$ holds, we can linearize the real part of the self-energy [42]:

$$Re\Sigma(\mathbf{k},\omega) = \omega \frac{\partial}{\partial \omega} Re\Sigma(\mathbf{k},\omega) \equiv \alpha\,\omega \;\rightarrow\; Z_{\mathbf{k}} \equiv [1+\alpha]^{-1}.$$

Thus, the properties of the interacting electron gas are obtained from those of the non-interacting gas by a simple renormalization of the band parameters by the factor $Z_{\mathbf{k}}$. The

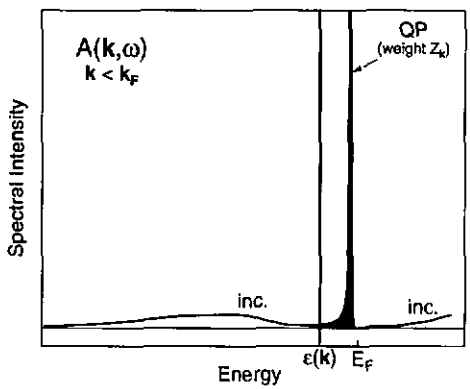

Figure 2.2: *Sketch of a typical electron removal spectrum of a Fermi liquid, $k < k_F$. The non-interacting case (δ-function) is indicated by a thick, vertical line. The shaded part represents the QP contribution. Note the incaherent part of the spectrum above the Fermi energy E_F.*

whole spectral function becomes then $A = A^{\mathrm{coh}} + A^{\mathrm{inc}}$. An analytic description of the "incoherent" part is beyond the scope of this work, and the interested reader is referred to Refs. [6, 18, 24, 43, 44]. The typical form of the excitation spectrum is displayed in Fig. 2.2. Since the QPs are fermions [3, 5, 43], the momentum distribution $n(\mathbf{k})$ of the QPs at finite temperature can be found by evaluating

$$n(\mathbf{k}) = \int_{-\infty}^{\infty} A(\mathbf{k},\omega)\, f(\omega)\, d\omega, \tag{2.2.12}$$

where $f(\omega)$ is the Fermi function. $Z_{\mathbf{k}}$ can be interpreted as measure of the bare-particle contribution to the spectral function [45]. As the QP peak crosses E_F for $k = k_F$, $n(\mathbf{k})$ exhibits a discontinuity of height $Z_{\mathbf{k}}$ at $T = 0$ due to the transfer of spectral weight into the unoccupied part (Fig. 2.3). This discontinuity defines the Fermi surface [3].

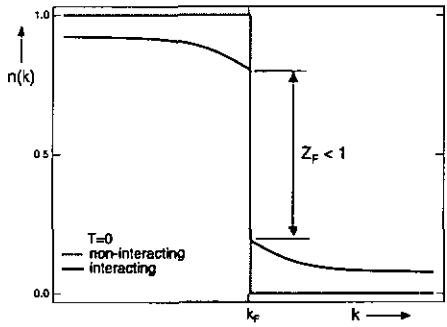

Figure 2.3: *Momentum distribution* $n(\mathbf{k})$ *at* $T = 0$ *of the spectral weight in the interacting (solid line) and the non-interacting (dotted line) system. Note that the QP momentum distribution* $\zeta(\mathbf{k})$ *is identical to that of the non-interacting electron gas [3, 45].*

2.3 Many-Body Effects

Prior to introducing the effects of many-body interactions in a formal way, the physics will be illustrated using as example the electron-phonon coupling. Consider an isotropic non-interacting electron gas at $T = 0$. For the sake of simplicity, the spin index will be dropped and the states are specified solely by the wavevector $\mathbf{k}$. In reciprocal space, all states $\mathbf{k}$ are filled up to the Fermi momentum $\mathbf{k}_F$. The total ground state energy E_0 of the electron gas is given by summing up the one-electron energies, in our example:

$$E_0 = \sum_{\mathbf{k}} \frac{\hbar^2 \mathbf{k}^2}{2m} \zeta_{\mathbf{k}} = \sum_{\mathbf{k}} \varepsilon(\mathbf{k}) \zeta_{\mathbf{k}}, \tag{2.3.13}$$

where m is the free electron mass and $\zeta_{\mathbf{k}}$ the occupation probability for momentum $\mathbf{k}$. We will introduce now the phonon modes and couple them to the electrons by some matrix element $V_{e\varphi}$. According to Luttinger's theorem [46], the Fermi surface remains the same upon switching on the interactions[c]. The high-energy cutoff of the phonon density of states (DOS) shall be given by the frequency ω_{max}.

We will proceed in two steps: first, the many-body correction to the one-particle energies will be derived, then the inverse lifetime will be evaluated. The interaction of electrons with phonons is given by the following hamiltonian, introduced by Fröhlich [8]:

$$H_{e\varphi} = \sum_{\mathbf{q},\mathbf{k}} V_{e\varphi}(\mathbf{q}, \mathbf{k}) a^{\dagger}_{\mathbf{k}+\mathbf{q}} a_{\mathbf{k}} \left(b^{\dagger}_{-\mathbf{q}} + b_{\mathbf{q}} \right) . \tag{2.3.14}$$

[c]More precisely, the *volume* enclosed by the Fermi surface is not altered by the interactions due to particle number conservation, but it may be deformed [46]. In the case of an isotropic system, as considered here, the Fermi surface is not changed at all.

The operators $a_{\mathbf{k}}^{\dagger}$ ($a_{\mathbf{k}}$) and $b_{\mathbf{q}}^{\dagger}$ ($b_{\mathbf{q}}$) create (annihilate) an electron of momentum $\mathbf{k}$ or a phonon of wavevector $\mathbf{q}$, respectively. The hamiltonian describes the scattering of an electron from state $\mathbf{k}$ into state $\mathbf{k}+\mathbf{q}$ by emission or absorption of a phonon $\mathbf{q}$. Multi-phonon and umklapp scattering will be neglected in the following. The coupling contributes to the ground state energy E by virtual processes: electrons are scattered by phonon emission from an occupied to an unoccupied state and back again by reabsorption of the phonon, as sketched in Fig. 2.4. At $T=0$, no phonons are present, and emission has to precede absorption. The intermediate state is traversed in such a short time that energy is not conserved in the virtual process owing to energy-time uncertainty [8]. Using second order perturbation theory and the interaction

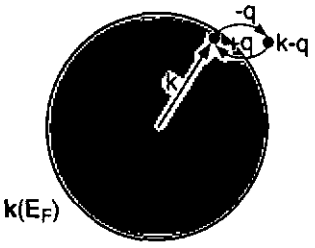

Figure 2.4: *Ground state of the interacting electron-phonon system at $T=0$. Electron states are filled up (shaded area) to E_F, given by the outer circle. Due to the coupling, electrons scatter out of the dark shaded region into unoccupied states and back again (virtual processes).*

hamiltonian as given above, the contribution of the virtual processes to the ground state energy can be computed to yield [5,8]:

$$E = E_0 + \frac{1}{N}\sum_{\mathbf{q},\mathbf{k}} \frac{\mid V_{e\varphi} \mid^2 \zeta_{\mathbf{k}}(1-\zeta_{\mathbf{k}-\mathbf{q}})}{\varepsilon(\mathbf{k}) - \varepsilon(\mathbf{k}-\mathbf{q}) - \tilde{\omega}(\mathbf{q})}, \tag{2.3.15}$$

where $\varepsilon(\mathbf{k})$ denotes the electronic band energy at wave vector $\mathbf{k}$ and $\tilde{\omega}(\mathbf{q})$ the phonon energy at wavevector $\mathbf{q}$. N is the number of electrons in the ground state.

Upon removal of an electron of momentum $\mathbf{k}$, the sum in Eq. (2.3.15) changes due to appearance of new virtual processes into the empty state $\mathbf{k}$ and due to the omission of processes out of state $\mathbf{k}$, as shown in Fig. 2.5. We are interested in the following problem: what is the amount of energy $E(\mathbf{k})$, necessary to remove the electron of momentum $\mathbf{k}$? In the spirit of Landau [2], the excitation energy is given as derivative of the total energy [Eq. (2.3.15)]

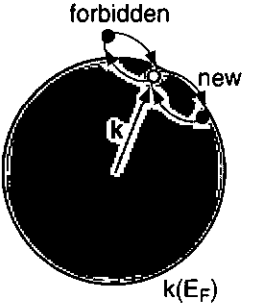

Figure 2.5: *Appearance and disappearance of virtual processes due to the removal of an electron at* $\mathbf{k}$.

with respect to the distribution function, thus

$$E(\mathbf{k}) = \varepsilon(\mathbf{k}) + \frac{1}{N}\sum_{\mathbf{q}} |\, V_{e\varphi}\,|^2 \left[\frac{(1-\zeta_{\mathbf{k}-\mathbf{q}})}{\varepsilon(\mathbf{k}) - \varepsilon(\mathbf{k}-\mathbf{q}) - \tilde{\omega}(\mathbf{q})} + \frac{\zeta_{\mathbf{k}-\mathbf{q}}}{\varepsilon(\mathbf{k}) - \varepsilon(\mathbf{k}-\mathbf{q}) + \tilde{\omega}(\mathbf{q})}\right]. \tag{2.3.16}$$

The sum on the right-hand-side of Eq. (2.3.16) constitutes the many-body correction to the one-particle energy. The first fraction describes the disappearance of virtual processes out of the state $\mathbf{k}$, the second the contribution of new processes into state $\mathbf{k}$. Both contributions cancel, if $\mathbf{k} = \mathbf{k}_F$. Far from the Fermi surface, only the contribution of new processes is important due to the singularities in the energy denominators and the cut-off by the distribution function. The situation is sketched in Fig. 2.6 for two different wavevectors. As can be seen from Eq. (2.3.16), states with energies higher than $\varepsilon(\mathbf{k}) \pm \omega_q$ yield a negative correction to the single-particle energy, whereas those of lower energies yield a positive correction. The negative and positive contributions are represented as black and dark grey areas in Fig. 2.6, respectively. Both contributions cancel approximately, if the electron energy is larger than the maximum phonon energy [part (a) in Fig. 2.6]. Upon approaching the Fermi surface, the negative contribution vanishes due to the cut-off by the distribution function and the correction becomes important. At the same time, unoccupied states start to contribute to the many-body correction, as mentioned above, and the correction becomes zero again at the Fermi surface. Thus, the largest correction is expected for electrons, whose energies differ from the Fermi energy by the maximum phonon energy. Summarizing, the electron-phonon coupling renormalizes the electron dispersion close to the Fermi surface and yields a vanishing correction far away from E_F.

The second effect of interactions on the excitation spectrum is the finite lifetime of the hole state $\mathbf{k}$. Electrons from occupied states with energies between $\varepsilon(\mathbf{k})$ and $\varepsilon(\mathbf{k}) + \omega_{max}$ can scatter into $\mathbf{k}$ under emission of a phonon. Owing to energy conservation in this scattering process, the lifetime depends on the number of available electron states with higher energy

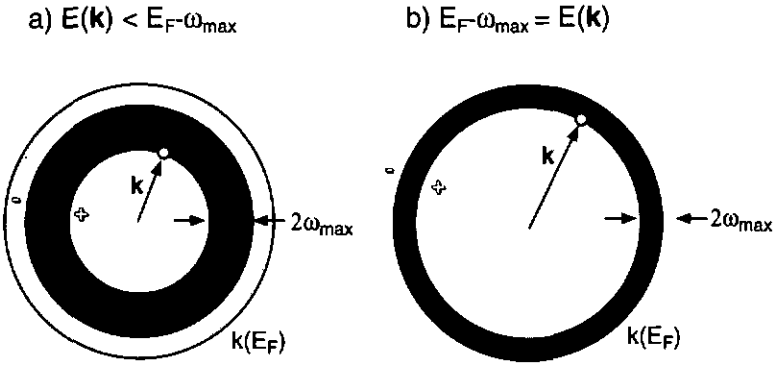

Figure 2.6: *Contribution of new virtual processes to the many-body correction of the single-particle energy after removal of an electron. Contributions, which increase (decrease) the single-particle energy are shown as dark grey and black areas, respectively. a) For energies far away from E_F on the scale of the maximum phonon energy ω_{max}, both contributions cancel nearly. b) Close to the Fermi surface, the negative (black) contribution is cut by the distribution function. The correction becomes very large and enhances the single-particle energy.*

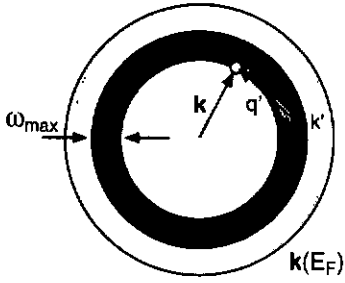

Figure 2.7: *Decay of a hole excitation. Due to the interaction with phonons, electrons from occupied states with energies between $\varepsilon(\mathbf{k})$ and $\varepsilon(\mathbf{k}) + \omega_{max}$ can scatter into the state $\mathbf{k}$ under emission of a phonon. These processes are energy-conserving and limit the lifetime of the hole excitation.*

and on the number of phonons. If $\varepsilon(\mathbf{k})$ is far from E_F on the scale of the phonon energies, phonons of any mode can be emitted, and the lifetime can be shown to be constant in energy. Close to E_F, less occupied states are available to fill the hole, and the lifetime increases and becomes infinite at the Fermi surface. The excitation spectrum at $\mathbf{k}_F$ is thus dominated by

a δ-Function at E_F. The notion of the Fermi surface persists therefore in these excitation spectra. This point is, of course, not trivial and strongly related to the question of validity of the quasi-particle concept. The spectra obtained in our example above at different momenta are shown schematically in Fig. 2.8. $\tilde{k}$ denotes the momentum at which the electron energy $\varepsilon(\mathbf{k}) - E_F$ equals the maximum phonon energy.

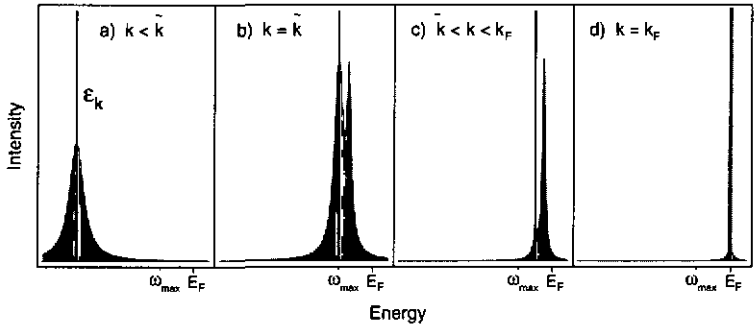

Figure 2.8: *Sketch of the excitation spectra (grey) as obtained in the example of an interacting electron-phonon system. $\tilde{k}$ corresponds the state, whose energy $\varepsilon(\mathbf{k}) - E_F$ equals the maximum phonon energy ω_{max}. Cases (a) through (d) refer to a) $k < \tilde{k}$, b) $k \approx \tilde{k}$, c) $\tilde{k} < k < k_F$, and d) $k = k_F$. The thick vertical lines represent the δ-functions at $\varepsilon(\mathbf{k})$ of the non-interacting electron gas.*

More formally, an expression can be derived for the excitation spectrum using the Green's function formalism [6, 47]. Let $a_\mathbf{k}$ denote the annihilation operator of an electron in state $\mathbf{k}$ (including the spin index), and $|E_N\rangle$ the ground state of the N-electron system. In the following I will restrain the calculation to the injection of a hole, i.e. to $k < k_F$. The process of removing one electron at time $t = 0$ can be written as

$$|\varphi_\mathbf{k}(t=0)\rangle \equiv a_\mathbf{k}(t=0)\,|E_N\rangle\,.$$

As we have seen in the example above, the new state $|\varphi_\mathbf{k}(0)\rangle$ is in general not a stationary state. In order to calculate the propagator of the hole, the advanced one-particle Green's function has to be calculated:

$$G^{\mathrm{adv}}(\mathbf{k},t) = i\,\langle E_N|\left[a_\mathbf{k}^\dagger(t), a_\mathbf{k}(0)\right]_+ |E_N\rangle\ ,\ t > 0.$$

After time-energy Fourier transform of the Green's function (see Appendix A), the equation of motion can usually be written as [43, 47][d]:

$$[\omega - \varepsilon(\mathbf{k})]\,G^{\mathrm{adv}}(\mathbf{k},\omega) = 1 + \Sigma(\mathbf{k},\omega)G^{\mathrm{adv}}(\mathbf{k},\omega), \tag{2.3.17}$$

[d]Eq. (2.3.17) can be written in a different form, known as the Dyson-equation [47].

which defines the complex-valued function $\Sigma(\mathbf{k},\omega)$ as the self-energy, which was introduced in the preceding section 2.2. The latter contains the whole many-body physics of the problem and can be found, e.g., by perturbation approach [47]. Finally, one finds [43]:

$$G^{\mathrm{adv}}(\mathbf{k},\omega) = \frac{1}{\omega - \varepsilon(\mathbf{k}) - \Sigma(\mathbf{k},\omega)}. \tag{2.3.18}$$

The spectral function $A(\mathbf{k},\omega)$ is related to the Green's function by

$$A(\mathbf{k},\omega) = \frac{1}{\pi} ImG^{\mathrm{adv}}(\mathbf{k},\omega - i\delta) = \frac{1}{\pi} \frac{\mid Im\Sigma(\mathbf{k},\omega) \mid}{\left[\omega - \varepsilon(\mathbf{k}) - Re\Sigma(\mathbf{k},\omega)\right]^2 + \left[Im\Sigma(\mathbf{k},\omega)\right]^2}, \tag{2.3.19}$$

where we added an infinitesimal imaginary part to the energy, as required by the analytic properties of the advanced Green's function for $\omega < 0$ [48]. As a consequence of the interactions, unoccupied states participate in the spectral function even at $T = 0$. Thus, for $k < k_F$ spectral weight is lost in the occupied part, and, *vice versa*, spectral weight is gained for $k > k_F$. The momentum distribution of the occupied spectral weight is, therefore, generally smaller than 1 [6,43].

Chapter 3

Experimental Setup

This part of the thesis covers the description of the whole experimental setup, necessary to prepare, characterize, and measure the samples studied in this work. Some points, like the transfer system and the sample heating stage, were already described in detail elsewhere [49]. Particular attention is paid to the assembly and calibration of the vuv-monochromator, the angle-resolved mode of the electron analyser, and the different experimental methods used to characterize the samples.

3.1 The Vacuum System

Photoemission measurements have to be done in vacuum for several reasons:

- the use of uv-light and x-rays requires vacuum because photons with energies higher than visible light are strongly absorbed in air. One then speaks of vacuum ultraviolet- (vuv-) radiation.
- electrons leaving the sample can travel typically some centimeters in gas of atmospheric pressure. A vacuum of 10^{-10} Torr ensures, in contrary, a mean free path of several hundreds of kilometers allowing the electrons to reach the detector without experiencing any collision.
- any contamination of the sample surface by residual gases has to be avoided since PES is extremely surface sensitive in the range of photon energies used in this work.

For this purpose, an ultra-high vacuum (UHV) system was built up consisting of three units: the measurement chamber, the sample preparation facility and a sample introduction/storage system (see Fig. 3.1). All vessels are evacuated by 2-stage turbomolecular pumps, the necessary forevacuum (about 1 Torr) being provided by oil-free membrane backing pumps. In addition, titanium sublimation and getter pumps are used to accelerate achievement of the

base pressure after bakeout and to limit the residual hydrogen pressure, respectively. The total pressure in the system is monitored by ionisation and cold-cathode gauges, and the composition of the residual gases is measured by a quadrupole mass spectrometer attached to the preparation facility. The whole apparatus is schematically drawn in Fig. 3.1.

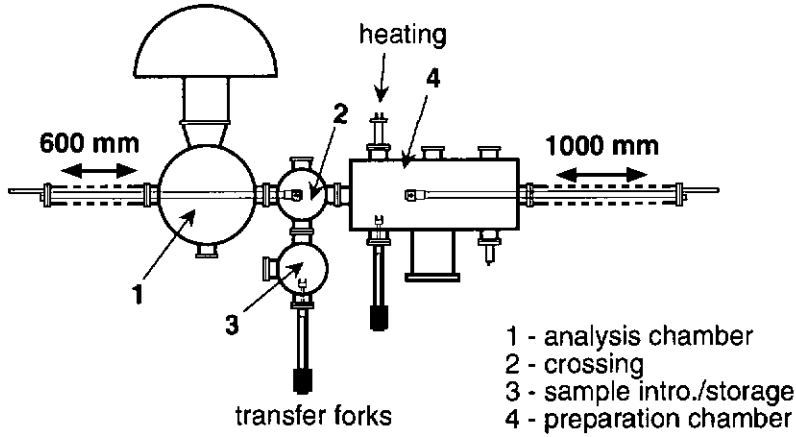

Figure 3.1: *Schematic plan view of the chamber layout. 1: measurement chamber 2: transfer/scraping chamber 3: sample bank/introduction chamber 4: preparation chamber. The transfer forks and the sample heating/sputter-stage stage are indicated. (Courtesy of M. Garnier)*

On the left- and right-hand-sides of the system, the two manipulators are shown, which are used for the sample transfers and the different measurements. They are fixed on 600 mm- and 1000 mm- linear drives for the measurement and the preparation chamber, respectively. On both manipulators, samples can be cooled down to 10-16 K by means of open-cycle liquid He-cryostats, and be heated up resistively to about 200°C. Sample transfers between the two main manipulators and onto the heating stage are effectuated by means of fork-like manipulators. The different chambers are linked by valves to a small crossing, which can be used optionally for the attachment of evaporators or for tools to scrape or cleave samples. Each vessel may independently be vented with nitrogen. After venting, pumping and the subsequent bakeout, a base pressure of about $1-5\times10^{-11}$ Torr is reached within a few days.

3.2 The Preparation Chamber

3.2.1 Sample Preparation: Generalities

As samples or substrates, commercially available single crystals were used. The *ex situ* preparation usually included mechanical polishing with diamond paste (grain size 0.25 μm), and, depending on the sample, an electro-chemical treatment in order to remove an amorphous surface layer. The samples were azimuthally oriented by means of van Laue-back reflection and mounted onto Mo sample holders. The materials for the sample holder and the necessary springs, screws and foils were chosen in order to ensure stability during the heating/cooling cycles (between 10 and 1200 K) and to avoid interdiffusion of these elements with the sample. For the samples presented in this work, the sample holders were made of Mo and all things in contact with the sample were out of Ta. A typical mounting is depicted in Fig. 3.2.

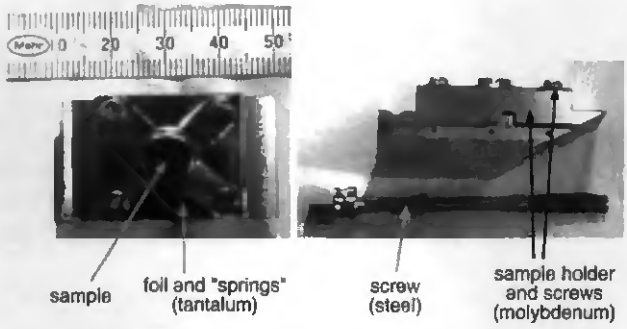

Figure 3.2: *Typical mounting of a single-crystalline sample onto a Mo sample holder. The scale in the upper left corner is given in millimeters. A Ta foil is inserted between the sample and the Mo holder in order to avoid diffusion of the Mo atoms during heating cycles. The springs (0.5 mm thick Ta foil) ensure that the sample is firmly fixed and that the mechanical tension onto the surface is negligible for the whole temperature range.*

The sample holder is screwed onto the manipulator head by means of a stainless steel screw. The large area of the holder in touch with the manipulator guarantees excellent thermal contact and, thus, the possibility to cool down to liquid He temperature.
The cleanliness and crystalline order of the surface are obtained by ion bombardment and heating. For this, the sample is transferred onto a separate stage and the steel screw removed. When on the sputtering/heating stage, the sample is electrically isolated. Usually, Ar^+ with kinetic energies varying between 600 V and 2 keV is used to sputter the sample surface. Ne^+-

sputtering turned out to necessitate subsequent annealing to much higher temperatures. The ion beam is scanned over the surface at video frequency and the drain current to ground measured allowing a continuous picture of the sputtered area to be seen on the monitor. Typical sample currents are of the order of 1 μA for Ar ions at 1 keV. The sample is annealed by means of electron bombardment with thermal electron emission from a filament and a sample bias of 1-2 keV. The heating power is controlled by a PID-circuit using the filament emission current as feedback parameter (see Ref. [49] for details). The parameters (ion kinetic energy, annealing temperature and duration) for the different surfaces studied will be given in the respective chapters.

3.2.2 Low-Energy Electron Diffraction (LEED)

The crystalline order is checked by low-energy electron diffraction (LEED). Since the electron energy in this type of experiment is of the order of 50-500 eV, the probed depth under the sample surface is small due to the small mean free path of the electrons (of order 10-20 Å). This method is, therefore, ideally well suited to study the order of the sample surface. Electrons incident onto the surface are scattered by interaction with the surface electron density. Constructive interference of the scattered waves is obtained when the wavevector change $\Delta\mathbf{k} = \mathbf{k}_0' - \mathbf{k}_0$ equals a vector of the reciprocal lattice $\mathbf{G}$ (Bragg- or van Laue-conditions, see e.g. [1, 50, 51]). The fulfillment of this condition can be visualised in the so-called Ewald-construction, shown in Fig. 3.3. For a given electron energy, all possible final wavevectors $\mathbf{k}_0'$ lie on a sphere of radius k_0, centered at $-\mathbf{k}_0$, the Ewald-sphere. The Bragg condition is fulfilled when a reciprocal lattice vector lies on the surface of this sphere. The outgoing electron wave is refracted at the surface under conservation of the momentum component parallel to the surface plane. It is observed on the spherical screen as light spot, whose distance from the (0,0)-spot (specular reflection) scales linearly with $\Delta\mathbf{k}_\parallel = \mathbf{G}_\parallel$. Seen by the observer as two-dimensional projection of the pattern from a sphere onto a plane, the pattern represents the reciprocal lattice (see Fig. 3.3), modulated by the structure factor of the lattice. The instrument used is a commercial Omicron-LEED with 4-grid optics, shown schematically in Fig. 3.3. Electrons are produced by a LaB_6-cathode and focused onto the sample as a beam with minimum divergence. The four spherical copper grids act as high-pass and filter the inelastically scattered electrons. Behind the grids the electrons are accelerated towards a spherical fluorescent screen and are observed as light spots through a viewport. A CCD-camera system can be mounted to record the images. This has the advantage that, a) long integration times can be used to enhance weak structures, and b) the spot profiles can be analysed numerically.

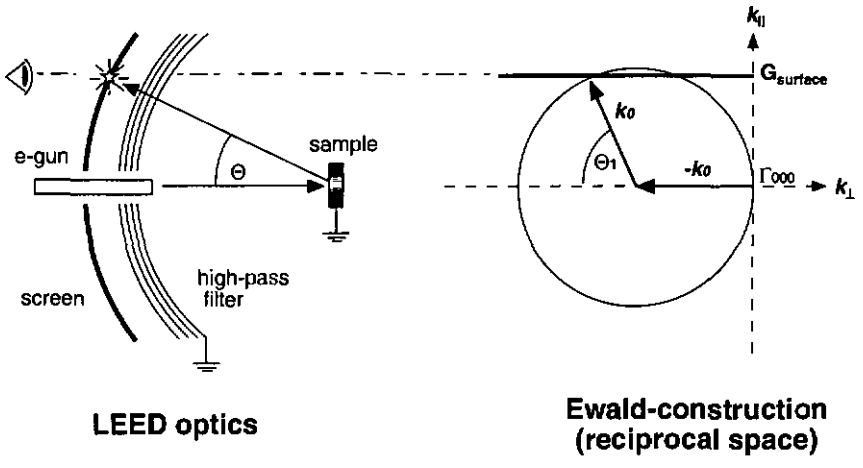

Figure 3.3: *Left panel: schematic drowing of the LEED-optics used. Electrons scatter from the sample surface and give rise to an interference pattern. This pattern is observed in reflection on a fluorescent screen. Right panel: Ewald-construction; constructive interference is obtained whenever a vector of the reciprocal lattice intersects the free-electron sphere. As an example, this is shown here for a reciprocal lattice vector of surface (independent of* $k_\perp$*).*

3.2.3 Auger Electron Spectroscopy (AES)

Electro-magnetic radiation or electrons with suitably high energy impinging onto a sample can eject electrons from the core shells of the atoms. The core holes left behind are refilled by higher energy electrons. The energy difference in this transition is transferred to another outer shell electron, which in turn can leave the sample. The latter are called Auger electrons and are analysed according to their kinetic energy, which is given solely by the transition energy and the binding energy of the Auger electron, thus independent of the excitation energy $\hbar\omega$. The recorded spectrum is typical for the kind of atom. The Auger process is shown schematically in Fig. 3.4. The mean free path of the Auger electrons leaving the sample, is comparable to that of LEED electrons. The method is therefore surface sensitive and is used to monitor the chemical composition of a surface [51]. In our case, the electron gun of the LEED and the 4-grid LEED optics are employed as excitation source and energy-selective electron detector, respectively. The former provides electrons with high primary energy (about 3 keV). The grids of the LEED optics retard the secondary electrons coming from the sample and act as a high pass filter. The electrons which pass the "analyser" are accelerated towards the screen and detected as current according to the actual retarding potential. Since the background and the signal/noise ratio are quite unfavorable for this kind

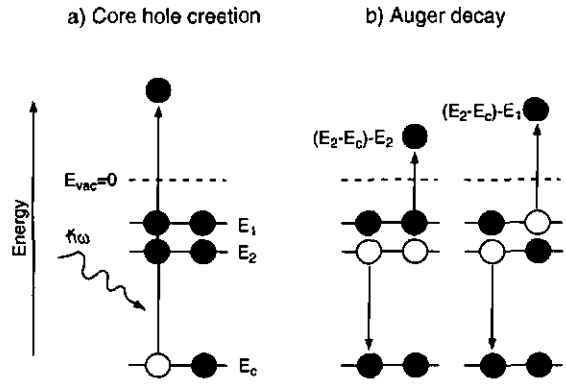

Figure 3.4: *Energy diagram of an Auger process. a) An electron from a core shell is emitted by energy-absorption from a high-energy electron or photon $\hbar\omega$. b) The core hole left is refilled by an electron with higher energy, the transition energy being transferred to a third electron. The latter can leave the sample and is detected according to its kinetic energy.*

of detection, the modulation technique is used. A small alternating voltage with frequency ω is added to the retarding potential. The current is detected by a lock-in amplifier at frequency ω or 2ω. The final signal is directly proportional to the Auger spectrum or its derivative. It can be compared with published data of almost all elements of the periodic table [52].

3.3 The Spectrometer

As a matter of principle, a photoemission experiment is simple, since it necessitates a monochromatic light source, providing photons with energies higher than the workfunction of the sample (typically 5 eV) and an energy-dispersive electron analyser. The requirement of high resolution, however, imposes stringent constraints:

- very narrow excitation lines,
- stable and accurate power supplies for the electrostatic analyser,
- efficient shielding of all perturbing electric and magnetic fields,
- efficient electron detection with high signal-to-noise ratio,
- precise mechanical alignment of the spectrometer as a whole, in order to avoid necessary corrections within the electron optics.

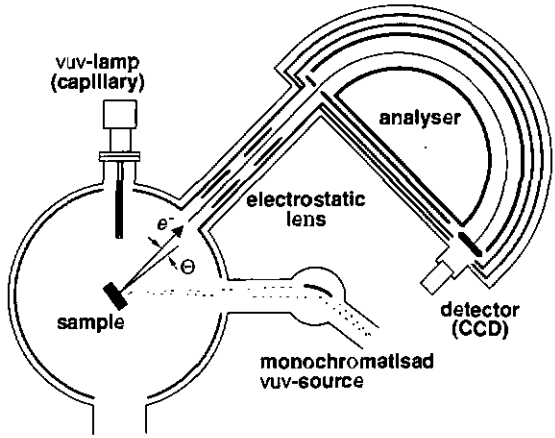

Figure 3.5: *View of the spectrometer. Three different light sources can be used, an unmonochromatised vuv-lamp, connected by a quartz capillary to the analysis chamber, a second vuv-source coupled to a monochromator, and a x-ray gun (hidden behind the capillary lamp in the figure). The emission angle Θ of the electrons analysed is varied by rotation of the sample. The spectrometer consists of an electrostatic lens system, followed by the hemispherical analyser and the fluorescing detector, observed by a CCD-camera.*

Moreover, a reasonable time scale of the experiment demands a strong signal intensity, i.e. a high-flux photon source and an analyser with high transmission. The system set up in our group, which fulfills these conditions, will be presented in this section. The spectrometer is shown schematically in Fig. 3.5. Three different light sources can be used, a x-ray gun (not shown in Fig. 3.5), and two vuv He discharge lamps. The light beams of both vuv-lamps form an angle of 45° with the analyser axis. Electron detection at different emission angles is performed by rotation of the sample. Note that the angle of light incidence and, consequently, the polarization of the light with respect to the surface plane, varies with changing emission angle.

3.3.1 The x-Ray Source

The x-ray source is a commercial Fisons x-ray gun, equipped with a twin anode (Al and Mg). The unmonochromatised *bremsstrahlung* spectrum is dominated by the strong Al-Kα- and Mg-Kα-excitation lines at 1487 and 1254 eV, respectively, which are used for photoemission. The experimental resolution is limited by the width of the excitation lines. It has been determined to be about 830 meV at 150 eV pass energy. x-ray photoemission spectroscopy (XPS, also called ESCA, electron spectroscopy for chemical analysis) is by

far the most direct way to monitor the chemical composition of a sample surface. It is therefore used as a complement to Auger spectroscopy. The different surface sensitivities of these two spectroscopies allow diffusion processes to be checked for. The advantages of XPS with respect to AES are the simple interpretation of the spectra and the stability of the experiment, since AES has to work in differential mode. The disadvantages are the time needed to record spectra, especially of elements with very small photoexcitation cross-sections, and the large spot of the x-ray gun. For small samples, contributions from the sample holder can render a conclusive interpretation of the XP-spectra difficult.

3.3.2 The vuv-Lamp

Usual laboratory sources for uv-light work with excitation lines, which are produced in a gas discharge. The gas atoms are excited or ionised by electron impact. The excited states de-excite by emission of uv-photons. The emitted radiation is denoted by Roman numerals I or II behind the atom symbol, for the excited neutral or the ionised atom, respectively, followed by a greek letter for the particular transition. In our case, we exclusively work with the transitions HeIα (21.2 eV), HeIβ (23.1 eV), HeIIα (40.8 eV), and HeIIβ (48.3 eV), commonly named HeI, HeI*, HeII, and HeII*, respectively. Since uv-light in this energy range is absorbed by most materials, the emitted photons are guided by a quartz capillary with small inner diameter (1.1 mm) into the analysis chamber or via the monochromator. The capillary has incisions at two places, which allow differential pumping of the discharge gas. The natural intrinsic lineshape of one of these emission lines is a lorentzian whose width reflects the inverse lifetime of the excited state (of order 10 μeV [53, 54]), broadened by the Doppler-effect to about 1-2 meV. It has been turned out that the high gas pressure, necessary in conventional lamps to maintain the discharge causes broad excitation lines decreasing the overall resolution of the spectrometer. This is due to the process of self-absorption, in which photons are absorbed by surrounding, unexcited gas atoms. Depending on the pressure, this broadening can reach more than 10 meV [53, 54].
Recently, two types of lamp have been commercialized, both of which allow a large reduction of the gas pressure. Through this, a decrease in the contribution of the self-absorption is achieved. At the same, one obtains a markedly increased intensity and a stronger contribution of emission at higher energies, in particular of HeII-photons [55–58]. The principle common to both lamps is the spatial confinement of the discharge plasma by an inhomogeneous magnetic field. In the lamp used in this work, an microwave field is coupled into the Ta-cavity where the discharge takes place. After initial ignition of the discharge by a high-voltage pulse, the electrons are forced onto cyclotron trajectories, accelerated by the electro-magnetic field (ECR, electron cyclotron resonance). The impact of high-energy electrons with gas atoms can ionise the latter and maintains the discharge. The ECR increases considerably the probability of collisions between atoms (ions) and electrons and allows the

Table 3.1: *Principal excitation lines of the Gammadata VUV-5000 source with their intensities relative to HeI-light and the calculated Doppler-broadening.*

Line	Energy [eV]	Intensity [%]	Doppler-width [meV]
HeI	21.218	100	0.9
HeI*	23.087	5.7 Ref. [57]	1.0
HeII	40.811 40.8118	5.4	1.8
HeII*	48.372	0.6 Ref. [57]	2.1

gas pressure to be decreased by at least one order of magnitude (the typical pressure is 10^{-3} Torr, measured at the exit of the cavity). The final excitation spectrum, obtained with He at full klystron power, is listed in Table 3.1. The relative intensities are calculated from gas phase spectra of Xe, recorded with a gas cell similar to the one described in Ref. [54].

3.3.3 The vuv-Monochromator

General Setup of the Monochromator

In order to avoid satellite-induced features in the photoemission spectra and to minimize the background above the Fermi level, the isolation of one excitation line is necessary. For this purpose, a vuv-monochromator was developed whose principal element is a toroidal diffraction grating. The exit hole of the lamp is at one focal point of the grating, and a slit aperture at the other. The latter serves as monochromatic light source for a toroidal mirror which images the aperture onto the sample in the analysis chamber. The monochromator is schematically drawn in Fig. 3.6. It is suspended by one axis in a frame allowing a rotation around this reference axis. The polarization vector of the light can thereby be changed from "parallel to the measurement plane" (p-polarization) to "perpendicular to the measurement plane" (s-polarization).

Four turbo pumps evacuate the different chambers. To reduce the gas flow, several cones were added which do not limit the light path. They are coated with colloidal graphite in order to minimize light reflection. The pressure is monitored by three cold cathode gauges, as indicated in Fig. 3.6. The gas load in the analysis chamber during the measurements is about 10^{-9} Torr (partial He pressure).

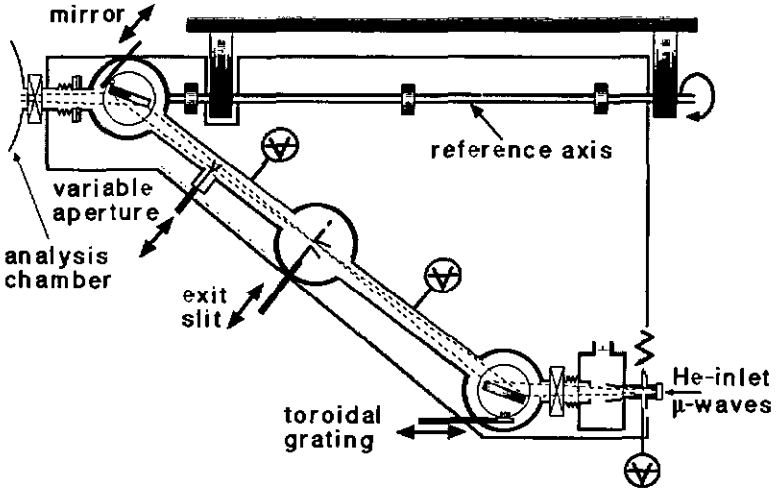

Figure 3.6: *Sketch of the vuv-monochromator. The microwave-driven lamp is located in the bottom right corner of the picture. Subsequent optical elements in the direction of light propagation are the grating, the exit slits, a variable aperture, and the mirror. The monochromator is mounted into a frame and turnable as a whole allowing the light polarization to be changed at the sample.*

Optical Properties

Geometry The monochromator uses a toroidal, Pt covered, holographic grating (Jobin Yvon Instruments SA, 1100 grooves per mm) in grazing incidence. The large radius of curvature $R = 1000$ mm in the dispersive direction is a compromise between a resolution, sufficient to separate the lines, and the intensity in the plane of the exit slit. The smaller radius $r = 104$ mm corresponds to the perpendicular, i.e. non-dispersive, direction. A detailed description of the optical properties and the aberrations of the grating can be found in Refs. [55,59]. The wavelength of the light diffracted into the exit slit is determined by the angle of light incidence onto the grating, and the total reflection angle of the grating, here fixed to be 142°. The photon energy can be tuned by rotation of the grating by means of a so-called sine drive, which translates a linear movement into an angular one, corresponding to the sine-function to a first approximation [55]. Behind the focal plane of the grating, the exit slit is imaged by a mirror with a 1:1 magnification onto the sample. The mirror (Scopas SARL) has like the grating two different radii of curvature ($r = 129.96$ mm, $R = 1226$ mm), the larger one belonging to the dispersive direction of the grating. The exit slit-mirror and mirror-sample distances are 400 mm. The total reflection angle is again 142°and the reflected

beam represents the reference axis of the monochromator. The mirror is made of Astrositall and covered with hardgold in order to ensure a high reflectivity of the vuv-photos.

Resolution One of the main problems of the monochromator is the separation of the first order HeI- and second order HeII- light. The difference in wavelength is only 23 Å (2× 303.8 Å - 584.4 Å). This corresponds to a difference in diffraction angle β of 0.345°, or 2.2 mm of lateral separation in the focal plane, in good agreement with the simulated dispersion stated by the manufacturer (about 10 Å per mm [59]). If the intrinsic line width is neglected, the resolution is limited by the width of source and exit slit. Ray tracing calculations reveal that the source size should be less than 2 mm of diameter and the exit slit less than 1.5 mm in the dispersive direction to separate HeI and HeII second order. In order to improve the resolution and to minimize the gas flow, a diameter of 1 mm (exit hole of the Ta-cavity) has been chosen. Two different exit slits are available, one elongated in the non-dispersive direction (2.5 × 1 mm^2), and a round hole (1 mm of diameter).

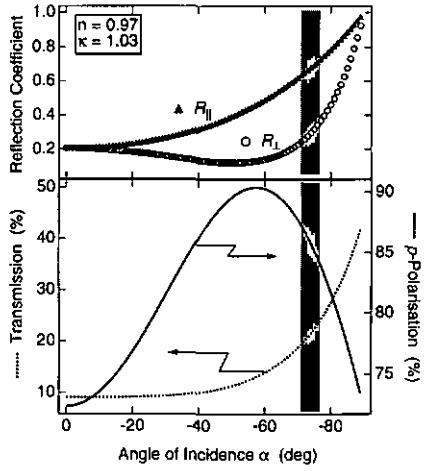

Figure 3.7: *Estimate of the polarization of the monochromatised light and the transmission of the monochromator. Upper ponel: reflection coefficients, calculated for Pt and 21 eV-radiation for light polarization perpendicular to the grating surface ($R_\perp$) and parallel to it ($R_\parallel$). Lower panel: transmission coefficient (dotted line) and polarization (solid line) including the mirror and the grating. A transmission of about 22% and a polarization of higher than 86% is calculated in the working region (shaded).*

Polarization The reflection coefficient of a metallic surface changes with the polarization vector of the impinging light. Depending on the angle of incidence, the reflected light will be partially linearly polarized in the direction along the grooves of the grating, i.e. perpendicular to the mounting plate of the monochromator. In Fig. 3.7 (upper panel), the reflection coefficients are displayed as a function of incidence angle. The values ($n = 0.97$ and $\kappa = 1.03$ for Pt and 21 eV-radiation) are taken from Ref. [55] and the formulae from Ref. [60]. The shaded area highlightens the range of incidence angle the grating is working in. In the lower panel of Fig. 3.7, the calculated "transmission" of the grating and the polarization are shown.

Intensity The photon flux from the Gammadata vuv-source is stated to be 1.2×10^{16} photons per second per steradian [57, 61]. One aim of the monochromator is to lose as less intensity as possible with respect to the lamp equipped with a capillary. An estimation of the emittance cone of a capillary has to be based on experimental work. Spot profile measurements taken with a similar capillary revealed a beam divergence of 0.4° [56]. In the case of the monochromator the relevant solid angle can easily be calculated by the area of the grating illuminated by the lamp. A solid angle of 1.5×10^{-4} sterad is obtained for the capillary and 3×10^{-3} sterad for the monochromator. About 25% of the impinging light are diffracted into zero order [60]. Supposing the same reflection efficiency for the mirror and the grating, one can obtain a rough estimate of the intensity in zero order (index "mo") with respect to the capillary lamp (index "cap"):

$$\frac{I_{mo}}{I_{cap}} \approx \frac{\Omega_{mo}}{\Omega_{cap}} \times T_{\text{grating}} \times T_{\text{mirror}} \times I_0 \approx 20 \times 22\% \times 22\% \times 25\% \approx 24\%,$$

i.e. at first glance, an intensity drop by a factor of 4.

Measured Characteristics of the Monochromator

The monochromator was experimentally calibrated using an Al-foil photocathode. The latter was biased with -25 V and the total current measured as a function of the grating position. The recorded diffraction spectrum is displayed in Fig. 3.8 and the obtained absolute intensity values listed in Table 3.2. Using photoemission, an intensity lower by a factor of 3 for the monochromator in zero order than for the capillary lamp, was found, thus slightly worse than the estimate in Table (3.2). Surprisingly, in photoemission spectra the HeII-light is found to be more intense in first order than in zero order, probably because of the optimization of the grating for 20 eV-photons.

The polarization of the light was measured using Cu(100), whose d-bands possess a well defined symmetry at the $\overline{\text{M}}$-point of the surface Brillouin zone. Two spectra recorded with different light polarizations are shown in Fig. 3.9. The degree of polarization of the light, defined as ratio of the intensity of the 100% polarized light to the total intensity, was found to

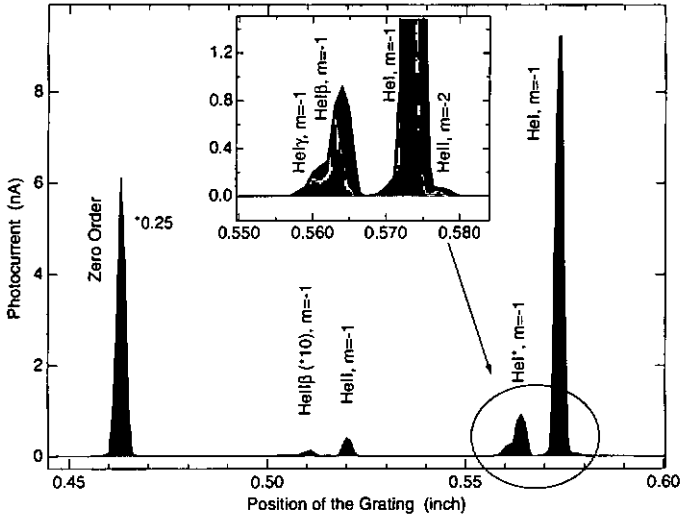

Figure 3.8: *Diffraction Spectrum of the monochromator, as measured from an Al-foil (bias voltage -25 V). Note that the zero order is scaled down by 4. Insert: Magnified view of the ronge around the HeI first order line. HeI* (m=-1) and HeII (m=-2) are clearly separated. The curve shaded in light grey was measured using the small exit hole.*

Table 3.2: *Excitation lines, angles of incidence at the grating α, and intensities obtained from the monochromator (big exit slit), compared to estimated intensity values from the capillary lamp (last column). The photoelectric cross-sections for Al were taken from Ref. [61].*

Line	Wavelength [Å]	Order	α [deg]	Sample Current [nA]	Intensity [10^{12} ph/sec]	Intensity (cap.) [10^{12} ph/sec]
all		0	-71	24.3	1.1	1.8
HeI	584.4	-1	-76.666	9.8	0.45	1.6
HeI*	537.06	-1	-76.206	0.97	0.045	0.09
HeII	303.8	-1	-73.942	0.44	0.036	0.097
		-2	-76.892	≈0.05	0.004	
HeII*	256.33	-1	-73.482	0.012	0.001	0.011

be greater than 86%, in excellent agreement with the estimation in Fig. 3.7. Measurements of a metallic Fermi edge confirm that the total spectrometer resolution is not affected by use of the monochromator. As last point, the shape of the light spot is shown (Fig. 3.10). It

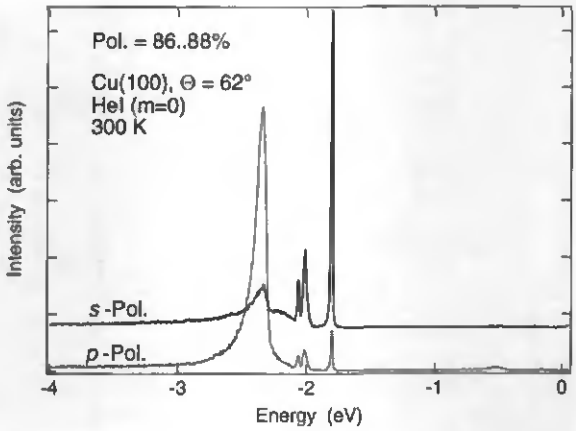

Figure 3.9: *Photoemission spectra taken from the Cu(100)-surface with different light polarizations. The vector potential of the photons probes the symmetry of the electronic states. This measurement can be used to measure the degree of polarization. About 86% p-polarization was found for the 0 order light.*

was gauged by means of a 0.5 mm Ag wire, moved vertically and horizontally through the spot (bias voltage -25 V). The spatial extent of the image is slightly larger than that of the exit slit.

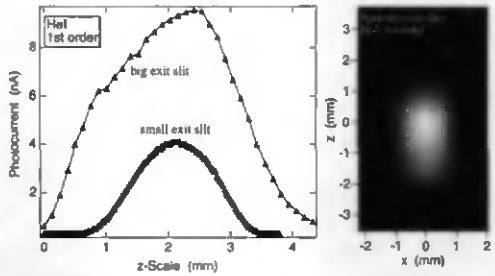

Figure 3.10: *Shape of the vuv-light spot for both exit slits (left panel). On the right-hand-side, the 2-dimensional shape of the spot is shown for the big exit slit.*

3.3.4 The Electron Analyser

The electron analyser Scienta SES-200 is an electrostatic analyser, optimized for high transmission and maximum energy resolution [62, 63]. It consists of three principal elements: an electron-optical lens, a hemispherical energy-dispersive analyser, and a two-dimensional detector (see Fig. 3.5).

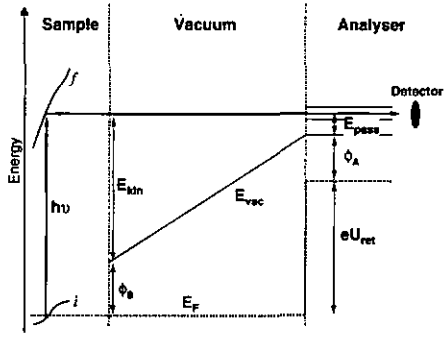

Figure 3.11: *Energy level diagram for a photoemission experiment. Electrons excited by photons of energy $h\upsilon$ leave the sample with the kinetic energy E_{kin}, referenced to the vacuum potential. They are detected if their energy corresponds to $E_{pass} + eU_{ret} + \phi_A - \phi_S$, where ϕ_A (ϕ_S) denotes the analyser (sample) work function.*

Electron Optics and Detection Electrons emitted from the sample into a cone of about $\pm 10°$ are collected by the electro-optical lens[a]. They are focused by the lens onto the entrance plane of the analyser. The analyser then produces an image of the variable entrance slit on the detector plane. At the same time it filters all electrons whose energies do not correspond to the user set pass energy. The sample is grounded, and all analyser voltages float on the retardation potential, allowing the kinetic energy of the detected electrons to be swept. This is schematically shown in Fig. 3.11. Once past the hemispherical analyser, the electrons pass a high-transmission gold mesh and are accelerated towards two multichannel-plates, mounted in a chevron configuration (MCP). The gold mesh minimizes the contribution of low-energy secondary electrons produced within the analyser [62, 63]. Passing by one of the channels of the MCP, the electrons cause an avalanche of electrons and therefore multiply their number by a factor of 10^7. These currents produce light spots on the fluorescent screen

[a]Three different entrance apertures are available. The given acceptance cone corresponds to the largest of these.

behind the MCP, where they are observed by a CCD-camera.
The peculiarity of this spectrometer is the 2-dimensional detector. One dimension of the detector corresponds always to the dispersive direction, i.e. the energy scale. The resolution is determined by the width of the entrance slits and the pass energy. It is controlled by measurements of the Fermi edge of metallic samples. Typical values obtained are better than 5 meV. The solid angle of the electron beam entering the analyser is given by the width of the entrance slits. It determines the angular resolution in the dispersive direction of the detector. Stated by the manufacturer to be below 1°, the value is estimated experimentally to be of the order of 0.2°. The second dimension of the detector can be chosen to represent either the spatial direction perpendicular to the measurement plane or the angle in this direction (i.e. the electron wavevector). These options are referred to as "transmission" and "angular" mode, respectively, and they can be compared to the different imaging modes of a transmission electron microscope. The observer (here: the hemispherical analyser) regards either the image (Gauss) plane of the electro-optical lens or its focal plane. The first one contains the spatial information whereas the latter gives the image in reciprocal space [64]. In this work, we are only concerned with the angle-resolved mode, visualised in Fig. 3.12: electrons leaving the sample under different emission angles perpendicular to the actual measurement plane, are collected at different positions on the detector. This relation angle-spot position depends on the voltages on the different deflection systems, defined in lens table files on the computer. Requirements are a fixed angular dispersion relation, independent of pass energy and retarding potential, and a high signal intensity. The lens tables have been calibrated for the whole energy range of UPS (i.e. 2 - 50 eV) by the experiment described in Fig. 3.12. With our calibration, 10% of the detector window correspond to about 1.8°. Hence, the width of the active detector window, defined by the user, determines the angular resolution perpendicular to the actual measurement plane.

Control of the Analyser The central control element is a PC. User chosen parameters are amongst others the pass energy, the lens mode, and the active detector window. The computer then calculates the different voltages and sends the commands via an IEEE-488-link to an interface box, which converts them into pulse-width modulated optical signals. The interface box is connected by optical fibers to the power supplies, which generate the desired voltages. This system has the advantage that the computer is completely decoupled electrically from the analyser, minimizing the risk of ground loops. A detailed description of the whole control unit can be found in Ref. [62]. The detecting CCD-camera is read out line by line via the video output (U.S. standard, frequency 30 Hz). This signal is decomposed and transferred into the different channels by a multi-channel logic device. The signal is summed up over the active detector window and sent back via the optical fibers to the computer. Simultaneously, the video signal of the CCD and the sum signal are displayed on a monitor. Sometimes it is useful to obtain an image of the whole detector for a fixed energy range. For

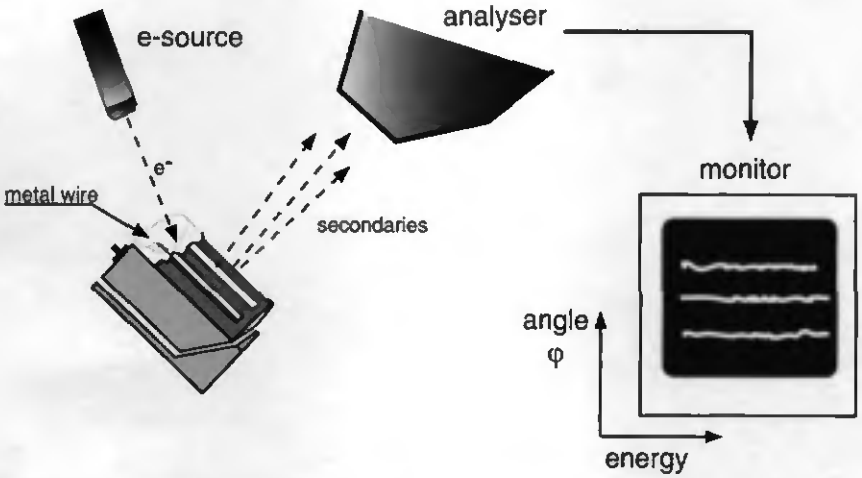

Figure 3.12: *Calibration of the angular mode of the electron optics. Secondary electrons are emitted from a metal wire by impact of high-energy electrons and leave the "sample" by one of the slits. Consequently, the image on the detector has to consist of parallel stripes for fixed angles and variable energies. The voltage tables of the electron optics are adjusted in order to reproduce a constant image independent of energy and with minimised optical aberrations.*

this purpose, a commercially available frame grabber card, controlled by a second computer, can be connected to the video output of the CCD. It allows the integration and summation of the video signal.

Chapter 4

The Surface Electronic Structure of the Group-V Semimetals

4.1 Motivation: One-Dimensional Metal in Mesoscopic Dimensions

The most spectacular breakdown of the Fermi liquid model may be expected to occur in one-dimensional (1D) metals. Such a material has a chain or wire structure leading to lateral confinement of the electrons. The salient point of the present discussion is the lateral dimension a wire must have in order to exhibit 1D properties. Elementary quantum mechanics implies that the electronic wave function changes upon confinement in dimensions, which are comparable to the wavelength. In solids, the relevant wavelength can be estimated from the inverse Fermi vector, yielding $\lambda_F = k_F^{-1}$. λ_F is called the Fermi wavelength and the condition of confinement reads: $\lambda_F \approx d$. For most metals, the length of the Fermi wave vector is of the order of the inter-atomic spacing, i.e. of the order of some Ångstrøm [1]. The effect of confinement, commonly called quantum size effect (QSE), is shown in Fig. 4.1 for an electron gas with parabolic dispersion. Let the wire have infinite length in direction x and lateral dimension d. The dispersion in x-direction is not changed, whereas the possible values of lateral momentum are discrete ("particle in a box"- model). The difference in energy of the quantum levels depends on the inverse effective mass and the width of the quantum box. The subbands are then filled with the number of electrons at disposal. The resulting density of states (DOS) is singular at the bottom of each band and decreases with increasing energy as $E^{-1/2}$. An ideal 1D system should only have the lowest band occupied, visualized by the grey shading in Fig. 4.1. The energy difference between the Fermi energy E_F and the bottom of the second band should be large on the scale of the temperature in order to avoid thermal population of the second band. This condition in line with typical electron densities of metals restricts to atomic chains. Such chains have meanwhile been

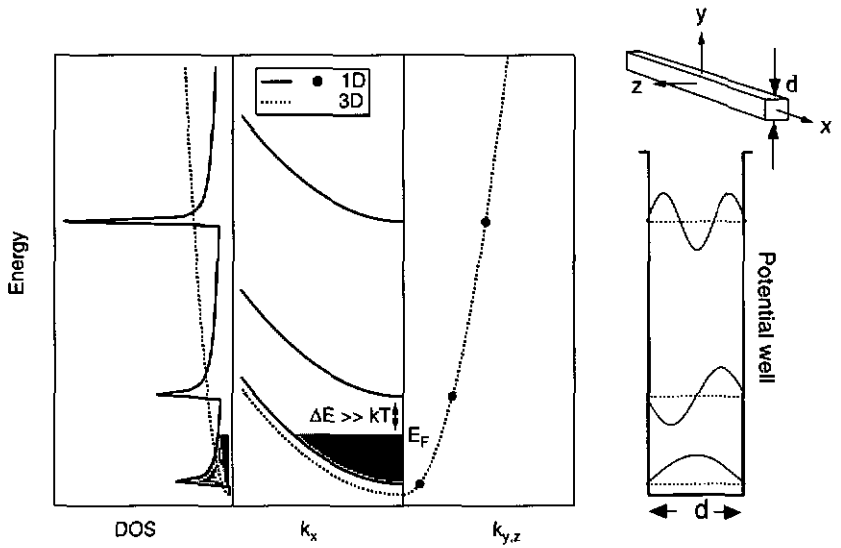

Figure 4.1: *Schematic representation of a 1D metal. The wire is supposed to run in x-direction. Its lateral dimension is d in the y- and z-directions (geometry in the upper right corner). Electrons are confined in y and z, and their wave function is given by the solutions of the "particle in a box"-model, sketched in the lower right panel. Resulting band structure (two centre panels for k_x and $k_{y,z}$) and DOS (left panel) are shown in the figure as thick lines and dots (denoting discrete k-values) and compared to the 3D case (dashed lines). Real 1D behaviour is expected if only the lowest energy band is occupied (grey shaded area) up to a Fermi energy E_F, which is far from the energy minimum of the next level on the scale of the temperature k_BT.*

successfully prepared [23, 65, 66]. However, the experimental problem encountered in the study of atomic chains is the band dispersion, which is not *a priori* known. This problem could be overcome if the wires were allowed to grow in the same way as the corresponding 3D bulk crystal, surrounded by some suitable insulating material. The required wire dimensions are of the order of several lattice spacings. Summarizing, in order to make use of QSE, as described above, for the study of a 1D metal, we are therefore limited to metals with very small electron densities.

4.2 Why Bismuth and Antimony?

Metals, or more precisely semimetals, with a electronic structure suitable for studies of mesoscopic systems, can be found in the group V of the Periodic Table of Elements. Bismuth

(no. 83) and antimony (no. 51) exhibit extremely small carrier densities of $3 \times 10^{17}\,\mathrm{cm}^{-3}$ and $3.4 \times 10^{19}\,\mathrm{cm}^{-3}$, respectively [67,68], thus orders of magnitude smaller than densities of common metals. The highly anisotropic Fermi wavelength can be as large as 140 Å for Bi and 50 Å for Sb. Size effects were already measured in numerous studies on length scales up to 1 micron [69–74]. Both elements can be grown as (111)-oriented crystallites on a wide variety of substrates [73–83] or in the pores of a ceramic compound [69,70].
The bulk band structure is well known from calculations [68,84–89] and experiments (see Ref. [90] for a review) and is expected not to be altered in structures on a nanometer scale [70,73]. At these length scales, however, the influence of the surface becomes very important, and drastic changes of the electronic structure at the surface were anticipated from results of some studies [75,91]. Several photoemission (PE) experiments on Bi have been published, but none of them examine those bands near E_F responsible for the transport properties. Surface states [92–94] and a large surface core level shift (SCLS) [95] have been found in the previous studies of Bi(111). The most intriguing result, however, is the appearance of a strong Fermi edge in normal emission spectra, contrasting with the expected low density of states of this material [95]. For Sb, no PE study has been published to the best of my knowledge. Aim of the present work was therefore to verify, whether the bulk carrier bands can be observed in PE spectra, and to look for differences between the bulk and the surface electronic structure.
It is anticipated that the observation of the carrier bands sets stringent constraints for the photoemission experiment. At 48 K [Bi(111)-surface [96]] and 211 K (bulk Sb [97]), the Debye temperatures of both elements are very low. Cooling to liquid He temperature is therefore indispensable if phonon-assisted indirect transitions are to be minimized [98]. The typical band width of the carrier bands is of the order of room temperature, i.e. 25 meV, and some effective band masses are of the order of 0.05 m_0. A reasonable signal intensity can only be achieved if the angular resolution is lowered. As a consequence, the corresponding resolution in k-space is not sufficient to resolve the dispersion in the directions of small effective mass.

4.3 Bulk Properties

4.3.1 Lattice and Brillouin Zone

Both elements crystallize in the rhombohedral A7-structure ($R\bar{3}m$, no. 166 of the *Int. Tables of Crystallography*). This structure can be given in either hexagonal or rhombohedral coordinates. In order to construct the rhombohedral lattice, we start from the simple cubic (sc)-crystal, represented by two interpenetrating fcc-lattices [1]. We obtain the rhombohedral lattice by effectuating two independent distortions: At first, the whole lattice is stretched

along the body diagonal [111] until the rhombohedral angle α reaches its equilibrium value (see Table 4.1). The second distortion is a relative displacement of the two fcc-sublattices along [111], defined by a value u. Commonly, the origin is set to be the midpoint between two nearest-neighbour sites on the [111]-axis. The two basis atoms are then found at the positions $(u,u,u)c$ and $(-u,-u,-u)c$, where c denotes the lattice constant in the [111]-direction. The lattice is, thereby, defined by two parameters α and u[a]. Put another way, the lattice is a sequence of pairs of planes, or bilayers, stacked along the [111]-axis. The distance between the two planes of one pair (intra-plane distance) is much smaller than the distance between two pairs (inter-plane distance), as can be seen from Table (4.1). This leads to a weak chemical bonding between the bilayers.

Table 4.1: *Lattice parameters of Bi and Sb at 4 K. The first set of values is taken from Ref. [68]; the others are calculated using the formulas given in Ref. [87]. Note the large difference between the inter- and intra-plane separation.*

parameter	symbol	Bi	Sb
unit cell volume	Ω_0	69.81 Å^3	59.9 Å^3
rhombohedral system			
length of lattice vector	a_0	4.7236 Å	4.4898 Å
n. n. distance	a_{nn}	3.0625 Å	2.9023 Å
rhombohedral angle	α	57.35°	57.23°
shear parameter	ϵ	0.0399	0.0417
internal displacement	u	0.23407	0.23362
min. atomic distance along C3	$2 \mid \tau \mid$	5.522 Å	5.243 Å
hexagonal system			
lattice vector [0001]	c	11.797 Å	11.222 Å
lattice vector [11$\bar{2}$0]	a	4.533 Å	4.301 Å
intra-plane distance	d_{intra}	1.59 Å	1.503 Å
inter-plane distance	d_{inter}	2.342 Å	2.238 Å

The A7-structure is displayed in Fig. 4.2. In the left panel, the rhombohedron of the primitive fcc-lattice vectors is emphasized. The right panel shows the hexagonal stacking of the (111)-layers containing each two planes. The repetition length of the stacking corresponds to 6 planes. The resulting lattice possesses a rather low symmetry. The principal symmetry elements are listed here:

[a] *A different set of parameters ϵ and τ is often used in literature: ϵ describes the shear of the lattice and is related to α, whereas the vector τ defines the displacement related to u [87].*

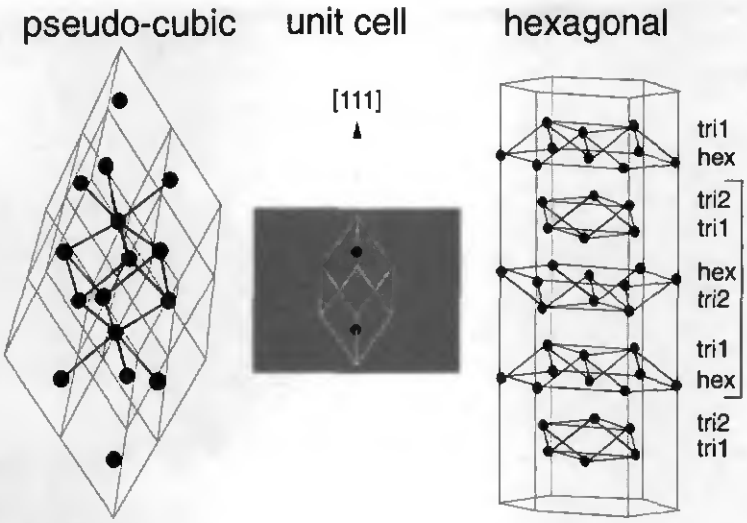

Figure 4.2: *The A7-structure. Left panel: pseudo-cubic structure; the rhombohedron in the centre corresponds to the fcc-like lattice vectors. In the middle: rhombohedral unit cell with the basis of two atoms. Right panel: hexagonal stacking of the lattice. The different types of planes are indicated (two trigonal and one hexagonal).*

- The *trigonal axis* [111], labeled C3.
- The $[1\bar{1}0]$-axis (and axes related through rotation by 60°around C3), perpendicular to C3, with two-fold rotation symmetry. This *binary axis* is labeled C1. It points from C3 toward an atom of a hexagonal layer.
- The $[2\bar{1}\bar{1}]$-axis (and axes related through rotation by 60°around C3), perpendicular to C1 and C3, labeled C2. It is called *bisectrix* and denotes the direction from the C3-axis toward an atom of one of the trigonal layers.
- The mirror planes spanned by C2 and C3 (usually named σ in literature).
- Centers of inversion are at the midpoints between neighbouring atoms along C3.

The Brillouin zone (BZ) of the A7-lattice is shown in Fig. 4.3 together with the surface BZ (SBZ) of the (111)-surface. The symmetry points are labeled according to the commonly used notation [86]. As expected from a fcc-like structure, the BZ corresponds to the Wigner-Seitz cell of the bcc-lattice. The points T and L, i.e. the centers of the hexagonal zone faces in [111] and [010]-direction, are no longer equivalent. The plane of interest is the mirror plane

σ or ΓTLUX (Fig. 4.3), whose projection of the (111)-surface corresponds to the $\overline{M'\Gamma M}$-line. The latter is emphasized in Fig. 4.3.

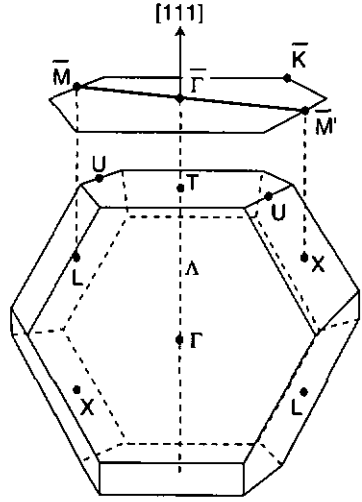

Figure 4.3: *Brillouin zone of the rhombohedral lattice. At the top, the SBZ is shown for the (111)-surface. The projection of the ΓTLUX-mirror plane of the bulk onto the (111)-face yields the $\overline{M'\Gamma M}$-line of the SBZ.*

4.3.2 Bulk Electronic Structure

The atomic electron configurations are [Kr]$4d^{10}5s^25p^3$ and [Xe]$4f^{14}5d^{10}6s^26p^3$ for Sb and Bi, respectively. The d-levels are far from E_F and can therefore be treated as core levels. The s-like valence bands are found at approximately 10-14 eV binding energy. The carrier bands at the Fermi level are mainly determined by the overlap of the 5th and the 6th valence bands, which dominantly are of p-character [99]. A schematic diagram of the valence band structure is given in Fig. 4.4.

Usually, the calculations of the band structure of the group-V semimetals [68, 84–89] are done within the pseudo-potential formalism [5, 100, 101]. Difficulties arise because of the very small energy scales involved and the large spin-orbit splitting in the case of Bi. Huge basis sets of plane waves are required to obtain a final accuracy of the calculations, which is of the order of the energy scales of the carrier bands [68]. A first insight can, however, be obtained with the so-called deformation theory of Abkrikosov and Fal'kovskiĭ [90, 102], which shows in a very figurative way the interplay between the lattice and the electronic

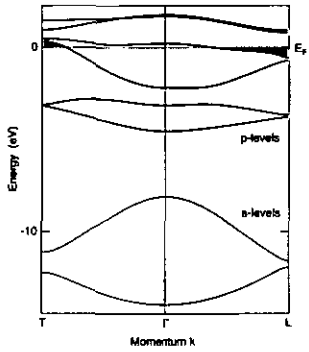

Figure 4.4: *Schematic representation of the bulk band structure of Bi and Sb. s-like bands are found at roughly 10-14 eV below the Fermi energy E_F, p-like states close to E_F. The 5th and the 6th valence band overlap at E_F, leading to small pockets of electrons and and holes (shaded).*

structure. As a result, the hexagonal zone faces in [111]-direction become inequivalent to the six others due to the lattice distortion along the trigonal axis. The centers of these faces (points T for the [111]-direction, L for the others) become the centers of the hole and electron Fermi surfaces. Recently, Liu and Allen presented a simple tight-binding scheme [103] for the semimetals Bi and Sb [104]. This model will be used for comparison with our experimental results. The Fermi surfaces of electrons and holes lie within the three mirror planes ΓTLUX, shown in Fig. 4.5. The electron pockets are ellipsoids elongated along the bisectrix and centered at the L-point [$\overline{\text{M}}$ of the (111)-surface] for both, Sb and Bi[b]. In the case of Bi, the hole pockets are ellipsoids elongated along the trigonal axis with circular cross sections perpendicular to the trigonal axis[c]. For Sb, the situation is somewhat more complicated, since the hole pockets are located in the mirror plane, but slightly off the [111]-axis (H-point), and have some "sausage"-like form [85, 88]. The projections of all bulk Fermi surfaces onto the (111)-surface are shown in Fig. 4.6.

As anticipated above, the carrier bands result from a small overlap of the 5th and the 6th at the Fermi level. Both bands are very close in energy at the centre of the electron Fermi surface, i.e. at the L-point, where they exhibit mirror-like dispersion. The very small energy gap between both bands causes severe deviations from the parabolic dispersion near L. Moreover, the strong temperature dependence of the energy gap [110] results in temperature dependent effective masses [67, 90, 105]. As a consequence, the electron Fermi energy, which depends on the overlap and the effective masses of electron and hole bands, has

[b]The surfaces are in fact non-ellipsoidal [105], but the deviations are far too small to be of interest here [106].

[c]A very figurative image of the Fermi surfaces of Bi can be found in Refs. [107, 108].

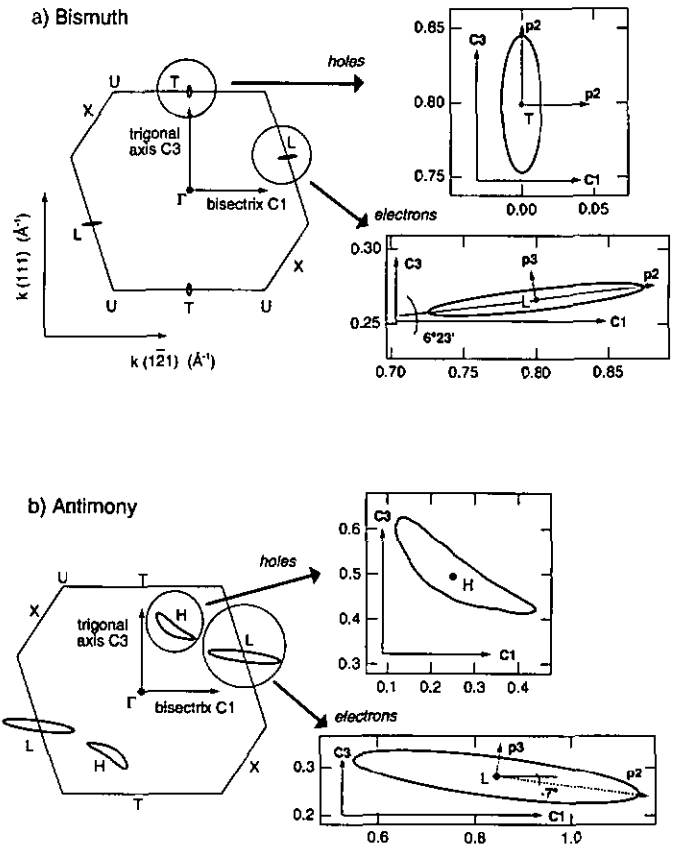

Figure 4.5: *Cut through the bulk BZ (ΓTULX-plane), and the Fermi surfaces of the electron and hole bands for Bi (a) and Sb (b). At the right-hand-side a magnified view of the Fermi surfaces; the coordinates are given in $Å^{-1}$ with respect to Γ.*

to be computed numerically in consideration of charge neutrality for a given temperature. It was shown to be constant in the range of 4-80 K, and to change dramatically for higher temperature [67]. A selection of band parameters at low-temperature is given in Table (4.2). The scattering of published data is quite large, since the data were mostly interpreted using different models [67,68,90,104,109,111]. Thus, we will use two experimental data sets for the Fermi surfaces [90,109] and calculate the remaining data using formulae given by Heremans and Hansen [67], assuming ellipsoidal form of the Fermi surfaces (ENP-model for "ellipsoidal non-parabolic).

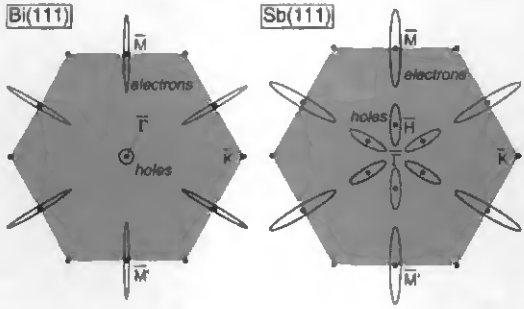

Figure 4.6: *Fermi surfaces of Bi on the left and Sb, projected onto the BZ of the (111)-surface (shaded). The dots correspond to the $\overline{M}$ and $\overline{K}$ symmetry points of the SBZ. The size of the Bi Fermi surface has been enhanced by a factor of 4 for the sake of clarity.*

Table 4.2: *Band parameters of Bi and Sb at 4 K. Energies and principal momenta were taken from literature [90, 109]. Directions 1, 2, and 3 refer to C1, C2, and C3, i.e. the binary axis, the bisectriz, and the trigonal axis, respectively. Note that the principal momentum k_2 of the electron Fermi surfaces is 6-7° off the bisectriz C2 [88]. The hole FS of Sb is inclined by about 35-50° with respect to C2.*

			Bi	Sb
electrons	Fermi energy [meV]	E_F	27.2	90-206
	energy gap [meV]	E_{Gap}	13.6	101
	effective masses at band bottom [m_0]	m_{11}	1.26×10^{-3}	0.011
		m_{22}	0.256	0.537
		m_{33}	2.23×10^{-3}	0.011
	principal momenta [Å^{-1}]	$k_F(1)$	5.2×10^{-3}	0.042
		$k_F(2)$	0.074	0.297
		$k_F(3)$	6.9×10^{-3}	0.042
holes	Fermi energy [meV]	E_F	11	84
	effective masses [m_0]	m_{11}	-0.064	
		m_{22}	-0.064	
		m_{33}	0.667	
	principal momenta [Å^{-1}]	$k_F(1)$	0.0138	(-)
		$k_F(2)$	0.0138	(0.12-0.19)
		$k_F(3)$	0.046	(0.082-0.13)

4.4 Preparation of the Single Crystals

The crystals were mechanically polished to mirror finish and prepared *in situ* by sputtering (Ar^+, 1 keV) and annealing cycles. (111)-oriented crystals of Bi and Sb are usually cleaved

in situ. Jezequel *et al.*showed that, despite some differences in intensity, the results obtained from the cleaved or sputter-annealed Bi(111)-surfaces are identical [93].

Due to the low melting point of Bi (271°C), annealing (160°C) was done on the resistively heated 1000mm-manipulator. This treatment results in a hexagonal LEED-pattern [112] with rather broad spots (see Fig. 4.7). In the initial stages of the preparation, the contamination of the Bi(111)-surface could only be verified by XPS, since the Auger spectrum of clean Bi shows transitions near the typical peaks of carbon and oxygen. Later, an Auger spectrum taken from a clean surface can be used as reference. The Sb-surface was annealed

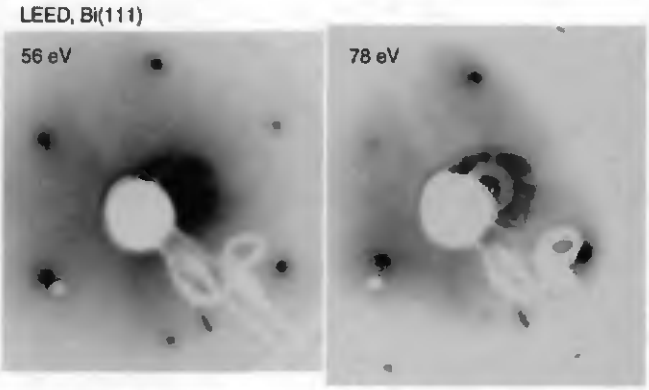

Figure 4.7: *LEED-images taken at electron energies of 56 eV and 78 eV from Bi(111). The trigonal symmetry of the [111]-axis is clearly observable.*

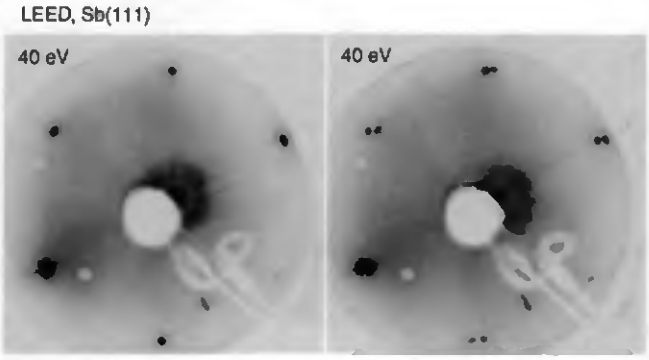

Figure 4.8: *LEED-images from Sb(111). The LEED-image on the right was taken with the beam incident on the border between two domains (see text).*

on the heating stage at 250°C, followed by a slow cooldown. Sb(111) tended to develop facets. Three large domains of same azimuthal orientation could be seen in the LEED-pattern (see Fig. 4.8). The polar orientation was identical for the three domains except close to the domain borders. This result could later be confirmed by photoemission. All spectra presented here are taken with the light spot placed in the centre of one domain. Note that no spectra could be taken with s-polarized light because the spot size extends over more than one domain in this geometry. The LEED-spots were generally much sharper than those of the Bi crystal. This is an inherent property of the crystals and was already observed in previous work [112]. The cleanliness of the Sb(111)-surface was checked by AES. Both elements turned out to be very inert against contamination by residual gases. Typically, once per week, sputtering of the surfaces was necessary in order to remove carbon.

4.5 Bi(111)

Previously, the electronic structure of Bi(111) has been examined by means of angle-resolved photoemission in normal emission geometry [92, 93] and along the two high-symmetry direction of the SBZ [94, 95]. The experimental results are in reasonable agreement with bulk band structure calculations [86, 104]. However, a strong surface state was shown to originate from a spin-orbit gap in the bulk band structure [92]. The latter can only be reproduced in calculations if substantial relaxations of the surface atoms are assumed [113]. Since the carrier bands at the Fermi energy are very sensitive to smallest distortion of the lattice, severe modifications of the carrier spectrum at the surface may be expected. For example, slight admixture of Sb to Bi changes dramatically the carrier band structure. At only 8 at.% of Sb, the overlap between hole and electron bands of the semimetal reaches zero [114]. As a result, the crystal becomes a semiconductor with direct band gap at the L-point.
Most of the spectra presented here are taken from the mirror plane of the lattice ΓTLUX, i.e. along the $\overline{M'\Gamma M}$ direction of the surface. The spectra have been taken with HeI-photons for reason of signal intensity and momentum resolution. For the sake of convenience, the cut through the bulk BZ corresponding to the mirror plane is depicted again in Fig. 4.9, and some parameters, which are necessary for the PE experiment, are given in Table (4.3).

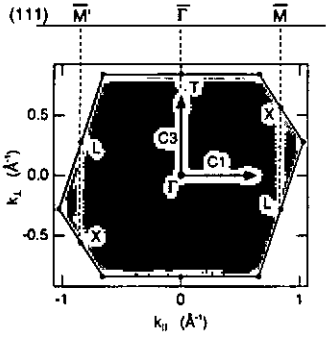

Figure 4.9: *ΓTLUX-mirror plane of the bulk (shaded) and its projection onto the (111)-surface. Note that the inversion symmetry of the bulk is broken at the surface, leading to two inequivalent directions* $\overline{\Gamma M'}$ *and* $\overline{\Gamma M}$.

4.5.1 Valence Band Structure

Figure 4.10 presents a series of angle-resolved spectra along $\overline{M'\Gamma M}$. The strong peak seen at about 250 meV in normal emission stems from a surface-induced state lying in the spin-

Table 4.3: *Some values for the (111)-surface used for the photoemission experiments.*

parameter	Bi(111)
work function (polycrystal, Ref. [115])	4.22 eV
Debye temperature (Ref. [96])	48 K
distance $\overline{\Gamma M}$ (centre of the electron FS)	0.797 $Å^{-1}$
centre of the hole FS	$\overline{\Gamma}$
distance $\overline{\Gamma K}$	0.92 $Å^{-1}$

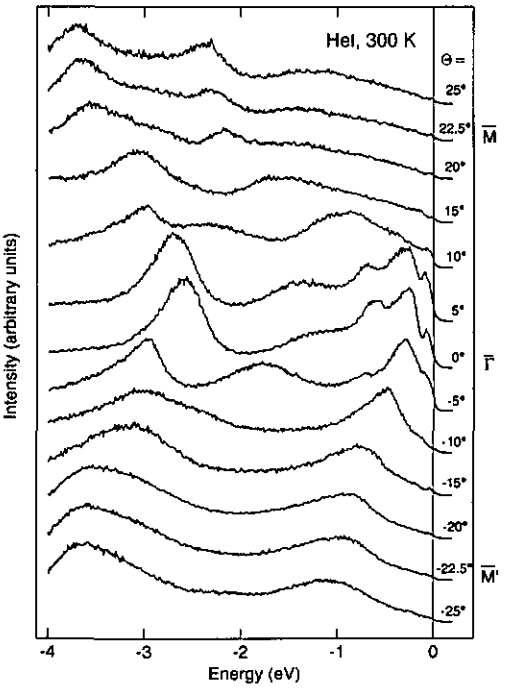

Figure 4.10: *Valence band spectra taken along the $\overline{M'\Gamma M}$-direction; the spectra are taken with unpolarized HeI-photons at 300 K, and are normalized to the total intensity.*

orbit gap at the T-point [94, 95]. The spectra are in excellent agreement with published data [92–95] and are partially even much better resolved. This indicates a good quality of the sputter-annealed sample.

Since it was one purpose of this work to observe the carrier bands of bulk Bi, a band

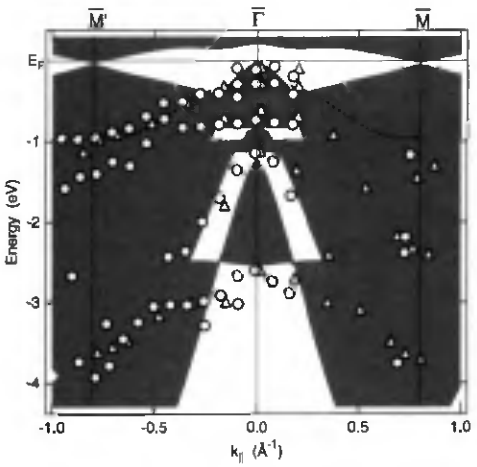

Figure 4.11: *Bulk band structure calculated within the tight-binding model [104] and projected onto the (111)-surface (shaded area). A thick dashed line displays the dispersion of the spin-orbit gap surface state (see text). Experimental peak maxima are plotted as large symbols vs $k_{\parallel}$ along $\overline{M'\Gamma M}$ for 300 K (triangles) and 10 K (p-polarized light, circles).*

mapping is unavoidable. The results are shown in Fig. 4.11. Data points, obtained from Fig. 4.10 and from spectra taken at low temperature (not shown here) are plotted vs $k_{\parallel}$ and compared to the bulk band structure, projected onto the (111)-surface. The band structure has been calculated using a tight-binding scheme [104]. The experimental data points have been determined using either lorentzian lineshapes or minima in the second derivatives of the energy distribution curves (EDC). The dispersion of the surface state in the spin-orbit gap, denoted by a dashed line in Fig. 4.11, was already analyzed for the direction $\overline{\Gamma K}$ [92, 95]. Tanaka and co-workers have taken spectra in the direction $\overline{\Gamma M}$, but they attributed erroneously peaks at higher binding energy to the surface state at the SBZ boundary [94]. Hence, their estimate of the band width (2.1 eV) exceeds by far the band width of about 750 meV found in the present work. The latter is in good agreement with results reported previously [92]. In connection with the analysis for $\overline{\Gamma K}$ [92, 95], we can conclude that the dispersion of this state is practically isotropic within the SBZ.

As anticipated above, the bulk Fermi surface of Bi consists of electron pockets centered at the six L-points of the bulk BZ and hole pockets at the T-points (see Fig. 4.6). Projected onto the (111)-surface under investigation here, one expects therefore to observe a band with very small negative effective mass crossing the Fermi level twice symmetrically around normal emission and a free-electron like band along the $\overline{\Gamma M}$-direction of the surface BZ centered at $\overline{M}$, i.e. the hole and the electron bands, respectively. Spectra, taken with p-polarized

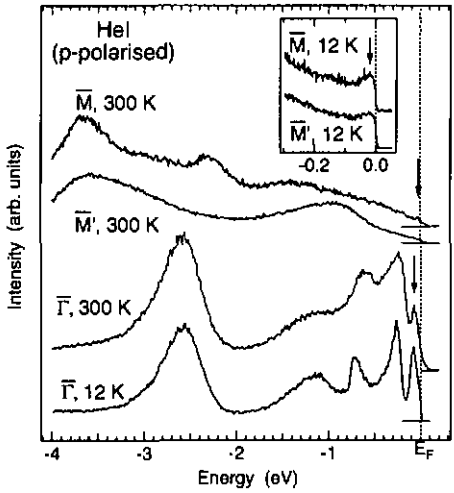

Figure 4.12: *Valence band spectra, taken with p-polarized HeI photons at various symmetry points. Arrows indicate the features of interest. The inset shows a zoom onto the Fermi level at the border of the SBZ, where the electron bands are observed.*

HeI-photons at these symmetry points, are displayed in Fig. 4.12. The inequivalence of the two directions $\overline{\Gamma M}$ and $\overline{\Gamma M}'$ is unambiguously reflected in the spectra. We want to focus our attention on the features highlighted by arrows in Fig. 4.12 and refer to the strong peak seen in normal emission as the hole band, to the weak structure at $\overline{M}$ as the electron band. As can be seen in the inset, this latter peak is observed in both directions. Because of the small signal intensity in the spectra taken around $\overline{M}'$, we restrict the analysis to the $\overline{M}$-point.

4.5.2 Electrons

The spectra displayed in Fig. 4.13 show the appearance of a peak at about 13.5° dispersing slowly towards the point of maximal binding energy at 22.3°. This angle corresponds to the border of the SBZ or the projection of the L-point of the bulk BZ onto the (111)-surface. At higher angles, a slow upward dispersion is observed. The spectra have been taken with the unmonochromatised lamp. Using the monochromatised source, the peaks appear only if excited with p-polarized light. The initial state belongs, therefore, to a wavefunction with even symmetry under reflection at the mirror plane. In accord with band structure calculations it can be attributed to the electron band with even L_4-symmetry at the border of the BZ [85,86]. A second band is observed at slightly higher binding energy. Its dispersion is roughly parallel to that of the electron band. No evidence of a band with expected mirror-like dispersion [67] was found around the $\overline{M}$ point. The next observation is the peak intensity

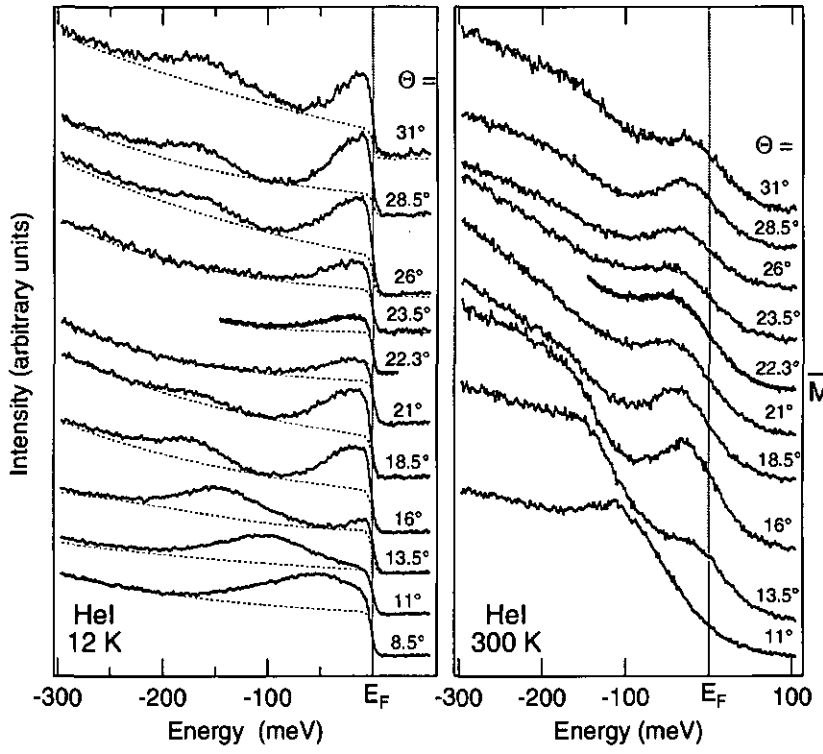

Figure 4.13: *Left (right) panel: series of selected spectra around the $\overline{M}$ symmetry point, taken with unpolarized HeI photons at 12 K (300 K) in the $\Gamma TULX$ bulk mirror plane. Θ gives the emission angle with respect to the surface normal. The dashed lines underneath the spectra denote the featureless background. The low temperature spectra were normalized to the integral background intensity, the spectra at 300 K accordingly.*

which diminishes at the $\overline{M}$ symmetry point. The second band observed in the spectra even vanishes at this angle indicating that, probably, a gap in the final state bands opens up at the zone boundary corresponding to $\overline{M}$. Attempts were made to measure the dispersion perpendicular to the symmetry plane by direct imaging of the second detector dimension, but the strong dispersion could not be resolved in angle. Spectra were taken (not shown here) showing a small hump right on the Fermi level which vanishes about 2° off the symmetry plane.

Thus, at a first glance, the measured electron band resembles to what is expected from band structure calculations and measurements of the bulk Fermi surface. Centered at the border of the SBZ, it disperses in a quasi-parabolic manner towards the Fermi energy with the heavy

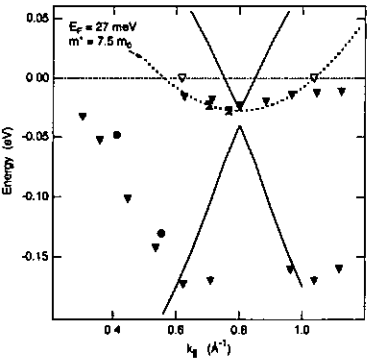

Figure 4.14: *Plot of the peak maxima vs the wave vector $k_{\parallel}$ (solid triangles). Open triangles denote the Fermi momentum at 300 K, circles data from spectra taken with p-polarized light at 12 K. The bulk dispersion of the two bands is indicated by the thick lines. The dashed line corresponds to parabolic dispersion with an effective mass of 7.5 m_0. It is obvious that the effective mass along the bisectrix is much higher than that of the bulk.*

mass direction along tbe bisectrix in the mirror plane (Fig. 4.14). The transversal effective mass, i. e. along tbe binary axis of tbe crystal lattice, is several orders of magnitude smaller. A comparison with Table (4.2) , however, shows that the beavy mass is much larger than the values found for tbe bulk electron band. Furthermore, the spectra at 300 K reveal that the Fermi wave vector does only slightly depend on temperature over the whole temperature range.

4.5.3 Temperature Dependence

Additional information about the dispersion of the electron band can be obtained from the temperature dependence of tbe electron Fermi energy. Tbe change of the Fermi energy with the temperature gives some rough indication of the energy gap between the two bands at the L-point ($\overline{\mathrm{M}}$) and tbe effective mass tensor [67]. In our experiment, the electron Fermi energy is measured as the initial state binding energy relative to E_F at the $\overline{\mathrm{M}}$-point. Spectra, taken at 12, 60 and 300 K are displayed in Fig. 4.15. The background, as extrapolated from valence band spectra at higber binding energies, is indicated as dashed line. The peak shapes were then fitted witb lorentzians, multiplied with tbe Fermi function, for the low temperature spectra. Tbe values found were 24 ± 3 meV at 12 K and 28 ± 3 meV at 60 K, in excellent agreement witb tbose reported for bulk Bi (about 27 meV for $T \leq 80$ K [67]). In tbe higb temperature spectrum, however, the strong background and the thermal broadening render a reliable fitting almost impossible. The most successful, but nevertheless ambiguous, way

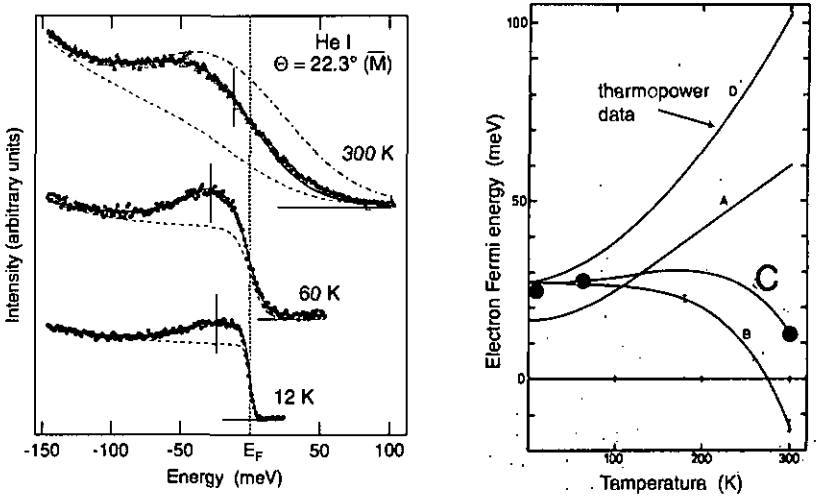

Figure 4.15: *Left panel: spectra at the $\overline{M}$-point (dots), taken with unpolarized HeI-photons at different temperatures. The dashed line under the topmost spectrum shows the background, as extropolated from the valence band spectrum at higher binding energy. The fits (solid lines) are described in detail in the text, the vertical lines denote the corresponding initial state energies. The dashed-dotted line in the 300 K-spectrum is the gaussian shape resulting from the fit. Right panel: Plot of the electron Fermi energy vs temperature, calulated for different temperature dependencies of the effective mass tensor (curves A through C) and obtained from measurements of the thermopower [curve D] (from Ref. [67]). Solid Circles denote results of the photoemission data.*

to find the peak position was to divide the spectrum by the Fermi function and to fit the result by a gaussian. In this way, a value of 12 ± 2 meV was found, thus a slight reduction of the occupied band width with increasing temperature. Heremans and Hansen computed the bulk electron Fermi energy assuming different temperature dependencies of the effective mass tensor [67] (see right panel in Fig. 4.15). A value of 12 meV, as found for 300 K, is in agreement with the calculation, if a temperature-independent heavy mass is supposed (curve C in Fig. 4.15). This is in contradiction to results from thermopower data (curve D in Fig. 4.15), which suggest an increase of the bulk electron Fermi energy with increasing temperature [67], but is in accord with the photoemission data along the heavy mass direction presented in the preceding section. Thus, the temperature dependence of the electron Fermi energy together with the observed large effective masses suggest that the dispersion of the electron band is strongly altered at the sample surface.

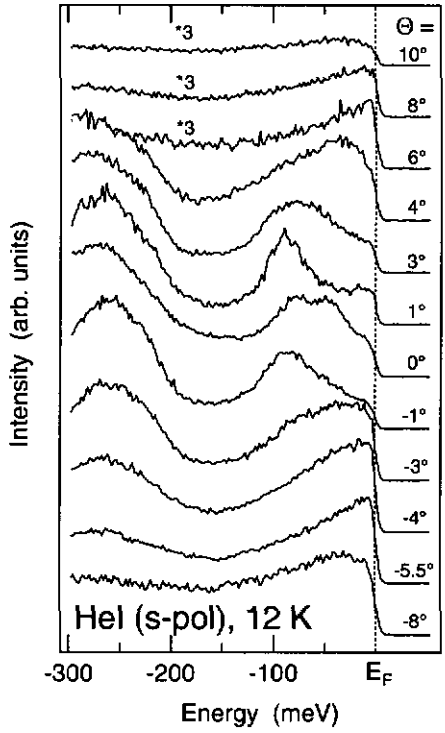

Figure 4.16: *Spectra, taken around normal emission with s-polarized HeI-photons at 10 K; spectra are normalized to the measurement time. The three topmost spectra are enhanced by a factor of 3.*

4.5.4 Holes

The band structure around normal emission is quite complex and contains certainly several features. The most contrasted spectra can be obtained by use of s-polarized light. Some selected spectra are displayed in Fig. 4.16. The spectra were taken at 12 K and are normalized to the measurement time. They show a peak at normal emission moving towards the Fermi level with increasing negative angle (direction $\overline{\Gamma M'}$), crossing E_F at about $-4°$ off-normal and moving back at about $-8°$. For positive angles, a similar behaviour is observed, but with less intensity. The same observations hold for p-polarized light, but the structures are smeared out due to the presence of a strong second peak dispersing in the opposite direction. The initial state contains therefore symmetric and antisymmetric contributions with regard to the mirror plane, as it should be for the bulk hole band (symmetry label λ_{45} [86]). A more figurative view is obtained if the spectra are displayed as greyscale plot with the abscissa and

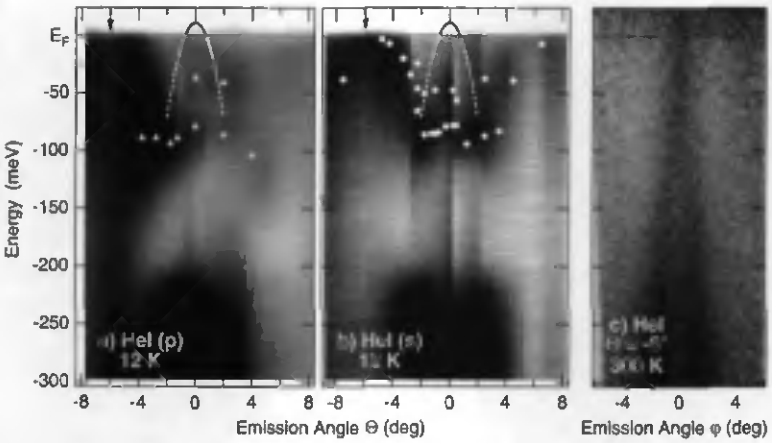

Figure 4.17: *Greyscale plot of spectra (HeI, 10 K), taken around normal emission within along* $\overline{\Gamma M}$ *(see text). a) p-polarized light, b) s-polarized light; black = high intensity; arrows indicate where the picture (c) has been taken. The symbols correspond to peak maxima extracted from the spectra. The dashed line denotes the expected dispersion of the bulk hole band. c) Direct image of the detector, displayed for an emission angle* $\Theta = -6°$. *It represents the dispersion of the band* perpendicular *to the measurement plane (unpolarized light, 300 K).*

ordinate corresponding to the emission angle and binding energy, respectively (Fig. 4.17a and b). Some of the spectra have been interpolated in order to get a continuous picture. The calculated dispersion of the bulk hole band was added as dashed line for comparison. The intensity seen around normal emission at energies below -200 meV stems from the surface state in the spin-orbit gap [95]. It is obvious that the state near the Fermi level is centered *off* normal emission for negative angles. The band has a negative effective mass as shown in Fig. 4.17c by a direct image of our detector in the direction perpendicular to the symmetry plane (emission angle $\Theta = -6°$, indicated by arrows in parts a and b). The image was taken at 300 K and reported on a logarithmic scale in order to follow the dispersion as far as possible beyond the Fermi energy. In a parabolic approximation, the dispersion corresponds to an effective mass of about $-0.04\, m_0$. The same holds for the opposite direction $\overline{\Gamma M}$, whereas no indication for a bulk-like hole band is found.

Finally, in order to establish the symmetry of the found Fermi surface and to exclude a possible sample misalignment, a Fermi surface mapping was carried out (Fig. 4.18). It was recorded with *s*-polarized HeI-radiation at 12 K, integrating over an energy window of 20 meV centered at the Fermi energy. It shows three intense ellipsoids elongated within the mirror planes in $\overline{\Gamma M}'$-direction and an analogue set related by inversion at the $\overline{\Gamma}$-point with

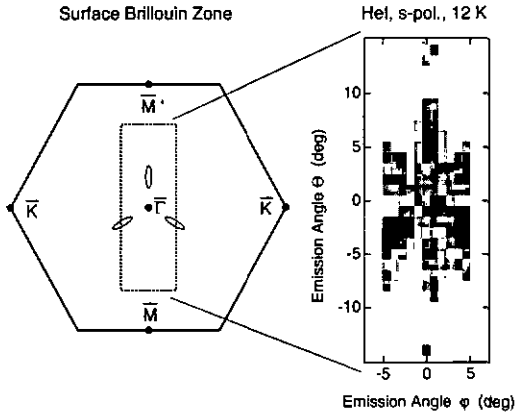

Figure 4.18: *Fermi surface mapping of the hole surfaces. The photoemission intensity (right panel) at E_F (energy window ±10 meV, s-polarized HeI photons, 12 K; black = high intensity) was probed as function of emission angle, corresponding to momenta within the dashed rectangle on the left-hand-side. Three ellipsoids with high intensity and a similar set, rotated by 180° around the trigonal axis, are observed.*

weaker intensity. The surface has *a priori* no inversion symmetry, nor exists a reciprocal lattice vector to relate the two sets via *umklapp* scattering. The presence of the second set indicates that contributions of at least the two topmost bilayers must participate in the formation of the surface hole band, since one bilayer possesses trigonal symmetry (see Fig. 4.2). This explains at the same time the difference in intensity between both sets.

4.5.5 Surface Electronic Structure of Bi(111)

Summarizing the results of this section we can propose a band structure for the Bi(111)-surface, which is displayed in Fig. 4.19 beside the projection of the bulk band structure. Effective mass and Fermi wave vector of the electrons are much larger than the corresponding bulk values. Although no information is available on the third dimension of the Fermi surface, the suggestion of a much higher carrier density for the surface seems to be reasonable.
The measured Fermi surfaces are very similar to the Fermi surfaces of bulk Sb (Fig. 4.6), i.e. six hole pockets in the reflection planes and large electron pockets around the L-points of the bulk BZ [85,109]. The only difference between the Sb and the Bi crystal lattice apart from the inter-atomic distances is the deviation from the cubic structure, larger by roughly 4% for Sb than for Bi. Supposed that the topmost layer of the Bi surface departs somewhat from its *ideal* structure by a slight relaxation of the surface atoms, the surface electronic structure of Bi could become to a certain extent "antimony-like". Since the carrier density in bulk Sb

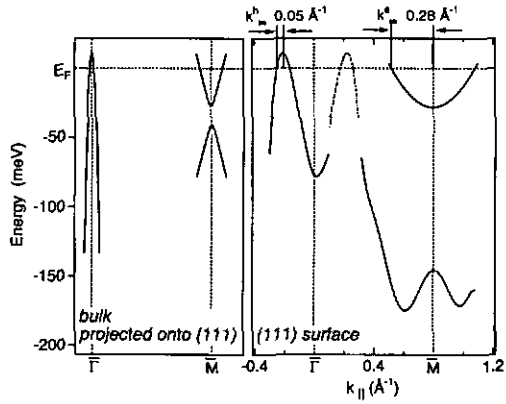

Figure 4.19: *Comparison of the bulk band structure of Bi, projected onto the (111)-surface, and the propased surface band structure. The grey parts of the bands could not be observed in our experiment. The dashed-dotted line is related to the hole band by inversion symmetry and is seen as weak feature in the spectra.*

is roughly two orders of magnitude higher than that of bulk Bi, our results could explain the high density of states on the Bi surface [95]. This is partially confirmed by calculations of the surface electronic structure [113] using the Green's function transfer method [116]. The authors conclude that " ... if we do not allow any kind of relaxation we do not obtain bona fide surface states".

The heavy effective mass of the electron band along the bisectrix can be understood on rather intuitive grounds. If the motion of the electrons is interpreted as hopping between nearest neighbour sites, the second nearest neighbours provide a non-negligible contribution. As can be seen from Fig. 4.2, the second nearest neighbours sit in adjacent bilayers. The hopping is done via the longer inter-layer bonds. The latter are broken at the surface, decreasing by this the hopping probability. Supposing parabolic dispersion, this yields an increase of the effective mass in the surface layer as observed in the PE spectra. On the same level, one could interpret the changes of the hole dispersion. The orbital character of the relevant band is mainly p_z. Due to the breaking of the longer bonds, the p_z dangling bonds rearrange, and the mobility diminishes considerably. As a direct consequence, the band width almost vanishes. The hole band can be observed over an energy range of about 170 meV between $\bar{\Gamma}$ and the $\bar{M}$-point. Some tens of meV are certainly a reasonable approximation for the width in the unoccupied part, yielding roughly 200 meV of total band width. This, compared to about 2.6 eV for the bulk band [104], gives evidence for surface character of the carrier bands.

4.6 Sb(111)

As for Bi, the plane of interest corresponds to the bulk mirror plane. The corresponding cut through the BZ, ΓTLUX, and its projection onto the (111)-surface are shown in Fig. 4.20a. A sketch of the carrier band structure is given in Fig. 4.20b. The hole band is centered at the H-point of the bulk BZ, the corresponding point of the SBZ was named $\overline{\mathrm{H}}$ for the sake of simplicity. The parameters important for the PE experiment are given in Table 4.4. The

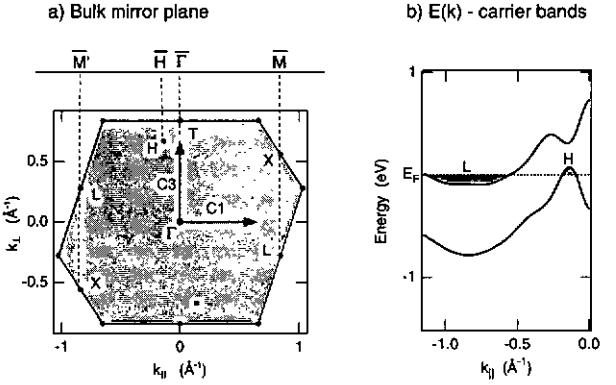

Figure 4.20: *a) Cut through the bulk BZ of Sb and its projection onto the (111)-surface. The H-point is the centre of the hole surface. b) Anticipated carrier band dispersion with $k_{\|}$, based on bulk calculations along high-symmetry directions. The electrons at L and holes at H are emphasized by shaded pockets.*

Table 4.4: *Some parameters for the (111)-surface used for the photoemission experiments.*

parameter	Sb(111)
work function (polycrystal, Ref. [115])	4.55 eV
Debye temperature (bulk, Ref. [97])	211 K
distance $\overline{\Gamma\mathrm{M}}$ (centre of the electron FS)	0.843 $\mathrm{\AA}^{-1}$
centre of the hole FS	$\approx$0.249$\mathrm{\AA}^{-1}$ ($\overline{\mathrm{H}}$-point)
distance $\overline{\Gamma\mathrm{K}}$	0.973 $\mathrm{\AA}^{-1}$

exact location of the H-point in the BZ is not known, since the usual methods to study the Fermi surfaces are only sensitive to shape and orientation of the surfaces [109]. Published band structure calculations predict different coordinates [68,85,88,104]. In the following the coordinates given by Liu and Allen [104] have been chosen since their calculation will be

compared to the experimental data.

4.6.1 Valence Band Structure

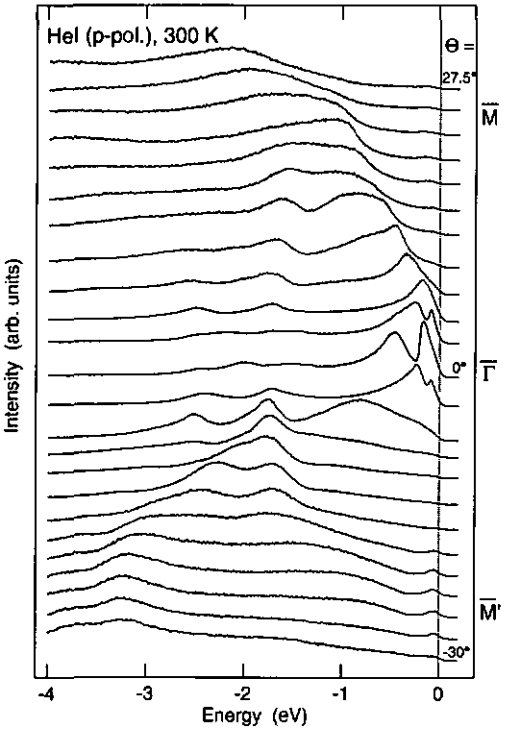

Figure 4.21: *Valence band spectra, taken with p-polarized HeI-photons at 300 K along the $\overline{\Gamma M}$-direction. Spectra are normalized to the same total intensity for the sake of clarity. The difference in angle between two spectra is 2.5°.*

The electronic structure of Sb is very similar to that of Bi except for the carrier bands. Figure 4.21 shows valence band spectra, taken along the $\overline{M'\Gamma M}$-direction of the SBZ. No angle-resolved PE study of Sb is published to the best of my knowledge, in particular no study making use of synchrotron light with variable photon energy. Attempts to take spectra with HeII-photons have failed for reasons of intensity. Thus, the attribution of the observed peak to bulk or surface states is less straightforward than in the case of Bi. The bulk band structure was computed in the same way as for Bi, using again the tight-binding scheme [104]. The

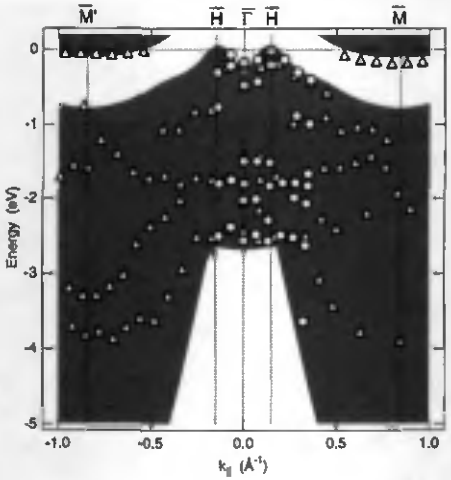

Figure 4.22: *Bulk band structure calculated within the tight-binding model [104]. Shaded areas correspond to dispersion of the bulk bands perpendicular to the (111)-surface. Experimental data points (HeI, p-polarized) are plotted as symbols vs $k_{\|}$ for 12 K (open circles) and 300 K (open triangles).*

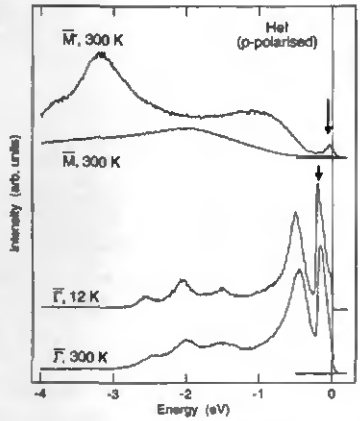

Figure 4.23: *Extended spectra, taken with p-polarized HeI-radiation at 300 K at the symmetry points, indicated in the figure. The arrows denote the features of the carrier bands (see text for details).*

dispersion of the peak maxima with $k_{\|}$, extracted from the spectra, taken at 12 K (spectra not shown) and 300 K with p-polarized light, is plotted in Fig. 4.22. Superimposed is the projected bulk band structure, given by the grey shaded area. The overall agreement is quite

good. Like in the case of Bi, we will focus our attention on the actual carrier bands around $\overline{\Gamma}$ and $\overline{M}/\overline{M}'$. Extended valence spectra at these symmetry points are depicted in Fig. 4.23. Arrows indicate the features, which will be discussed in the subsequent sections.

4.6.2 Electrons

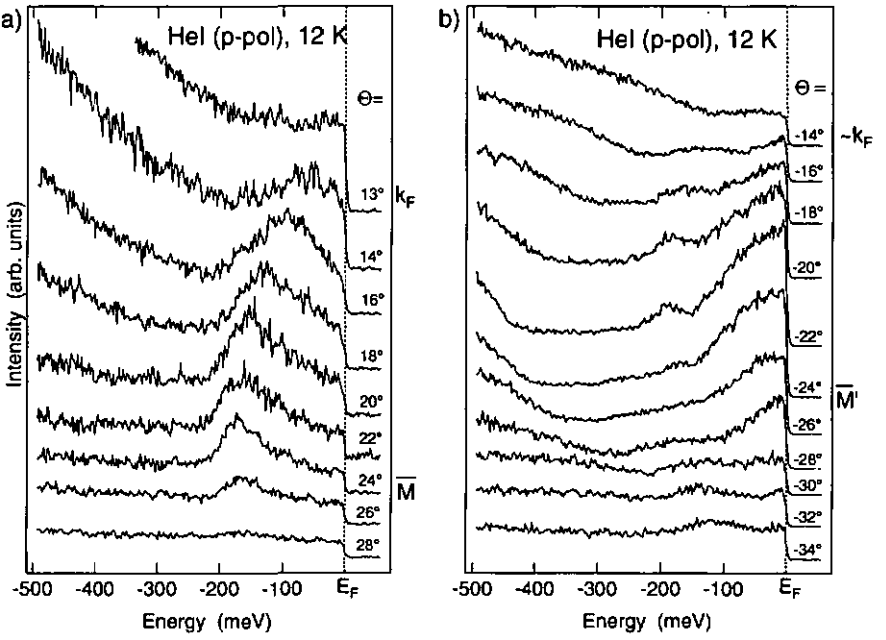

Figure 4.24: *Spectra around the symmetry points $\overline{M}$ (left ponel) and $\overline{M}'$ (right panel), taken with p-polarized HeI-radiation at 12 K. Each set of spectra has been normalized to the measurement time. The symmetry points and the approximate location of the Fermi level crossing are indicated.*

Photoemission intensity close to E_F can be found at both, the $\overline{M}$- and the $\overline{M}'$-point of the SBZ. High-resolution spectra, taken within the mirror plane around these points, are displayed in Fig. 4.24. We start with the analysis at the $\overline{M}$-point (left panel in Fig. 4.24). The spectra show the appearance of a weak structure at E_F at 13°, which disperses slowly toward higher binding energies and reaches its maximum binding energy at 24°. The latter angle corresponds to the border of the SBZ ($\overline{M}$). For higher angles, it disperses back towards the Fermi energy. Like in the case of Bi, we attribute this band to the electron pocket due to its even symmetry [85] and the observed location and dispersion [68, 85, 104]. The same

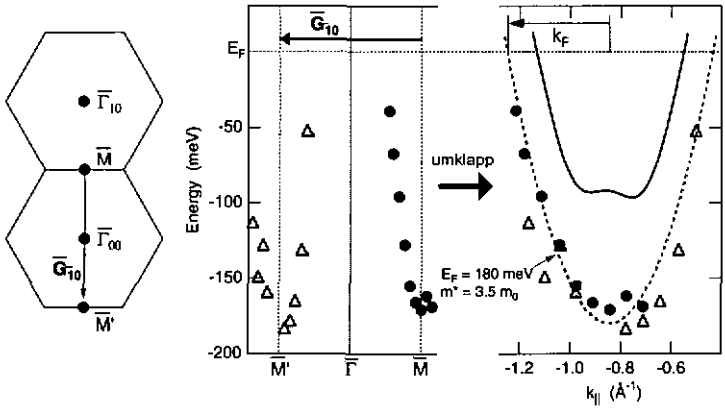

Figure 4.25: *From the left to the right: SBZ in the extended zone scheme with the reciprocal lattice vector $\overline{G}_{\overline{1}0}$; peak maxima, found in the spectra of Fig. 4.24 around the two symmetry points; idem, but with the peak maxima at $\overline{M}$ displaced by a reciprocal lattice vector (surface umklapp). Solid and dashed lines in the right panel respectively denote the bulk electron band and a parabolic band with effective mass of 3.5 m_0.*

behaviour can be observed in the opposite direction around $\overline{M}'$, but only as a small peak on the high-binding energy side of a strong feature at E_F. If the binding energy of the observed peaks is plotted versus the parallel component of the momentum, the dispersion plot in Fig. 4.25 is obtained. The calculated bulk band dispersion and a free-electron-like parabola ($E_F = 180$ meV, $m^* = 3.5m_0$) are superimposed. The weak peak, which is attributed to the expected electron band, shows nearly parabolic dispersion. As in the case of Bi, this peak is observed at $\overline{M}$ and $\overline{M}'$. A surface *umklapp* process can be invoked, because $\overline{M}$ and $\overline{M}'$ are just separated by a surface reciprocal lattice vector, as shown in Fig. 4.25. Concerning the effective mass, the agreement between experiment and theory is quite good, whereas the experimentally found Fermi energy is about the double of that given by the calculation. Extrapolation of the dispersion to the Fermi energy yields a Fermi wave vector of 0.37-0.4 Å^{-1}, thus only slightly higher than the bulk value (0.3 Å^{-1} [109]).

The origin of the strong feature at E_F, observed in spectra taken at the $\overline{M}'$-point (Fig. 4.24), is less clear. The fact that the peak is not observed at $\overline{M}$ may be explained by effects of the optical matrix element. The latter changes due to the sample rotation, if p-polarized light is employed. A second possibility is the quality of the sample surface, which exhibits several domains. Due to our experimental geometry, different areas of the sample surface are probed, when the sample is rotated. Moreover, it was found that the spectral shape of the peak is not altered if the angular resolution or the sample temperature are varied. The form of the peak is reminiscent of a square-root function, similar to a 3D-DOS, and

the feature may be tentatively attributed to non-k-conserving transitions. The final answer must, however, await further experiments.

4.6.3 Holes

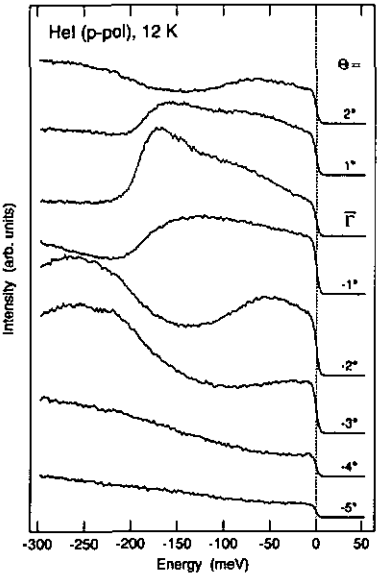

Figure 4.26: *Near-E_F spectra (HeI, p-pol, 12 K) taken around normal emission in direction $\overline{M}\overline{\Gamma}\overline{M}$. The spectra are normalized to the measurement time.*

Figure 4.26 presents low-temperature spectra, taken close to normal emission within the mirror plane. A broad feature can be seen at $\overline{\Gamma}$ with an intensity maximum at about 180 meV binding energy. The large width and the apparent double structure result probably from the angular resolution, which is insufficient to resolve the strong dispersion perpendicular to the mirror plane. Off normal emission, the observed peak approaches the Fermi energy and reaches E_F in the spectrum taken at -3°. An further increase of the emission angle results in a rapid decrease of spectral intensity suggesting that the peak crosses E_F. Due to location, symmetry and dispersion, the feature can be identified with the hole band of Sb. It was checked that the dispersion perpendicular to the mirror plane corresponds to that expected for a hole band (negative effective mass).

In order to measure the extent of the hole FS, a series of spectra was taken at room temperature. The thermal broadening of the Fermi function allows the peak dispersion to be

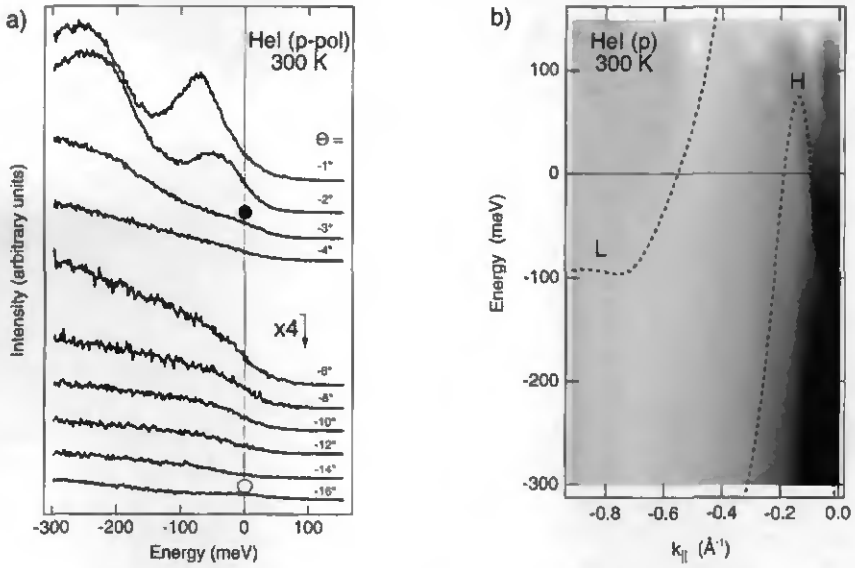

Figure 4.27: *a) As Fig. 4.26, but at 300 K in direction $\overline{\Gamma M}$. The solid black dot denotes the crossing of the Fermi level by the hole band, the open circle at $\Theta = -16°$ the appearance of the electron band. b) Same spectra as in (a), presented as contour plot with logarithmic intensity scale (black = high intensity). The calculated carrier bands (dashed lines) have been added.*

followed far above E_F [117]. A selection of spectra is shown in Fig. 4.27a. They are normalized to the measurement time. The Fermi level crossing of the hole band is indicated by a black dot. No pronounced second crossing, which is expected from a band dispersing back into the occupied part, is visible in the spectra. The weak peak appearing at E_F for $\Theta = -16°$ (open circle), which is barely discernible on this intensity scale, was identified as the electron band, discussed in the preceding section. However, it can not be ruled out that both observed bands belong to one single state. In Fig. 4.27b, the same spectra are presented as a contour plot as function of energy and momentum. The intensity scale is logarithmic in order to compensate for the Fermi function. Again, no second crossing of the hole band can be found in this representation.

Up to now, the bulk Fermi surfaces of the holes have been treated as isolated pseudo-ellipsoids. Arsenic, the group-V element above Sb in the Periodic Table of Elements, has many features in common with Sb. The hole Fermi surface of As is similar to that of Sb, except for some ring-like structure, which connects all ellipsoids within the BZ (see Fig. 4.28). These necks appear in the bulk band structure as Fermi level crossing on the TW-line [68,84].

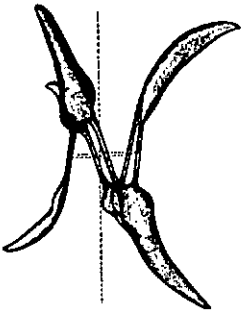

Figure 4.28: *Perspective view of the hole Fermi surface of Arsenic. The vertical dashed line is the trigonal axis, the "pepperoni"-like surfaces lie in the mirror planes (from Ref. [118]).*

In Sb, no crossing should be found for the TW-direction of the bulk BZ. Falicov and Lin discuss the effect of spin-orbit coupling on the band structure around the T-point and find that the inclusion of LS-coupling opens a gap at E_F for wave vectors along TW [85] (see Fig. 4.29). However, no experimental evidence for the absence or presence of these necks in Sb has been found, since in conventional Fermi surface measurements, like de Haas-van Alphen-experiments, these necks are difficult to detect due to their very long period [118] (see the discussion in Ref. [109]).

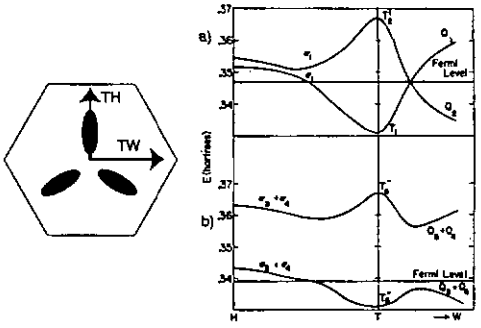

Figure 4.29: *Calculated dispersion of the 5th and 6th valence bands band along TW ($\overline{\Gamma K}$) and TH ($\overline{\Gamma M}$) (directions sketched in the left part): a) without spin-orbit coupling, b) including spin-orbit coupling. In the latter case, no crossing of the Fermi level should be found perpendicular to the mirror plane (direction $\overline{\Gamma K}$). From Ref. [85].*

The tight binding calculation of Liu and Allen fails to reproduce correctly the shape of the

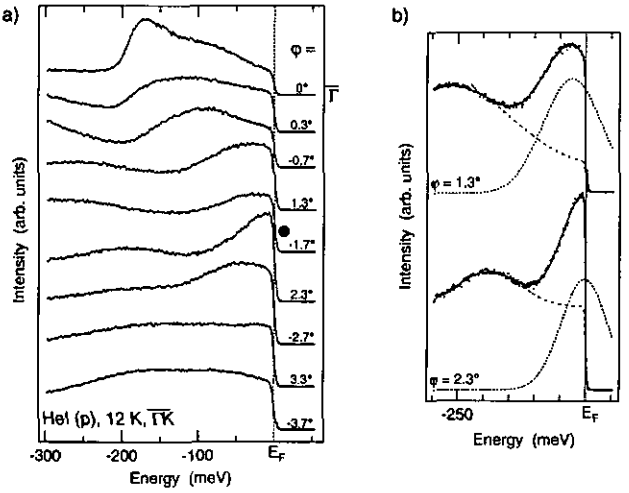

Figure 4.30: *a) High-resolution spectra in the direction $\overline{\Gamma K}$ (HeI, p-pol, 12 K). Note that spectra, taken at negative and positive emission angles, are presented in series. This is allowed because of the mirror symmetry of the crystal with respect to the $\overline{\Gamma M}$-line ($\Theta = 0$). A solid circle indicates the spectrum, where the peak probably crosses E_F. b) Two selected spectra (dots), taken from (a) and fitted with gaussian peak shapes (dotted lines) after subtraction of the background (dashed line).*

hole FS, as stated by the autbors [104]. They obtain even a crossing of the Fermi level for wave vectors along TW, but they do not discuss this point. Tbe direction TW corresponds to $\overline{\Gamma K}$ of the SBZ, thus tbe direction perpendicular to the mirror plane. Making use of the second detector dimension, spectra have been taken for a few angles from normal emission towards $\overline{K}$. A series of high-resolution spectra, taken at low temperature, is presented in Fig. 4.30a. The spectra have been normalized to the measurement time. It was checked that the peak dispersion was symmetric with respect to the mirror plane. We are therefore allowed to plot spectra, taken in both directions $\overline{\Gamma K}$, as series in emission angle irrespective of the sign of φ.

From Fig. 4.30a, we can see a peak to disperse from its bottom at $\overline{\Gamma}$ towards E_F. The peak maximum seems to cross the Fermi energy between $\varphi = 1.3°$ and 1.7°(spectrum marked by a black bullet), evidenced by the sudden intensity drop at E_F in the spectrum, taken at $\varphi = 1.7°$. In the following spectrum ($\varphi = 2.3°$), the peak is situated at E_F. The lineshape can be fitted by a gaussian after subtraction of some background, as shown in Fig. 4.30b. The dispersion of the peak for emission angles higher than 2.7°is difficult to discern due to the strong intensity of a feature at higher binding energy. Summarizing, these results give evidence for an unpredicted Fermi level crossing in the direction $\overline{\Gamma K}$ of the SBZ. Further

support of the crossing is obtained from valence band spectra taken at room temperature (spectra not shown here). The topology of the hole Fermi surface may therefore be similar to that of As.

4.6.4 Surface Electronic Structure of Sb(111)

In conclusion, the electronic structure of the Sb(111)-surface is in extensive agreement with calculations and experiments probing the bulk band structure. The hole band seems to deviate from the bulk band, but the spectra and previous experiments are finally little conclusive. In order to establish a complete picture of the shape of the hole Fermi surfaces, a Fermi surface mapping with variable photon energy is necessary. On the other hand, the observed electron band agrees in location and effective band mass with the precisely measured bulk Fermi surface and with band structure calculations. The occupied band width is slightly larger than predicted. The origin of the strong DOS feature at E_F could not be identified. Similarly to the case of Bi, one could invoke an inward-relaxation of the surface atoms. As a consequence, the lattice of the surface could approach the more distorted As-structure, explaining some apparent changes in the electronic structure. An overestimation of the importance of spin-orbit splitting in previous calculations could be quoted as second possibility to explain the observed hole Fermi surface.

4.7 Bismuth and Antimony in Mesoscopic Dimensions

I will address now the question whether these elements are suitable candidates for photoemission studies of low-dimensional metals. For such studies, the electron band is certainly more interesting than the hole band. In both cases, Bi(111) and Sb(111), it was found that the topology of the electron Fermi surface is preserved at the surface, i.e. it consists of elongated ellipsoids with the heavy mass direction roughly along the bisectrix. The electron density at the surface is higher than in the bulk, but still very small in comparison to typical metallic electron densities. Antimony is probably the better choice for photoemission measurements on metallic wires. The necessary dimensions can be estimated to a good approximation from the well-known bulk Fermi surface. This yields a lateral wire dimension in the order of 25 Å, i.e. about 8 inter-atomic spacings, if the wire direction coincides with the bisectrix of the crystalline lattice. The band width, much larger in Sb than in Bi, allows the dispersion to be followed over a sufficient range in energy and momentum.

Chapter 5

Step Potentials on Vicinal Surfaces: Barriers for Surface States

5.1 Short Review of Surface States and Goal of our Experiment

Electronic states are usually obtained by solution of the Schrödinger-equation. If the crystal dimensions are taken to be infinite, the momentum of the electrons is a real vector. As a consequence of the periodic crystal potential, energy gaps open up between bands at the boundaries of the BZ. For energies within these gaps, the Schrödinger-equation has no solution. Due to the presence of a bulk termination, new states appear, whose energies lie within the gaps, and whose momenta possess a complex component perpendicular to the surface. The imaginary part describes the decay of the wave function inside the crystal. If the wave function amplitude vanishes inside the crystal, the new states are called "bona fide" surface states, if the amplitude reaches a finite value, they are called surface resonances [51]. Due to the finite amplitude in the bulk, the latter hybridize with bulk states. Energies and wave functions are schematically shown in Fig. 5.1. For the bona fide surface states, it became customary to make a distinction between Tamm states and Shockley states, depending on the model, which describes the crystal potential and the wave functions near the surface [119]. Tamm used a Kronig-Penney model with a boundary [120], a situation, which applies to tightly bound electrons like *d*- and *f*-like states [32]. He showed that, if the surface perturbation is "strong", states split off from the bulk states due to the surface potential shift. Some criteria, which are used to define the term "strong" can be found in the review of Davison and Levine [119]. For our purpose, it is sufficient to note that Tamm states can only exist in bulk band gaps opening up at boundaries of *odd*-numbered zones [119]. In contrast to Tamm's work, Shockley considered a nearly-free electron model [121]. He showed that surface states appear, if the potential corrugation at the surface is *weak*, but the bands

enclosing the band gap have certain symmetries. One then speaks of Shockley-inverted band gaps with p-like states at the lower and s-like states at the upper limit of the gap (sometimes named hybridization gaps [33,122]).

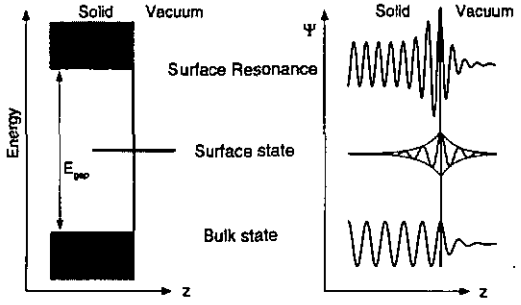

Figure 5.1: *Schematic representation of surface states and resonances. z is the spatial coordinate perpendicular to the surface. The binding energy of a surface state lies within a bulk band gap (left panel); its wave function decays exponentially inside the bulk and in the vacuum and shows a pronounced maximum at the surface (right-hand-side). Surface resonances appear due to a resonant enhancement of bulk states at the surface.*

Due to their localization in the outermost layers surface states are very sensitive to defects or superstructure at the crystal surface. Surfaces cut from a crystal with a small miscut from a low Miller index direction, can exhibit large terraces usually separated by monatomic steps. The steps are running perpendicular to the miscut direction. This type of surface is named vicinal to the low-index surface. Motivation for the study of surface states on such surfaces comes from different quarters. Step sites may be catalytically more active than normal terrace sites [123,124]. Ferromagnetic thin films on stepped surfaces have been shown to yield a fixed orientation of the magnetic moment along the steps ("easy axis") [125]. Submonolayer coverages of metals on vicinal surfaces may lead to the development of atomic chains allowing one-dimensional behaviour to be studied [23,65,66]. This, and the hope that a regular step array may lead to the observation of one-dimensional surface states associated with the step sites [126,127], have helped fuel interest in vicinal surfaces. However, it is only relatively recently that the quality of sample preparation necessary to produce convinciog results has been achieved. This question of sample quality has undoubtedly been helped by the development of the scanning tunneling microscope.

The Cu(100)-surface supports a well known Tamm-type surface state, which is localized in the topmost layer. It shows practically no interaction with the bulk states and, consequently, the previously measured lifetimes of the photohole are extremely long. The idea of our

experiment was, therefore, to study the behaviour of this state in a regular step array. The step superstructure has been found to be thermodynamically stable on Cu(610) and Cu(811) [127], cut at roughly 10°from Cu(100) toward [010] and [011], respectively. Taking into account the geometry of our experiment and the fact that we want to examine the electron dispersion perpendicular to the steps, the (610)-surface is employed in this study. We will make use of the (811)-surface for comparison only. Of particular interest were the lineshape and the existence of split-off states due to the modified surface potential. Most of the results presented in this section have been published in Ref. [26]. Similar experiments have already been carried out on Cu(410) [128] and recently on Cu(610) [129]. In both cases, a peak was found for emission angles corresponding roughly to the $\overline{\mathrm{M}}$-point of the flat surface, shifted by the angular misfit. The peak exhibits no dispersion in the direction perpendicular to the step edges [128,129]. It was shown to be the analogue of the Cu(100)-Tamm state. Furthermore, in agreement with results from our study, transitions from bulk states have been shown not to be affected by the superlattice [33,128,129].

5.2 Surface Mesh and Brillouin Zone

Copper crystallizes in the fcc-structure. We take a non-primitive unit mesh of the (100)-surface, defined by a square lattice with one atom in the center (Fig. 5.2a). The corresponding bulk lattice constant equals $a = 3.615$ Å along the crystallographic directions [010] (x) and [001] (y) [130]. The surface was shown to reconstruct by a slight in-plane contraction of about 1-2% with respect to the bulk lattice [131,132], yielding a surface lattice parameter $a_s = 3.58$ Å [131]. The vicinal surfaces (N10) and (N11) can be represented as superstructure of monatomic steps running along [001] and [0$\overline{1}$1], respectively. The relationship between step height h, terrace width w, and miscut angle γ is given by $\tan\gamma = h/w$. Assuming $h = 1.8$ Å (monatomic steps) and $\gamma_{610} = 9.5°$, we obtain for the (610)-surface $w = 10.75$ Å, or a width of 6 atomic rows. For the (811)-surface ($\gamma_{811} = 10°$) this yields $w = 10.2$ Å or 4 atomic rows. The corresponding surfaces, as seen from the terrace normal [100], are displayed in parts (b) and (c) in Fig. 5.2. Note that the steps on the (811)-surface run along a close-packed direction of the fcc-lattice.

Figure 5.3 shows the (610)-surface in a ball-and-sticks model. The surface retains only one symmetry plane, (001), which is indicated. Spectra taken with the emission angle lying within this plane, correspond to the dispersion of the surface state perpendicular to the steps. The surface Brillouin zones are plotted in Fig. 5.4. Symmetry points are given in their usual notation (e.g. Ref. [31]). The step superlattice induces new reciprocal lattice vectors perpendicular to the step edge direction. The $\overline{\mathrm{M}}$-point is given on the flat surface by the coordinates $(0, 2\pi/a_s, 0)$.

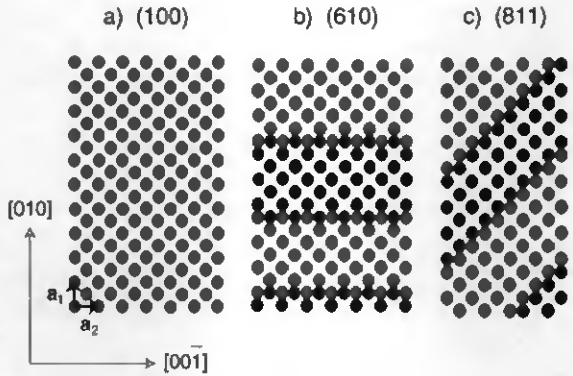

Figure 5.2: *Bird's-eye view of the atomic structure of different Cu surfaces; a) Cu(100), b) Cu(610), and c) Cu(811), as seen from the [100] direction. Unit mesh vectors* $\mathbf{a}_1$ *and* $\mathbf{a}_2$ *are indicated for Cu(100). Black and grey shaded atoms belong to different (100)-layers.*

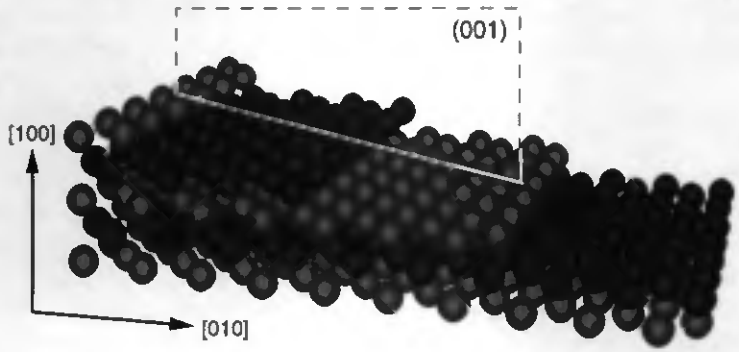

Figure 5.3: *Perspective view of the (610)-surface. Crystallographic directions and the (001)-symmetry plane are indicated. Different colour shading refers to different (100)-layers.*

5.3 Sample Preparation and LEED Analysis

All samples were mechanically polished with diamond paste of grain size 0.25 μ. Prior to introduction into the vacuum system they were given a careful electropolishing treatment.

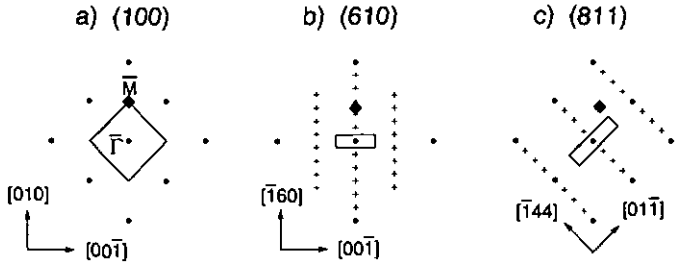

Figure 5.4: *Surface Brillouin zones of 3 surfaces: a) Cu(100), b) Cu(610), and c) Cu(811). Lines denote the SBZ, dots $\overline{\Gamma}$-points, common to all surfaces, and crosses reciprocal lattice points of the step superlattice. The diamonds represent the projection of the X_{110} onto the surface, e.g. $\overline{M}$ for Cu(100).*

This removes damage arising from the mechanical polishing of the sample and results in a surface requiring minimum *in situ* treatment. The acid solution used consisted of 63 vol% ortho-phosphoric acid (concentration 85%), 9 vol% sulfuric acid (conc. 98%), and 28 vol% distilled water [133]. A voltage of 1.85 V was applied to the samples with respect to a Cu cathode. The current density of about 1-1.8 mA/mm^2 at the beginning decreases and stabilizes after 2 mins at 0.3 mA/mm^2. The duration of the electro-chemical polishing was limited to about 2 and a half minutes. After that, the surface had mirror finish, and the sample was immediately inserted into the vacuum system. *In situ*, the preparation comprised standard sputter (Ar^+, 0.6-1 keV, 15-30 mins) and anneal cycles. The annealing temperature was higher for the vicinal surfaces (about 650-670°C, 30 mins) than for the (100)-surface (about 580°C, 30 mins). Moreover, after the anneal, slow cooling down to room temperature (30 mins) turned out to improve the quality of the vicinal surfaces. The level of surface contamination was checked by means of Auger spectroscopy and XPS.

LEED was used to verify the surface structure. From the vicinal faces, clearly split double spots were observed, consistent with a regularly stepped surface structure [128, 135]. The extinction of other superstructure spots is the consequence of the structure factor [51, 128, 135]. An image taken from such a pattern is displayed in Fig. 5.5a. It was shown that analysis of the spot profiles (SPALEED = spot profile analysis LEED) can be used to calculate the terrace width distribution [134, 136]. Lorentzians were fitted to the intensity profiles of the split Γ_{020}-spot, as shown in Fig. 5.5b. Distance between and width of the spots give information about the average length and the regularity of the terraces, respectively. We obtain a terrace width distribution of 6±0.5 atomic rows, in agreement with other studies [129,137]. Note that the period perpendicular to the steps reflects the terrace width and the step height due to the translational symmetry of the surface [135]. The surface disorder can be explained by the inherent structure of the rows forming the steps and atomic relaxations

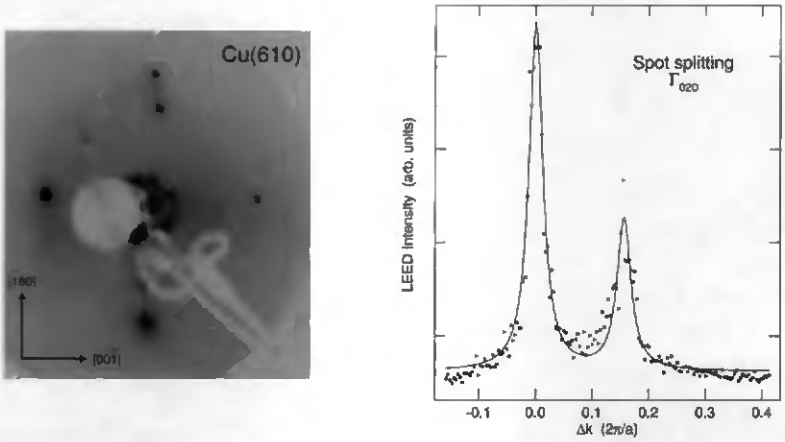

Figure 5.5: *LEED pattern of the (610)-surface. a) Image taken at 300 K using electrons with kinetic energy 89 eV. Steps are running along* $[00\bar{1}]$. *b) Intensity profile (dots) extracted from the pattern in (a) at the split spot at the top [corresponds to* $\bar{\Gamma}_{020}$ *on Cu(100)]. The line denotes the fit of two lorentzians [134], yielding a terrace width distribution of* 6 ± 0.5 *atomic rows.*

at the step edges [132].

As already mentioned above, the step edges on the (811)-surface correspond to close-packed atomic rows, whereas the step structure on Cu(610) is rather "fuzzy". This seems to have important consequences for the stability of the surfaces, as the (610)-surface was found to be highly unstable against surface damage induced by vuv-radiation at low temperature [27]. Deterioration of the surface order was observed as a decrease of the PE signal from the Tamm state within some minutes. The corresponding time scale for the (811)- and (100)-surfaces was considerably longer [27]. Therefore, only spectra from vicinal surfaces, which have been taken at room temperature, will be presented.

5.4 Interfering Electron Waves

In the following, we will first establish some microscopic picture of the charge arrangement at a single step, and then extent this picture to a regular step array. The coordination of surface atoms varies as function of the atom position with respect to the step. In a metal, the free charge will rearrange around the step sites in order to lower the total electronic energy (Smoluchowski-effect, [138]). The potential step is thereby smoothed by the charge distribution [138,139]. Electrons moving in the surface plane feel a potential, which is slightly higher at the steps and acts as repulsive barrier. Their motion can be described in terms of

reflection and transmission coefficients at these barriers [140]. The partial reflection of the wave leads to interference effects which can be well observed as ripples of the charge density in STM measurements [141,142]. One might argue as well in terms of electron hopping. The hopping probability across the step is lower than that between two neighbouring sites on the flat surface. As a consequence, the band width will be decreased, whereas the average potential will be increased. Assuming a free-electron like parabolic dispersion, this leads to an overall shift of the dispersion towards higher energy [143, 144] and to an enhancement of the effective mass. This general trend has been confirmed in various experiments. For example, if we take the width of the surface state, as observed in photoemission spectra, to be indicative of the step density [136], then one finds indeed a strong correlation between width, binding energy, and effective mass of surface states [136, 145].

Reconstruction [146] or angular miscut of surfaces [147,148] may induce an array of equidistant monatomic steps, separated by large terraces. Electrons, moving in the direction perpendicular to the steps, are therefore submitted to a potential with two different periodicities. The atomic potential on the terraces corresponds to the potential on the flat surface and determines the "unperturbed" electron motion in the surface layer. The second period is given by the potential corrugation due to the steps. The Kronig-Penney model [1,97,149] has been invoked to explain the modulation of the electron wave function by the larger step period [140,141,146,150]. In this picture, the steps represent rather permeable barriers allowing contributions to the wave function from adjacent terraces to be coupled by the transmitted part of the electron waves [150]. As a consequence, surface state bands are folded back by the new reciprocal lattice vector due to the superstructure [137, 146, 151]. Calculations carried out for clean and adsorbate-covered vicinal surfaces confirm this view [152]. The authors of this study suggest that no total confinement of surface state electrons is feasible within artificially made structures.

Although such simple models seem to describe the physics of electron confinement, a subtle problem has to be solved concerning the fundamental relationship between the translation vectors of the surface and the Bloch wave vector of the electrons. Invoking the translational symmetry and referring to section 5.2, the wave vector has to refer to the macroscopic surface. In the limit of large terraces, however, we have to come back to the flat surface, where the wave vector lies within the terraces [140–142, 153]. In early photoemission experiments, it was realized that the surface states have to be associated with either the terraces or with the macroscopic surface, depending on the terrace width [154, 155]. Recently, Ortega and co-workers elucidated this point in a systematic photoemission study of vicinal surfaces, covering several miscut angles [156]. A critical angle was found at which the "states switch their character". It is interesting to note that the corresponding terrace width does not coincide with the lateral coherence length of the surface state wave function, estimated from previous work on the corresponding flat surface [136].

5.5 The $\overline{\text{M}}$-Tamm State on Cu(100)

At the $\overline{\text{M}}$-point of the SBZ of Cu(100), the bulk d_{xy}-band reaches a local minimum in binding energy (2 eV). x and y are here rectangular coordinates from the origin to the corner atoms of the fcc unit cell, as defined in section 5.2. The effective band mass is negative at $\overline{\text{M}}$, and the band encloses a 4 eV-wide absolute band gap with an unoccupied sp-band (Fig. 5.6a). $\overline{\text{M}}$ is amongst others the projection of the bulk X_{110}-point onto the (100)-surface (Fig. 5.6b), the latter lying at the intersection of two Bragg-planes, (100) and (010). This location favors the appearance of a split-off d_{xy}-state, localized within the topmost surface layer of Cu(100). As a consequence, a Tamm state appears about 200 meV above the parent d_{xy}-band, dispersing with negative effective mass ($m^* \sim -2m_0$) along $\overline{\Gamma\text{M}}$ [157]. In Fig. 5.7a, a

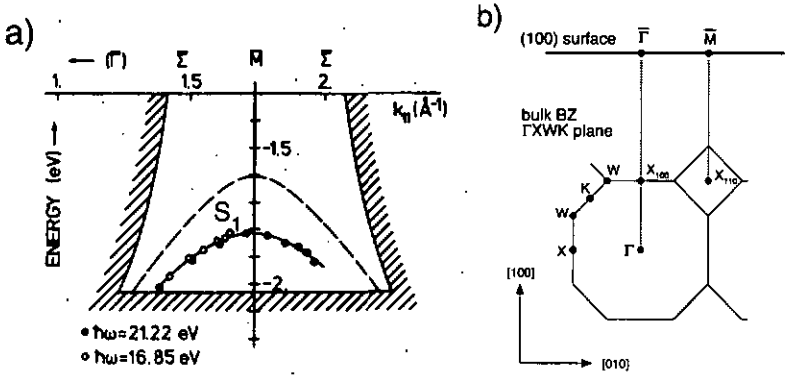

Figure 5.6: *a) Surface electronic structure of Cu(100). The gap in the projection of the bulk band structure is bounded by the hatched area. The line with the data points denotes the dispersion of the Tamm state S_1, the dashed line is the result of an earlier calculation (taken from Ref. [157]). b) Cut through the bulk mirror plane ΓXWK in the extended zone scheme and projection (dashed lines) of the bulk Γ- and X_{110}-points onto the (100)-surface (horizontal thick line above). X_{110} corresponds to the symmetry point $\overline{M}$ of the surface.*

series of spectra, taken previously with HeI-photons along the $\overline{\Gamma\text{M}}$-line of the SBZ, is shown. $\Theta = 62°$ corresponds to emission from the $\overline{\text{M}}$-point (work function ϕ=4.59 eV [32]). The symmetry of the Tamm state wave function with respect to the mirror plane is odd, i.e. the state is observable in a PE experiment using s-polarized light. A spectrum, taken with s-polarized light (HeI, 10 K) from $\overline{\text{M}}$ is depicted in Fig. 5.7b. S_1, B_1, and S_2 denote the peaks of the Tamm state, the parent bulk band, and a second surface state within the spin-orbit gap [158]. The binding energy of the Tamm state is lower by 200 meV than that of the parent bulk band.

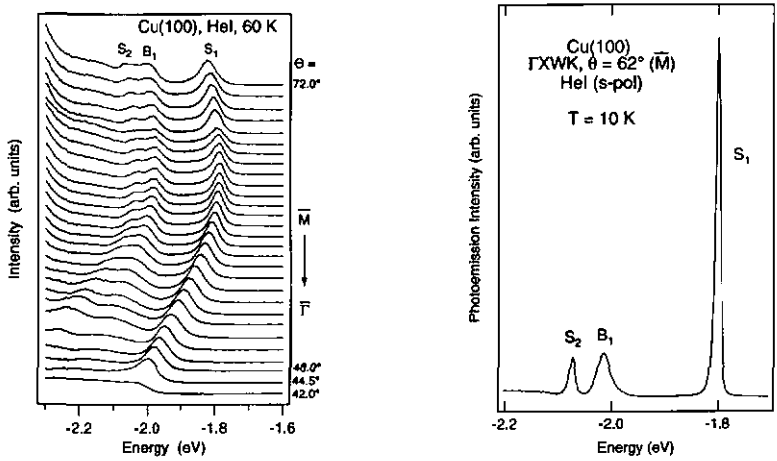

Figure 5.7: *Left panel: ARUPS data from Cu(100) along $\overline{\Gamma M}$ at 60 K, taken with unmonochromatised HeI-light. Note that these spectra have been taken from another sample (D. Purdie, 1995, unpublished results). Between 46° and 72°, angular steps are 2°. Right panel: data from Cu(100), taken at $\Theta = 62°$ with s-polarized HeI radiation. The spectrum was recorded at 10 K. The labels of the peaks are referred to within the text.*

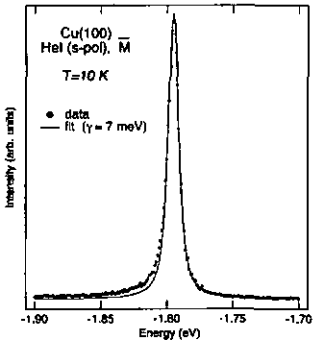

Figure 5.8: *The $\overline{M}$ Tamm state on Cu(100) measured at 10 K with s-palarized HeI-photons (dots). The fit to the data (see text) gives a lorentzian peak of FWHM 7 meV (line).*

Due to the special symmetry of the $\overline{M}$-point, electron states in adjacent layers are expected to decouple, excluding in particular any interaction of the Tamm state with the bulk [159]. The Tamm state is thereby perfectly localized within the topmost surface layer. As further consequence of the symmetry, the photohole, created in this band, possesses a rather long

lifetime and is observed as extremely sharp lorentzian peak in the PE spectra. Linewidths between 23 meV [158] and 50 meV [160] have been reported in earlier studies. In a recent study a value of 13 meV has been deduced by extrapolating to 0 K and taking into account the energy resolution of the spectrometer [136]. Figure 5.8 presents our measurement of this state obtained at 10 K from a freshly prepared surface and with an angular resolution of $\pm 0.5°$. The peak has been fitted to a lorentzian function convoluted with a gaussian of 5 meV FWHM, representing the analyser contribution. The FWHM of the lorentzian extracted from this fit (Fig. 5.8) is 7 meV, corresponding to a hole lifetime of 100 fs [27].
Kevan *et al.*suggested that the Tamm state penetrates far into the bulk in order to explain an apparent discrepancy between the calculated and experimentally found binding energy [122]. Spin-orbit coupling could weaken the symmetry at $\overline{\mathrm{M}}$ and render this process possible (see also the discussion in Ref. [128]). More recent fully relativistic calculations, however, obtained very good agreement with the measured dispersion [161]. The authors state that the surface state is localized solely in the topmost surface layer. In the PE spectra, computed in the same work using a non-relativistic code, the surface state is well reproduced, emphasizing the insignificance of spin-orbit coupling[a]. Moreover, the extremely narrow line shown in Fig. 5.8 corroborates the lack of hybridization. It is interesting to note that the existence of a quasi-particle with a lifetime corresponding to about 100 fs and an energy of $E - E_F \approx -1.8\,\mathrm{eV}$ is merely explicable by Auger decay or thermalization by phonons.

5.6 Dispersion Parallel and Perpendicular to the Step Edges: Cu(610)

All spectra presented here were taken with the reflection plane (001) corresponding to the principal measurement plane (Θ-direction). Parallel to the step direction, the dispersion was mapped using the second detector dimension (φ-direction). Sample temperature was 300 K, unless otherwise stated. The work function was found to be 4.69 eV, somewhat higher than that of the flat surface, in agreement with results of Wang *et al.* [137].
Figure 5.9a shows a series of spectra recorded from Cu(610) at different emission angles in the downhill-direction. Approximate identification of the majority of the peaks can be made with reference to the well documented photoemission features of Cu(100) (see preceding section): B_1 is part of the Cu bulk band structure; peaks S_1 and S_2 are both surface features, the first being closely related to the Cu(100) $\overline{\mathrm{M}}$ Tamm state, and the latter corresponding to a Shockley state which exists in a spin-orbit induced band gap on Cu(100) [158]. An analogous state on Cu(100) can not be found for the peak S_S, and this will be addressed further below.

[a]The second surface state S_2 is only reproduced including relativistic effects due to its position within a spin-orbit gap.

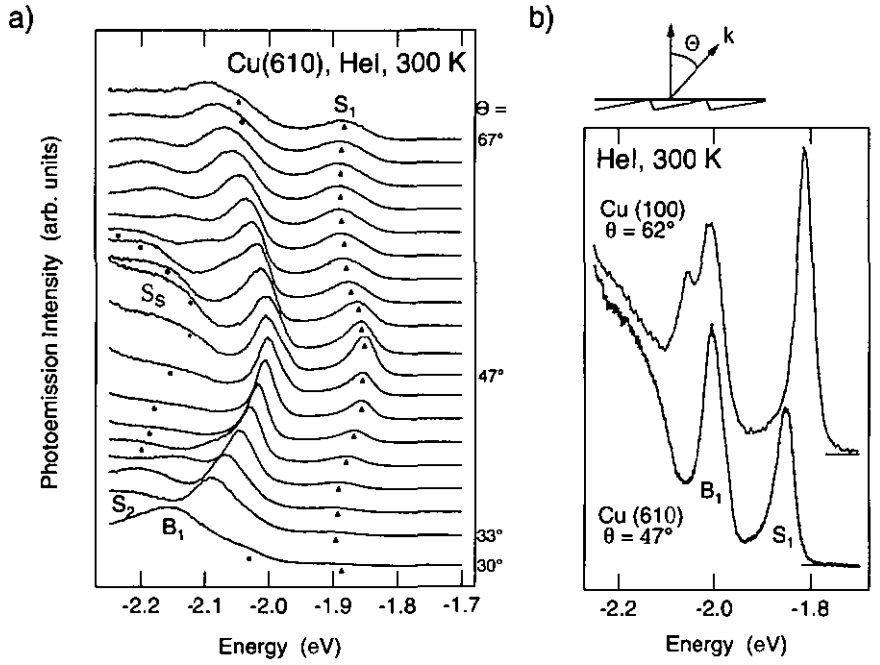

Figure 5.9: *a) A selection of HeI ARUPS spectra taken in the downhill direction in the mirror plane of Cu(610). The emission angle is given with respect to the normal of the macroscopic surface (see inset in the upper right corner of the figure). The peak designations are referred to in the text. Apart from the bottom two spectra, the angular difference between spectra is 2°. b) HeI ARUPS data from Cu(610) and Cu(100) at the angle of electron emission where the surface state is at its closest approach to the Fermi level.*

The presence of a regular step structure is seen to affect S_1[b]. Figure 5.9b shows ARUPS spectra from Cu(100) and Cu(610), measured at the emission angle where the Tamm state has its lowest binding energy. This comparison highlights two important points. The first of these is that the peak position is clearly shifted by 40 meV to higher binding energy on the vicinal surface. The second point concerns the angle at which S_1 has its lowest binding energy position on Cu(610), 47° in the downhill direction. The difference between this angle and that at which the Tamm state is measured at $\overline{\mathrm{M}}$ on Cu(100) (62° for HeI) does not correspond to the miscut of the vicinal surface. The microscopic picture of Cu(610) simply

[b]Although the Shockley state S_2 is also affected by the step structure, because of its presence inside the bulk *d*-bands its dispersion can only be followed over quite a limited range.

being composed of (100) terraces is not adequate, therefore, and the whole macroscopic surface must be considered in its unity.

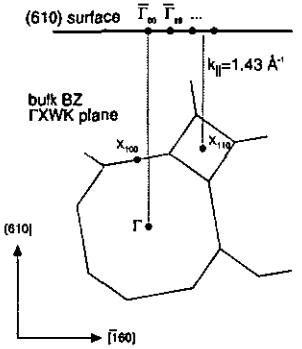

Figure 5.10: *The surface Brillouin zone of Cu(610) and its relation to the ΓXWK mirror-plane of the bulk Brillouin zone of copper in the extended zone scheme. The projection of the bulk X_{110}-point onto (610) corresponds to $k_{\|}$=1.43 Å^{-1}.*

On Cu(100), the Tamm state is associated with a gap in the Cu bulk band structure existing at the symmetry point X_{110}. As illustrated in Fig. 5.10, the projection of the appropriate X_{110}-point onto Cu(610) lies at $k_{\|}$=1.43 Å^{-1}, corresponding to an emission angle $\Theta = 47°$ for HeI-photons. In the uphill-direction, the projection of $X_{1\bar{1}0}$ onto the (610) surface is $k_{\|}$=-2.02 Å^{-1}, thus not accessible for HeI-excitation. Using HeII-photons, the minimum in binding energy is indeed found at -2.08 Å^{-1} (Θ=-44°).

Further evidence of the effect of the step super-structure on the surface state is obtained by plotting out the dispersion curve, $E(k_{\|})$, for S_1. This is done in Fig. 5.11a. In this figure the values of $k_{\|}$ are calculated with respect to the macroscopic (610) surface, an imposition required by the observation that Cu(610) cannot simply be considered as a combination of Cu(100) surfaces. The data points presented were obtained from the HeI photoemission spectra of Fig. 5.9(a), although the corresponding data points from HeII photoemission spectra (not shown) fall on the same dispersion curve, providing further confirmation of the surface nature of S_1. The most immediately striking aspect of the S_1 dispersion curve is the reduction in the band width compared to that of the analogous Cu(100) Tamm state. The band width of S_1 is ~50 meV, as compared to ~200 meV for the state on Cu(100) over the same k range [158]. This we take to be a signature of gap opening at the step superstructure zone boundary, something which is supported by the period of the dispersion curve. The separation of the two curve minima is 0.58 Å^{-1}, which corresponds to the reciprocal lattice

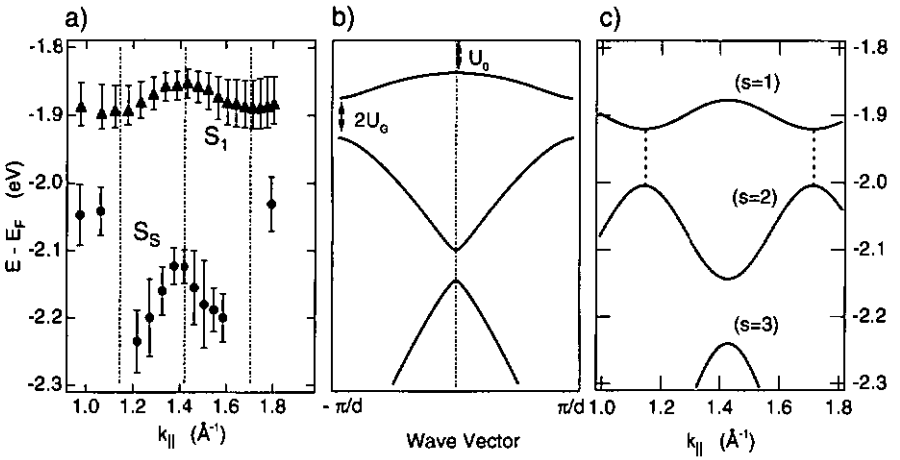

Figure 5.11: *Dispersion perpendicular to the step edges. a) Experimental results $E(k_{\|})$ for the state S_1 on Cu(610) [triangles]. The dispersion of the state S_S is also shown (circles). Dashed-dotted vertical lines denote the center and the border of the SBZ. b) Schematic band structure showing the effect of a one dimensional potential on a free electron of negative effective mass. The energy gaps at the zone border are given by the Fourier components of the step potential U_G. c) Result of the tight-binding calculation for Cu(610); parameters are taken from Ref. [162]. The gap between the bands (s=1) and (s=2) is denoted by vertical dashed lines.*

vector of the step superstructure. Observation of the step periodicity in S_1 indicates that electronic states are interacting across the step edge. Put another way, the confinement of state S_1 between the steps is not complete, in accord with previous calculations [152] and experimental results [137, 150, 151]. Around the point of minimum binding energy, the dispersion can be fitted with a parabola, yielding an effective mass of about -4.2 m_0.

We note that the effect of the periodic step potential provides an explanation for the state S_S [Fig. 5.9a]. Figure 5.11b shows schematically the dispersion of an electron band with negative effective mass. The introduction of new zone boundaries, such as those created by a regular step structure, causes gaps to open as illustrated and, in a reduced scheme, the appearance of back folded bands. A comparison of the $E(k_{\|})$ relation for S_S given in Fig. 5.11b with the schematic band diagram suggests that the peak may originate in the surface band back folded by the reciprocal lattice vector of the step super-structure[c]. The middle band of the three shown would be obscured by the bulk band structure. Recently, the dispersion of the

[c]This band structure was produced using the Kronig-Penny model, as given by Singh [149], with an arbitrary potential strength. Output of this model are usually transmission coefficients and phase shift of the wave function across the barrier [1, 97].

Tamm state on vicinal surfaces has been computed within the tight-binding scheme [162]. The hopping integrals for hopping between terrace sites and across a step were estimated from two-center integrals [103]. Results of this calculation are displayed in Fig. 5.11c for Cu(610). The dispersion of the S_1-state is clearly reproduced (s=1), but the energy shifts due to confinement are overestimated, when compared to experimental data [26,129], as well as the gap at the zone boundary between the (s=1) and (s=2) bands. The band labeled (s=2) should correspond to the state S_S in our nomenclature. According to Beckmann *et al.*, this overestimation results from the neglected change of the atomic potential at the steps owing to reduced coordination and charge neutrality [162].

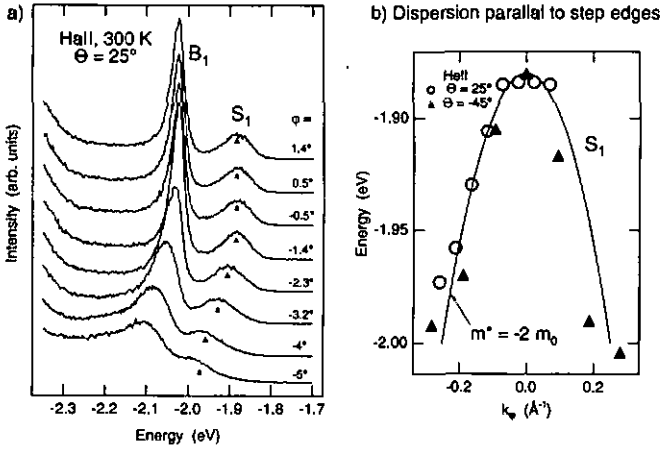

Figure 5.12: *Surface state dispersion parallel to the step edges. a) Spectra, taken with HeII-photons perpendicular to the mirror plane (angles φ are given). Symbols indicate the position of the peak maxima. The emission angle within the mirror plane was $\Theta = 25°$, thus close to the point of minimum binding energy. b) Dispersion of the peak maxima in the spectra, shown in (a), vs wave vector $k_{\parallel}^{par}$ along the steps. Data points are added, extracted from HeII-spectra around the point of minimum binding energy in the uphill-direction, Θ=-45°. The line denotes the parabola resulting from the fit (see text).*

Finally, we can make use of the second detector dimension in order to map the dispersion of the Tamm state parallel to the step edges. Since the range in emission angle, which can be covered in this mode, is limited, the spectra are taken with HeII-photons, accepting a worse resolution in angle. A selection of spectra, taken at $\Theta = 25°$ for various emission angles φ perpendicular to the symmetry plane (001), are shown in Fig. 5.12a. The peak dispersion, marked by symbols in Fig. 5.12a and plotted in part (b) as function of the wave vector $k_{\parallel}^{par}$, exceeds 130 meV, even in this small range in $k_{\parallel}^{par}$. The band width is, therefore, much

larger parallel to the steps than perpendicular, giving evidence for an unperturbed motion on the terraces parallel to the step edges. Using a parabolic function to fit the dispersion in Fig. 5.12b, an effective mass of $m^* \approx -2\,m_0$ is found as for the flat (100)-surface. The same behaviour can be seen in HeI-measurements along [001], i.e. parallel to the step edges, after re-orientation of the sample. The band bottom is shifted to higher binding energy, and the effective mass of S_1 found for Cu(610) is again -2 m_0. Surprisingly, the second surface state S_2 could not be observed in the HeII-excited spectra. The reasons for this are still not clear.

5.7 Lineshape Analysis and Comparison to Cu(811)

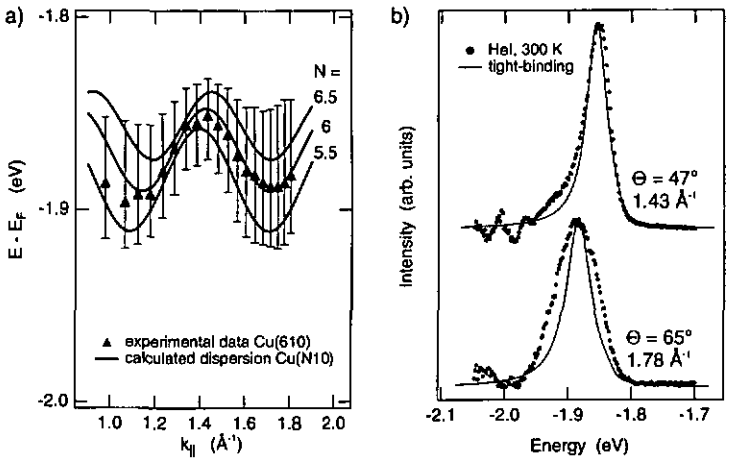

Figure 5.13: *Peak broadening due to electron confinement on Cu(610). a) Experimental peak dispersion (triangles) of the S_1-state; error bars indicate the energy at half maximum intensity of the asymmetric peak shape. Calculated peak dispersions [162] (shifted by +30 meV) are added as lines for surfaces (610), (5.5 1 0), and (6.5 1 0), corresponding to the finite terrace width distribution. b) Calculated line shapes (lines) using the measured terrace width distribution, together with experimental data (dots) for $k_{||}$ corresponding to band extrema (see text). The spectra have been corrected for background intensity.*

Using again the tight-binding calculation of Beckmann *et al.*, the line shape of the surface state can be computed [162]. In this model, the shift in energy of the surface state results from the smaller hopping probability across the steps. A small terrace size, and consequently a high step density, results in large energy shift. Broadening therefore arises from overlap of contributions from terraces of different size. This is sketched in part (a) of Fig. 5.13:

the measured peak dispersion is plotted together with the calculated dispersion on terraces, which are 5.5, 6, and 6.5 atom rows wide. For the sake of convenience, the theoretical curves have been shifted by 30 meV towards E_F. The peaks at the band extrema have a pronounced asymmetry with the larger tail towards the center of the band, visualized by error bars, which indicate the energy at half maximum intensity (Fig. 5.13a). Continuing with the analysis within tight-binding, Beckmann *et al.* obtain an expression for the peak shape, given as imaginary part of a function $g(\omega)$, which is defined by the following integral [162]:

$$g(\omega) \propto \int_{-\infty}^{\infty} dL\, \mathcal{P}(L) \frac{1}{\omega - E_N(L) + i(\gamma/2)}. \qquad (5.7.1)$$

Here, γ denotes the natural line width of the surface state, as measured on the flat surface, $\mathcal{P}(L)$ gives the terrace width distribution, and $E_N(L)$ describes the shift in energy of the surface state due to confinement on a terrace of width L. We note that the life time is still given by γ, i.e. the broadening of the peak shape is due solely to non-lifetime effects in this model. Using $E_N(L)$ from Ref. [162], γ=16 meV (at 300 K), and $\mathcal{P}(L)$ from the LEED-analysis described above, we can compute the peak shape without further fitting. The results are superimposed to experimental data in Fig. 5.13b for $k_\parallel$ corresponding to two band extrema, i.e. Θ=47°and 65°. The experimental spectra have been corrected for background, and the calculated spectra have again be shifted by 30 meV. The agreement is, at least qualitatively, satisfactory for both spectra. Even better agreement was obtained by use of the Kronig-Penney model as done in the previous analysis, Ref. [26]. The confinement shift was used there as fitting parameter. However, the values obtained for $E_N(L)$ were too high to be justified by confinement of the surface state between monatomic steps (see discussion in Ref. [162]).

At the end of this section, the spectrum taken from Cu(811) at the point of minimum binding energy will be analysed. The emission angles, corresponding to the projection of X_{110} onto the (811)-surface, are $\Theta \approx 50°$ and $\varphi \approx 8°$. To reach this point with our experimental setup, the use of a wedge underneath the sample was necessary. It has been checked that the projection of X_{110} coincides with the point, where the surface state has minimum binding energy. The spectrum is shown in Fig. 5.14, superimposed to the equivalent spectrum taken from Cu(610) ($\Theta = 47°$). This comparison highlights two important points. The shift in energy with respect to the flat surface is larger for Cu(811) than for Cu(610). This might be expected since the step edges correspond to a close-packed direction of the fcc-lattice. The confinement is therefore more complete than on the (610)-surface. The second point of note is the line width, found to be 55 meV for Cu(811), which has to be compared to 40 meV on Cu(610). Following the analysis within the confinement model, this is reasonable, because a larger confinement shift results in larger broadening, if the terrace width distributions are comparable [162]. Unfortunately, the latter could not be measured for Cu(811), because the

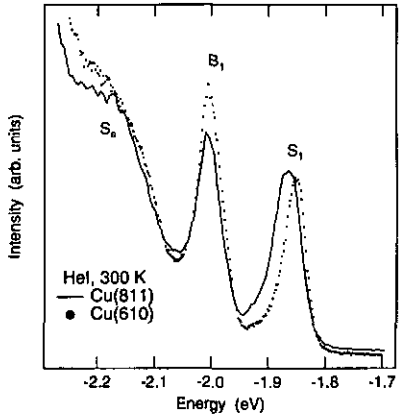

Figure 5.14: *Photoemission spectra, taken from Cu(610) [dots] and Cu(811) [line] at the respective X_{110}-points. The spectra have been normalized to the same maximum intensity for S_1.*

CCD-camera system was not at hand when the measurements were carried out.

5.8 Summary: Superlattice Effects

The following picture emerges from our results. The surface state observed on Cu(610) is analogous to the $\overline{\mathrm{M}}$ Tamm state of Cu(100). Its energy position is determined by the degree of confinement on the terraces. This localization is not complete and the spatial extent of the state is greater than the average terrace width. The surface state is related to a particular X symmetry point of the bulk reciprocal lattice, and its momentum is determined by the surface projection of this point. This statement is valid for all surfaces investigated here, i.e. Cu(610), Cu(811), and Cu(100). The dispersion of the surface state reflects the step-induced superlattice. The surface state wave function can be pictured as superposition of propagating waves, which are partially reflected at and transmitted through the potential barriers at the step edges. The back folded bands fall into the projected bulk band DOS, reflecting a hybridization of the surface state with bulk states.

A tight-binding scheme was shown to provide the basic physics of stepped surfaces, but self-consistency and inclusion of the charge rearrangement at the step sites in the calculation are required in order to improve agreement with experimental data. Finally, the asymmetric broadening of the surface state peak shape arises solely from confinement shift due to the non-uniform terrace width distribution, and is therefore a non-lifetime effect.

Chapter 6

Electron-Phonon Coupling: Be(0001)

Up to now, we have seen how superstructure lattices influence the line shape, dispersion, and lifetime of electronic excitations. In this chapter, we will go one step further including many-body effects. As example serves the well-known $\overline{\Gamma}$-surface state on Be(0001). After a short survey of the bulk and surface properties of Be, and of the experimental procedure, the photoemission results will be shown and compared to many-body calculations. Large parts of this chapter have been published in Refs. [28, 29].

6.1 Beryllium Bulk Properties

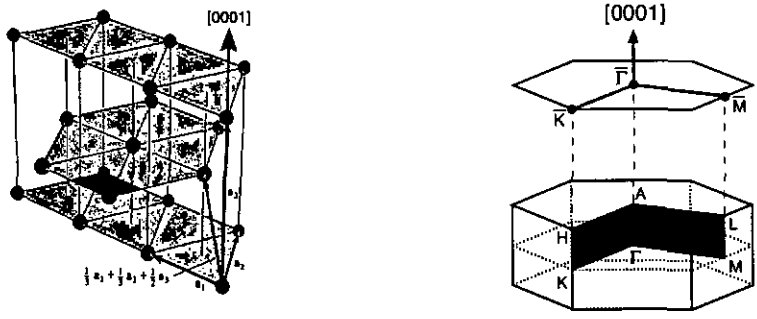

Figure 6.1: *Left panel: hcp-lattice with 2 atoms per unit cell. Right panel: BZ of the hcp-lattice; the main symmetry points are indicated. Above the BZ, the SBZ of the (0001)-face is shown, together with the projection of the symmetry planes.* $\overline{\Gamma K}$ *corresponds in real space to the nearest-neighbour direction within a (0001)-plane. The distance* $\overline{\Gamma K}$ *of the SBZ is about* $1.8\ \AA^{-1}$.

Beryllium (No. 4 of the Periodic Table of Elements) is an alkaline earth metal, iso-electronic

to Mg, which is considered as "simple metal" [1]. It crystallizes in the hexagonal close packed (hcp) structure with 2 atoms per unit cell (left panel in Fig. 6.1). The lattice constants are $a = 2.28$ Å and $c = 3.582$ Å [163], thus a c/a ratio of 1.57, somewhat smaller than the value of 1.63 for an ideal hcp-lattice [164]. The corresponding Brillouin zone (BZ) is shown together with the BZ of the (0001)-surface in the right panel of Fig. 6.1. The main symmetry directions of the (0001)-SBZ are indicated.

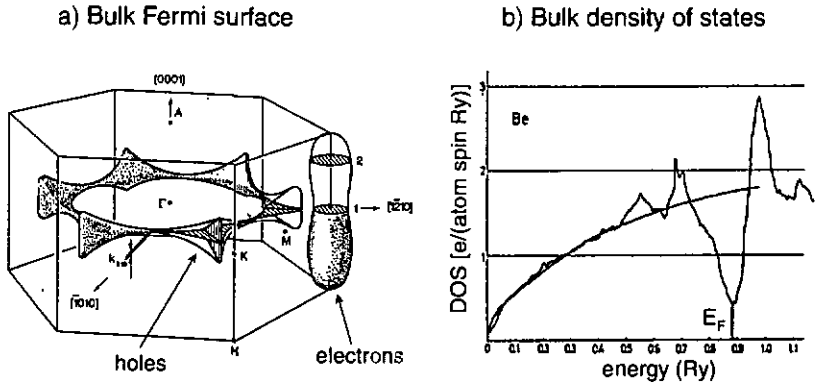

Figure 6.2: *Electronic properties of bulk Be. a) Fermi surfaces: ring-like corona of the holes and one quasi-ellipsoid at each corner for the electrons (from Ref. [165]). b) Density of states in comparison to the free-electron model (square-root function). Note that E_F lies in a dip of the DOS; the corresponding DOS value (indicated by a vertical grey line) is lower by a factor of 4 than that of the free-electron model (from Ref. [163]).*

Since the atomic electron configuration is a closed s-shell $1s^2 2s^2$, the metallic behaviour is dominated by the fraction of $2s$-electrons promoted into $2p$-states [164]. This leads to strong deviations from the free-electron model, reflected in a complicated Fermi surface topology and in a very low density of states at E_F [163, 166], plotted in Fig. 6.2. Due to the low number of states participating in the low-energy properties Be is a very poor conductor. It is beyond the scope of this work to enumerate all the unique properties of Be, which can be found e.g. in Refs. [163, 164, 166], but we note *en passant* the unusually high Debye temperature of bulk Be (about 1400 K) and the weak electron-phonon coupling constant $\lambda = 0.23$[a], estimated from the superconducting transition temperature [163]. Photoemission experiments from Be bulk bands show good agreement with band structure calculations, only if the electron-plasmon interaction is accounted for [167, 168].

[a]This coupling parameter λ will be defined later.

6.2 The "Specimen": Exotic Behaviour at E_F

Be is an almost paradigmatic example of a solid whose surfaces "live their own lives". The widely studied $(10\bar{1}0)$-surface, for instance, exhibits strong relaxation of the surface atoms [169], and the electronic response is dominated by a surface state at the border of the SBZ [153, 170–172]. The (0001)-surface of Be does not reconstruct, but drastic modification of the properties with respect to the bulk can be anticipated from the reduction in coordination at the surface. Low-energy-electron diffraction (LEED) measurements reveal large deviations of the inter-planar spacing at the surface compared to the bulk. Large values for the mean square displacement and thermal expansion are also unveiled [173], and all of these physical parameters are well described by density-functional theory [174]. The surface phonon modes investigated by electron-energy-loss-spectroscopy (EELS) could only be reproduced by calculations which assume substantial variations of the nearest neighbour force constants, inducing in the surface layer a reduction of the inter-planar bonding and an increase of the in-plane bonding [164,175]. A detailed calculation of the electronic structure of Be(0001) [176] predicts the existence of surface states in large gaps of the projected bulk density of states (DOS), in good agreement with angle-resolved photoemission data [177,178]. The charge density originating from the surface states is essentially localized within the first two layers [176,179] (Fig. 6.3) and dominates the DOS at E_F by a factor of four over the bulk density. As a consequence of the valence charge redistribution at the surface, the binding energy of the $1s$ core level, which probes the local charge density [179], is shifted with respect to its bulk value. Four distinct components resolved by x-ray photoemission spectroscopy could be related to emission from layers at different depths below the surface [180–182]. Finally, the electron inelastic mean free path of 2 Å at low kinetic energies (10-40 eV) is anomalously small compared to about 10 Å of the universal curve due to a high electron-hole pair and/or surface plasmon creation rate [183].

The $\overline{\Gamma}$-surface state of Be(0001) is widely decoupled from the bulk states and forms a nearly-ideal 2-dimensional (2D) electron gas on a poorly conducting substrate. The almost isotropic parabolic dispersion of the state is fitted with an effective mass which varies between 1.17 [164] and 1.53 [178] times the electron rest mass. The Fermi circle of the surface state has a radius of 0.93Å^{-1}, corresponding to roughly half the distance $\overline{\Gamma M}$ of the surface Brillouin zone (SBZ). In a recent scanning tunneling microscopy (STM) study, the surface image obtained for small bias potential showed a complex pattern of electron density waves resulting from scattering at impurities and defects [184]. These so-called energy-resolved Friedel oscillations are now well understood and can be used to map out the dispersion of the surface states involved [141,142,185,186]. As an example, the pattern obtained for small bias voltage (i.e. collecting electrons from E_F) is shown in Fig. 6.4 together with its Fourier transform into reciprocal space. The Fourier transform maps perfectly the FS of the surface state, if one takes into account that this method always measures twice the wave vector of the

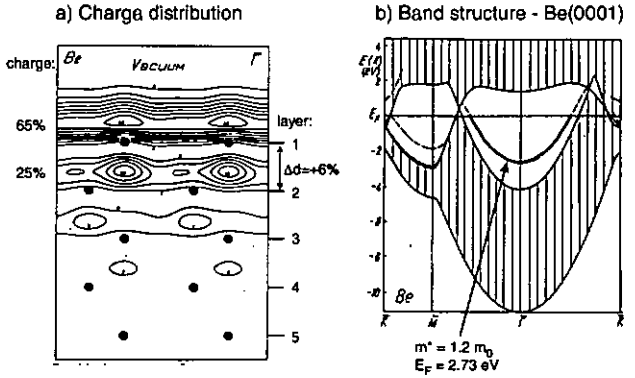

Figure 6.3: *Properties of the $\overline{\Gamma}$-surface state on Be(0001). a) Charge distribution of the surface state, projected into the $(11\bar{2}0)$-plane of the crystal. The vertical axis corresponds to the [0001]-direction; note the inter-planar spacing between the two topmost layers 1 and 2, larger by 6% than the bulk value. b) Bulk band structure projected onto the (0001)-surface (hatched area); the thick solid line denotes the $\overline{\Gamma}$-surface state, dashed lines other surface resonances (both figures from Ref. [176]).*

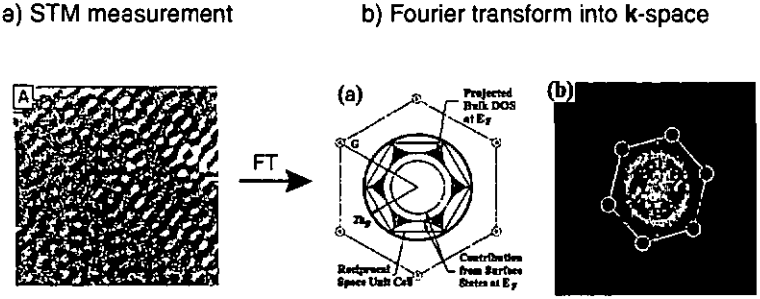

Figure 6.4: *Energy-resolved Friedel oscillations on Be(0001), as measured by means of STM. a) STM pattern in real space, recorded at 150 K; only electrons from the Fermi level are collected (from Ref. [184]). b) Fourier transform of such a pattern into reciprocal space; sketch of the SBZ with the FS of bulk and surface states on the left, and the transformed pattern on the right. The measured circle is identical to the FS of the $\overline{\Gamma}$-surface state (thick line) [taken from Ref. [186]].*

electrons involved [186]. This means that the surface state clearly dominates the electronic response. However, the Be study exhibits two exceptional features: the amplitude of the electron density waves near E_F is huge when compared to observations made on other surfaces [141, 142], and this amplitude decreases dramatically by orders of magnitude for larger

bias voltage. The authors propose an enhancement of the DOS at E_F due to electron-phonon coupling, or else, an accumulation of states due to the opening of a gap, to be responsible for the strong amplitude at E_F. The latter requires the pinning of the Fermi energy at the lower edge of the gap [184]. The formation of a charge density wave (CDW) was suggested as driving force for the gap opening. Such a CDW phase transition should occur at higher temperature than 150 K, where the STM-measurements were carried out.

Very recently, an electron-phonon coupling parameter of $\lambda = 1.15$ was extracted from a photoemission study of the temperature dependence of the surface state linewidth [187], thus five times the bulk value[b]. The authors claim this to be a possible indication for the existence of surface superconductivity with a high critical temperature. Summarizing, both, STM and photoemission experiments, suggest the occurrence of a quite unconventional mechanism modifying dramatically the nearly free electron behaviour of the surface state near E_F.

Before entering the description of our experiment, it is worth to see what is to be expected in the case of a CDW-formation or a metal-superconductor transition. A CDW introduces a new reciprocal lattice vector at $2\mathbf{k_F}$, which causes the opening of a gap at E_F. The electronic energy gain due to the gap stabilizes the phase transition [11]. In photoemission spectra, the gap can be observed as a depletion of spectral weight at E_F in line with an accumulation of weight at the low-energy edge of the gap. Such gaps, or pseudo-gaps for only partial depletion [189], were already observed with photoemission [17, 190, 191] and inverse photoemission [192]. Spectra of sodium [193], were claimed to be signature of such behaviour [194], but these results are subject to very controversial discussion [195–197]. We note that the gap could be anisotropic, but this should be rather improbable in the case of the isotropic $\overline{\Gamma}$-surface state on Be(0001). As second evidence for a CDW transition, the LEED pattern may exhibit additional spots due to the new reciprocal lattice vectors induced by the CDW. The case of superconductivity is much clearer. An example of a line shape observed with photoemission at and below the transition temperature is given in Fig. 6.5. The depletion of spectral weight at E_F in the superconducting phase is signature of the gap. Based on an electron-phonon coupling strength of $\lambda = 1.15$, Balasubramanian and co-workers estimated the critical temperature to be 70 K for the Be-surface [187]. The real value should be smaller than stated, since the appropriate formulae for the strong-coupling limit have to be taken [202]. However, according to the BCS-theory of conventional superconductivity, this would correspond to a gap of $\Delta = 1.76\, k_B T_c \approx 11$ meV at $T = 0$ or of $\Delta(12\text{ K}) \approx 10$ meV [1] for the temperature which can be reached with our equipment. Since the excitation of a photoelectron corresponds to the breaking of a Cooper-pair, we should observe a gap of the order of 10 meV and the concomitant QP peak in the spectra.

[b]The value has been meanwhile corrected for an error in the original analysis. It yields $\lambda = 0.8$ [188].

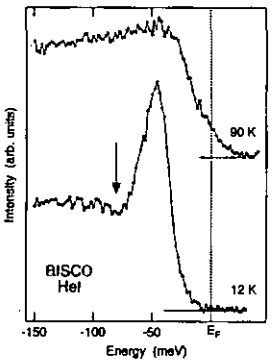

Figure 6.5: *Photoemission spectra, taken from the high-temperature superconductor BISCO ($T_c \approx 90$ K) at (top spectrum) and below the transition temperature (bottom spectrum). The well-known line shape in the superconducting state (e.g. [198–201]) exhibits a famous "dip" at the low-energy tail of the strong QP-peak (arrow) and no spectral weight at E_F, indicative of the gap (K. Breuer, U Neuchâtel, unpublished results).*

6.3 Sample Preparation

The sample was mechanically polished (diamond grain size 0.25 μ) and cleaned *in situ* by cycles of Ar^+ sputtering (1.5 keV) and annealing. Sputtering at elevated temperature (850 K) was found to be particularly efficient to remove oxygen, whereas carbon could be removed by sputtering at room temperature. The annealing temperature was slightly lower (800 K) and the subsequent cooling to room temperature has been done very slowly (over 30 mins). Typically, one sputtering cycle was necessary each day because of contamination by oxygen. After the treatment, contamination lines (carbon and oxygen) were barely discernible in Auger spectra recorded with highest sensitivity, yielding a contamination level of less than 0.3% with respect to the Be Auger lines. As expected, a sharp hexagonal LEED pattern was observed.

For the PE experiment, the sample was oriented with the measurement plane corresponding to emission from wave vectors either along the $\overline{\Gamma M}$-line or along the $\overline{\Gamma K}$-line of the SBZ. The angular resolution turned out to be the crucial experimental factor. For the variable polar angle, where the dispersion is fast, we estimate the resolution to be 0.2°. For electrons emitted from E_F by HeI-photons this corresponds to $\Delta k_{||} \approx 0.009\text{Å}^{-1}$ ($\approx 0.014\text{Å}^{-1}$ for HeII-photons). In the perpendicular direction, tangential to the constant energy curves of the surface state, the resolution is less important and was fixed electronically to 0.5-1° ($\Delta k_{||} \leq 0.036\text{Å}^{-1}$ for HeI or 0.055 Å^{-1} for HeII).

The peak of the surface state at $\overline{\Gamma}$ was measured with a linewidth of about 340 meV, indicating an excellent surface quality, if compared to data available in literature [178, 187].

The wave function symmetry is even under reflection at the mirror plane [177]. In the following, all spectra presented are therefore taken using p-polarized light, unless otherwise stated.

Using the capillary lamp as light source, the sample surface was found to be stable for at least 15 mins under constant vuv-illumination at low temperature. As already discussed, this time limitation is due to radiation induced surface damage [27,203], and the surface order can be restored by one annealing cycle (about 1 hr including warmup and cooling). Using the monochromatised source, the time scale was considerably longer, allowing reproducible spectra to be taken during 3-4 hrs.

6.4 Experimental Results

In Fig. 6.6, a set of spectra is shown, covering the whole band dispersion of the $\overline{\Gamma}$-surface state along $\overline{\Gamma M}$. The spectra were recorded with HeI-photons from the unmonochromatised source and the sample held at 60 K. An analysis yields the following band parameters for $\overline{\Gamma M}$ ($\overline{\Gamma K}$, spectra not shown): a parabolic dispersion with an effective mass of 1.19 (1.14) times the electron rest mass, and a Fermi wavevector of 0.924Å^{-1} (0.90Å^{-1}). The occupied bandwidth was found to be 2.73 eV, in good agreement with published data [177,178].

Within our experimental accuracy, the general trend of the measured dispersion curve $E(k_{||})$ of the surface state is unaffected by the sample temperature in the range 12 - 300 K. This allows a direct comparison of equivalent spectra recorded at different temperatures. One remarkable trend can be pointed out in this set of spectra: upon increasing the emission angle from normal emission towards k_F, the maximum intensity of the peak diminishes and the linewidth becomes larger. This is essentially due to the increasing slope of the dispersion curve in line with the minor angular resolution employed [37]. Close to $\mathbf{k_F}$, however, we observe a steep increase in intensity instead of a continuous decrease, suggesting an enhancement of the DOS at E_F, reminiscent of the results of the STM measurements mentioned above [184]. We will focus our attention now to the energy region near E_F. Figure 6.7a shows a set of data in a narrow k range near the Fermi level crossing, taken with HeI-photons (left panel). The relative intensities are normalized to the measurement time, and spectra are labeled by emission angles with respect to the surface normal. From the bottom of the figure, the first two spectra, $\Theta = 23.7°$ and $24.7°$, have the expected form and evolution for a surface state moving toward E_F. This trend can still be recognized in the following two spectra, $\Theta = 25.2°$ and $25.7°$, but a new weak structure emerges around 60 meV. The relative intensity of this new feature becomes important in the next spectrum, $\Theta = 26.2°$, and finally dominates completely the spectral function at k_F ($\Theta = 26.7°$), obtained from the extrapolation of the full dispersion curve of the conventional surface state. This extrapolation is allowed since an isotropic Fermi surface is not altered by interactions [46]. For wave vectors

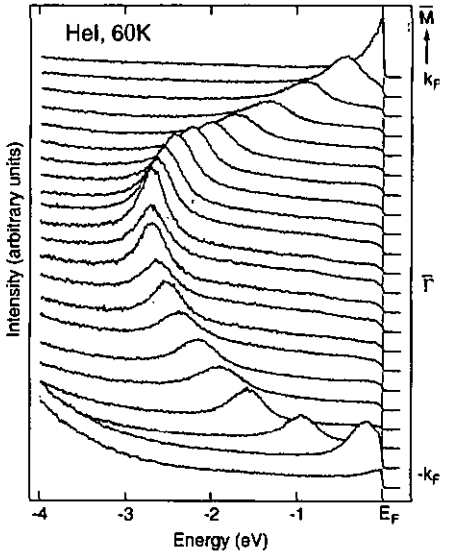

Figure 6.6: *Photoemission spectra of the $\bar{\Gamma}$-surface state on Be(0001) showing its parabolic dispersion along $\bar{\Gamma}\bar{M}$. The spectra were recorded with unpolarized HeI-photons at 60 K. 0° corresponds to normal emission, and the angular resolution is 1°. The difference in angle between two neighbouring spectra is 2.5°.*

larger than k_F ($\Theta > 26.7°$), the peak remains pinned at E_F with a rapidly decreasing intensity. The same lineshapes can be observed around $-k_F$ (spectra not shown) and in the corresponding spectra excited with HeII-radiation (Fig. 6.7b). The latter are broadened due to the worse resolution in k at higher electron energies.

In order to better characterize the narrow peak, we measured spectra with maximum resolution in energy and angle in the small energy range of 140 meV (Fig.6.8). These data clearly show the weak dispersion of the peak reaching E_F in the spectrum for $\Theta = 26.7°$. For $k > k_F$, the lineshape remains unchanged, whereas the amplitude decreases and an intensity excess above E_F is observed ($\Theta = 27.2°$). The true peak position in the spectra at $k > k_F$ cannot be observed due to the cut-off by the Fermi function, but it can nevertheless be anticipated that the excess in intensity above E_F and the shape of the peak indicate that the maximum lies above the Fermi energy. Furthermore, measurements at 300 K clearly confirm the thermal population of a high density of states for these values of k and one can safely conclude that the state crosses E_F (Fig. 6.9). This observation, together with the experimental position and sharpness of the Fermi edge, exclude the existence of a gap at E_F larger than 4 meV at 12 K. Since the spectral function remains basically unchanged at least up to 60 K (Fig. 6.10b),

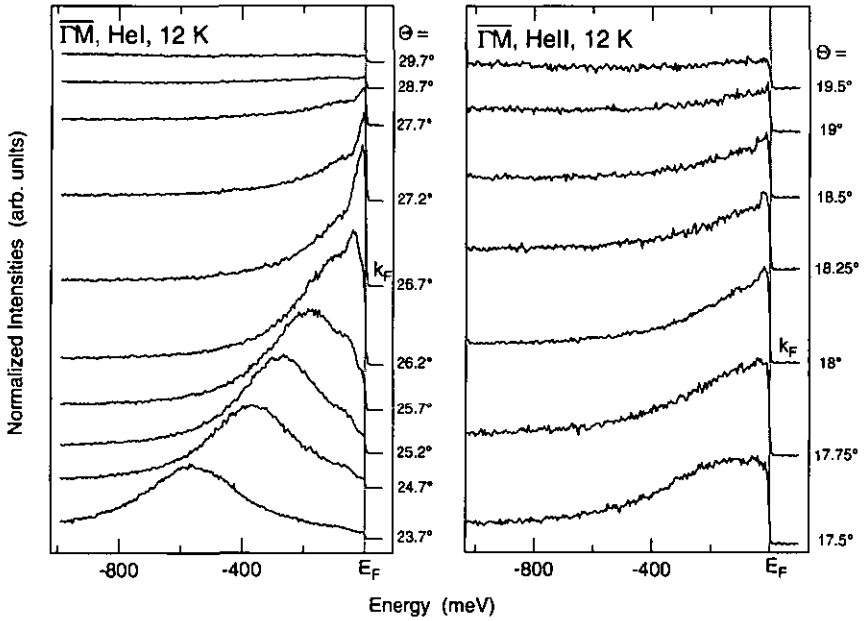

Figure 6.7: *Spectra taken at 12 K along $\overline{\Gamma M}$. Left panel: HeI, p-polarization. Right panel: HeII, unpolarized source. All spectra are normalized to the measurement time, the emission angles and $\mathbf{k}_F$ are indicated.*

where a 4 meV gap should be closed due to thermal excitation, the opening of even such a small gap becomes unlikely. The suggestion of surface superconductivity [187] can therefore be discarded, despite the resemblance of the spectra to photoemission measurements from high-temperature superconductors (Fig. 6.5 and Refs. [198–201]). For the same reason we can rule out an interpretation based on the formation of a charge density wave (CDW), since this requires the opening of a gap. Even if the lower band edge is pinned to E_F, this model is incompatible with our observation of the Fermi level crossing. A further indication of the inadequacy of this mechanism is the lack of extra diffraction spots in LEED-images observed at 60 K, as shown in Fig. 6.10b.

Moreover, the existence of an anisotropic gap can be ruled out, because the evolution of the spectra is the same for $\overline{\Gamma K}$ and for $\overline{\Gamma M}$ (Fig. 6.11): as the surface state approaches E_F (spectra at $\Theta = 24.4°$ through 25.9° in Fig.6.11), a second peak appears at -70 meV. Its intensity increases dramatically towards k_F, where it finally dominates the spectral function ($\Theta = 26.4°$). For $k > k_F$ ($\Theta = 26.65°$ to 27.4° in Fig.6.11), the whole spectral intensity decreases rapidly. However, the spectra show a sharp peak remaining pinned at E_F and a

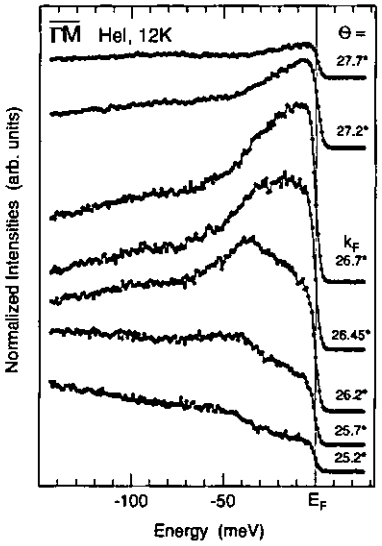

Figure 6.8: *As in Fig. 6.7, only for HeI-photons. Highest resolution in energy and angle was employed. Energy steps are 1 meV.*

second weak structure at about -70 meV.

The electron-phonon interaction is known to profoundly modify the electronic states near E_F in a characteristic energy region of the order of the phonon bandwidth ω_{ph} [129, 204]. The same mechanism has been invoked to explain an anomalous intensity observed in photoemission spectra from α-Ga(010) [205]. Recently, many-body effects have been found to renormalize the electronic energy of a surface state on Mo(110), but the electron-phonon coupling was weak and the QP picture was claimed to be appropriate on the whole energy scale [206]. For Be(0001), ω_{ph} can be estimated from EELS-measurements to about 60-70 meV [175]. This strongly suggests that ω_{ph} sets the correct energy scale for the unconventional lineshape evolution observed in our spectra. A many-body ground state results from the electron-phonon interaction and the excitations of this observed with photoemission correspond to the spectral function derived from the initial state by a perturbation treatment [6]. Several years ago, electron-phonon systems were treated within this formalism based on the coupling between an additional electron and phonon modes within the Debye-model [207]. These results have been extended to finite temperature and more realistic models, and their relevance in different measurements has been discussed [208,209]. By taking advantage of the symmetry between electron and hole addition, these spectral functions (e.g. Figs. 14-17 in

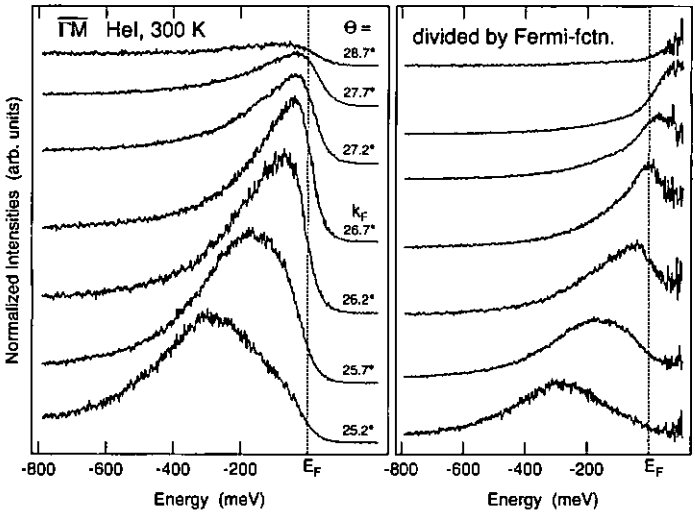

Figure 6.9: *Spectra taken around* $\mathbf{k_F}$ *along* $\overline{\Gamma M}$ *at 300 K (HeI, p-pol.). Right panel: raw data; curves are normalized to measurement time, and emission angles are given. Left panel: same spectra, but divided by the Fermi function at 300 K (see text) in order to emphasize the Fermi level crossing.*

Ref. [207]) can be compared to our spectra. The agreement between experiment and theory is at least qualitatively quite satisfactory: a sharp peak appears near E_F when the energy of the hole with respect to the Fermi energy becomes comparable to the phonon bandwidth. The quasi-particle picture of the electron-phonon coupling is only valid for energies either very near to or far away from the Fermi energy on the scale of the phonon bandwidth, but it breaks down for $E - E_F \approx \omega_{ph}$ [207–209]. Close to E_F, this quasi-particle can be more conventionally described as a hole excitation with a mass enhanced by a factor of $(1 + \lambda)$. In order to estimate the mass renormalization factor and, from this, the electron-phonon coupling parameter, it is necessary to compare the dispersion at E_F with that at energies far below. These can be linearized in the small region of interest. In Fig. 6.12a, the energy positions of the peak maxima for $\overline{\Gamma M}$ and $\overline{\Gamma K}$ are plotted together with the fitted dispersion. Additionally, points extracted from spectra taken at 300 K have been added to emphasize the crossing of the Fermi level. For $k \geq k_F$ these high temperature points were obtained by recording spectra with sufficient statistics in the tail above E_F to allow a subsequent division by the Fermi function (see Fig. 6.9). The thin solid line denotes the dispersion of the band $\varepsilon(\mathbf{k})$ in the energy range where only the electron-electron interaction plays a

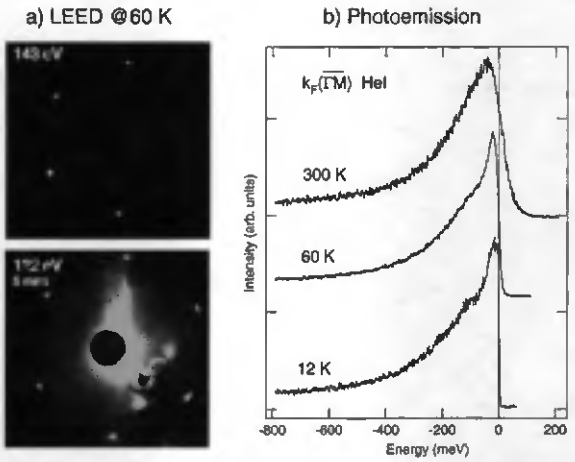

Figure 6.10: *Temperature dependence. a) LEED pattern recorded at 60 K and kinetic energies of 143 eV (top) and 122 eV (bottom); note the exposure time of 5 mins for the bottom image. No extra spots can be found in the low-temperature pattern, when compared to images taken at 300 K. b) PE spectra (HeI, p-pol.), taken from* $\mathbf{k_F}$ *(direction* $\overline{\Gamma M}$*) at different temperatures, as indicated.*

role and the quasi-particle description is adequate. Its dashed continuation toward k_F is the extrapolation used in the calculation. The thick solid line near k_F is the quasi-particle dispersion lowered by the electron-phonon coupling, $Z_{\mathbf{k}}\varepsilon(\mathbf{k})$. The size of the symbols scales with the relative intensities of the peaks. It is obvious that the experimental points follow the quasi-particle dispersion at E_F only in a small range below the Fermi energy, where the corresponding peak dominates the spectral function. This behaviour is strongly reminiscent of pictures found in solid state physics textbooks, as shown in Fig. 6.12b [1]. Lines were fitted to the band dispersion for energies $E - E_F > \omega_{ph}$ and to the renormalized dispersion close to E_F. The ratio of the slopes is $(1+\lambda)$. This yields $\lambda = 1.18 \pm 0.07$, in excellent agreement with the first value determined from the temperature dependence of the surface state linewidth [187]. Common values among the elements are mostly smaller than unity (for bulk Be $\lambda = 0.24$), except for some exceptional cases, large gap superconductors like Pb, where λ lies between 1 and 1.6 [202,210]. Our data thus demonstrate that the Be(0001)-surface has an individual behaviour distinct from the bulk, with a strong electron-phonon coupling at the surface. These conclusions will be strengthened by many-body calculations presented in the next section.

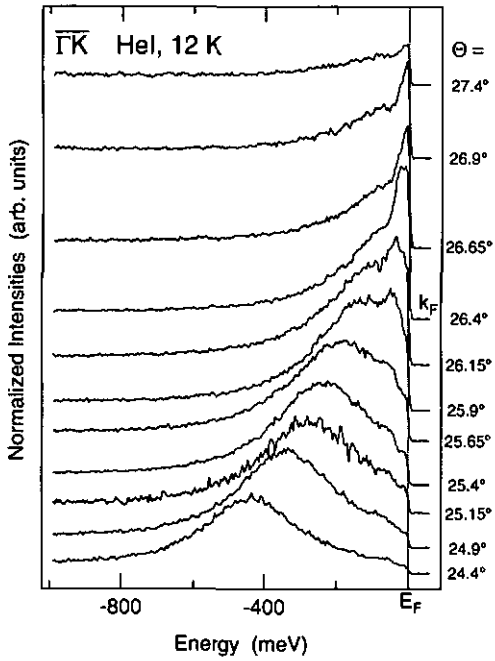

Figure 6.11: *Spectra taken at 12 K along $\overline{\Gamma K}$ close to $\mathbf{k}_F$ (HeI, p-pol.). Curves are normalized to measurement time; $\mathbf{k}_F$ and emission angles are indicated.*

6.5 Comparison of the Spectra with Calculations

A pictorial view of the electron-phonon coupling was already given in Chapter 2.3. It was then shown that the whole many-body physics is included in the self-energy of the interacting system. We can therefore skip this part here and go directly into *medias res*.

In an isotropic system, the electron-phonon part of the self-energy can be well approximated by averaging the electron-phonon coupling function over the Fermi surface [209]. The phonon modes then enter into the calculation through the so-called McMillan or Eliashberg function $\alpha^2F(\tilde{\omega})$, approximated here as a product of coupling strength and phonon DOS. The latter is taken to be linear in energy in two dimensions. The coupling strength is a smooth function of energy [208, 209, 211] and is taken here to be constant. The basic idea of our approach is, therefore, the linearization of the Eliashberg function submitted to the constraint that the maximum phonon energy equals the experimentally observed value ω_m [164, 175]. It is this value which sets the relevant energy scale of the interaction. The value of the coupling

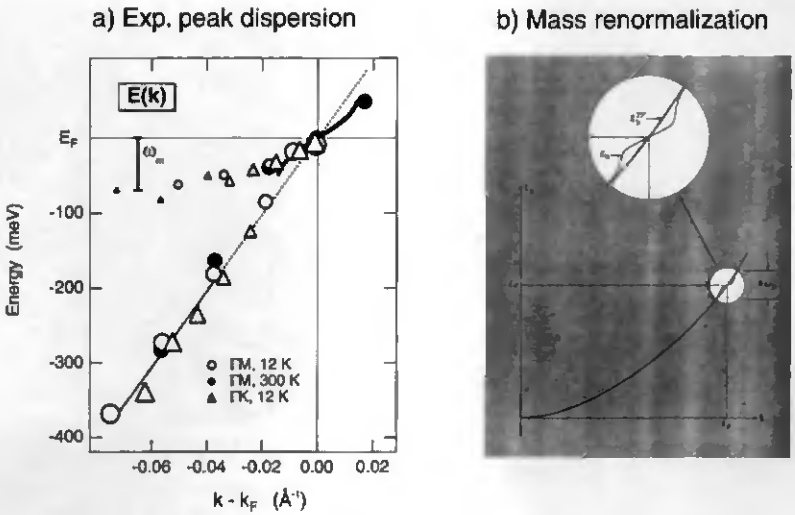

Figure 6.12: *Renormalization of the band energy. a) Dispersion of the experimentally determined peak maxima vs wave vector with respect to* $\mathbf{k_F}$*, for different directions (*$\overline{\Gamma M}$ *- circles,* $\overline{\Gamma K}$ *- triangles) and temperatures (12 K - open symbols, 300 K - solid symbols); the symbol size scales with the peak intensity. The band dispersion for energies higher than the maximum phonon bandwidth* ω_m *is shown by a thin line and extrapolated to* E_F *(dashed line). The many-body correction near* E_F *is plotted as thick solid line and may be compared to the picture in (b).* ω_m *is indicated. b) Sketch of the band renormalization near* E_F *due to electron-phonon coupling (from Ref. [1]).*

parameter λ, which is defined by the following integral [47]

$$\lambda = 2 \int_0^{\omega_m} \frac{\alpha^2 F(\tilde{\omega})}{\tilde{\omega}} \, d\tilde{\omega} \,, \tag{6.5.1}$$

then gives $\alpha^2 F(\tilde{\omega})$. The experimental value of λ is obtained from photoemission data either as the renormalization factor of the band dispersion at E_F as shown above or, equivalently, from the temperature dependence of the surface state linewidth near the Fermi surface [187,204]. A straightforward evaluation of Eq.(6.5.1) yields then $\alpha^2 F(\tilde{\omega}) = \lambda \tilde{\omega}/(2\omega_m)$.

Since the self-energy is only weakly k-dependent, $\Sigma^{ph}(k,\omega)$ can be replaced by its value at k_F (Migdal's theorem, [212]). One then arrives at the standard expression, dropping the

index k_F [209]:

$$\Sigma^{\rm ph}(\omega) = \int_{-E_F}^{\infty} d\epsilon \int_{0}^{\omega_m} d\tilde{\omega}\, \alpha^2 F(\tilde{\omega}) \times \left\{ \frac{1 - f(\epsilon,T) + N(\tilde{\omega},T)}{\omega - \epsilon - \tilde{\omega} + i\delta^{\pm}} + \frac{f(\epsilon,T) + N(\tilde{\omega},T)}{\omega - \epsilon + \tilde{\omega} + i\delta^{\pm}} \right\}, \qquad (6.5.2)$$

where $f(\epsilon,T)$ and $N(\tilde{\omega},T)$ are the Fermi-Dirac and Bose-Einstein factors, respectively. $\omega = 0$ refers to the Fermi energy, and $\delta^{\pm} \equiv sgn(\omega)\delta$ is an infinitesimal number. Assuming particle-hole symmetry, the limits of the ϵ-integration are set to $\pm E_F$.

In order to simulate the photoemission lineshapes, we adopt the procedure described in section 2.3 and the formulas given above with the following parameters: $\omega_m = 70$ meV was taken from electron-energy-loss measurements [164,175], and $\lambda = 1.18$ was determined by comparison of the quasi-particle dispersions in the present spectra (Fig. 6.12). The high Debye temperature of the sample (~1000 K) with respect to the sample temperature (12 K) allows us to compare the experimental spectra with calculations performed for $T = 0$. The Eliashberg coupling function and the phonon contribution to the self-energy are evaluated using Eqs. (6.5.1) and (6.5.2) (see Appendix B for the analytical form of the self-energy at $T = 0$). $\Sigma^{\rm ph}$ from Eq.(6.5.2) at $T = 0$ is displayed in Fig.6.13. Its behaviour is strongly

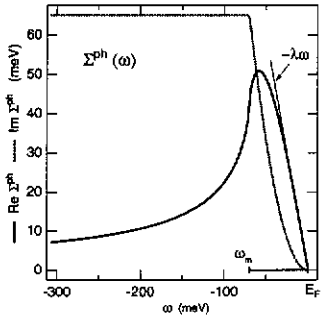

Figure 6.13: *Self-energy of the coupled electron-phonon system for an average coupling strength of* $\lambda = 1.18$. *Real and imaginary part are plotted as solid and dashed thick lines, respectively. The real part can be linearized close to* $\omega = 0$ *with slops* $-\lambda\omega$, *as indicated by the thin line. The phonon band width* ω_{max} *is indicated.*

reminiscent to results of other calculations [207–209] except for the imaginary part in the limit $\omega \to 0$. In contrast to calculations in three dimensions, where $Im\Sigma^{\rm ph}$ has a ω^3-dependence [207], the 2D results reveal a ω^2-law. The real part shows the expected linear dependence with slope $-\lambda$ and vanishes at E_F. At energies further than the maximum

phonon frequency from E_F, the real part decreases towards zero, whereas the imaginary part remains constant. The strong influence of the electron-phonon coupling on the structure of the spectral function is thus seen to be confined to a small energy region of the order of ω_m around the Fermi energy.

Up to this point, interactions other than the electron-phonon coupling have been neglected (see Appendix B). In our particular case, the self-energy must further comprise the electron-electron interaction and damping due to hole scattering at sample impurities and defects. To lowest order in the various interactions, the different contributions are simply summed up [6]:

$$\Sigma = \Sigma^{\text{ph}} + \Sigma^{\text{el-el}} + \Sigma^{\text{imp}}. \tag{6.5.3}$$

The isolation of the interesting electron-phonon term Σ^{ph} is a rather difficult task, because it necessitates an *a priori* estimation of the last two contributions. However, in the present situation, the conditions are favorable and offer a simple way to circumvent this difficulty. Firstly, the impurity term is purely imaginary and nearly constant in the small energy range of interest [143]. Secondly, the real part of the electron-electron term can be linearized close to the Fermi level on the scale of the electron bandwidth [24], leading to a constant change in the Fermi velocity v_F. If the experimentally observed dispersion $E(k) = \hbar v_F \times (k - k_F)$ is extrapolated from binding energies higher than the phonon bandwidth but small with respect to the electron bandwidth, $Re\Sigma^{\text{el-el}}$ is taken into account: $\varepsilon(\mathbf{k}) = \varepsilon^0(\mathbf{k}) + Re\Sigma^{\text{el-el}}(\mathbf{k},\omega)$. In order to implement the imaginary parts, a parameter $\Delta(\mathbf{k}) = Im\Sigma^{\text{el-el}}[\mathbf{k}, \omega = \varepsilon(\mathbf{k})] + Im\Sigma^{\text{imp}}$ is introduced, which is used in the first step of the analysis as a fitting parameter of the spectral function to the momentum resolved spectra (see App. B). Δ depends on energy through $\varepsilon(\mathbf{k})$. The electron-electron contribution can be calculated in two dimensions to yield [213]:

$$Im\Sigma^{\text{el-el}}(\mathbf{k},\omega) \propto \omega^2 \left[1 + 0.53\left|\ln\left(\frac{\omega}{E_F}\right)\right|\right], \tag{6.5.4}$$

where ω is measured from E_F. Equation (6.5.4) results in an almost parabolic function. When analyzing the experimental data, this function can not be distinguished from the well-known quadratic dependence in three dimensions [6,42]. The proportionality factor can be related to the electron density and the plasmon energy [24, 42], but this link is much less evident in two dimensions than in three. We will therefore analyze our data using both the 2D- and the 3D-formalisms. The resulting energy dependence of $\Delta[\varepsilon(\mathbf{k})]$ should reflect Eq.(6.5.4), with the addition of a constant term accounting for impurity scattering. Eq.(6.5.3) leads then to

$$\Sigma(\mathbf{k},\omega) = \Sigma^{\text{ph}}(\mathbf{k},\omega) + i\Delta(\mathbf{k}), \tag{6.5.5}$$

which is inserted into Eq.(2.3.19).

Back to the spectra, the emission angle Θ is fixed by the experiment and $\varepsilon(\mathbf{k})$ is given by extrapolation. With Δ as the only variable parameter, $G^<(\mathbf{k}(\Theta), \omega)$ is calculated from Eqs. (2.3.19) and (6.5.5) and multiplied by the Fermi function at 12 K. An example calculation is given in Appendix B. The resulting spectrum is then convoluted in $\mathbf{k}$-space with a Gaussian of width δk to account for the experimental angular resolution [37,38], the energy resolution being neglected. The intensity of each calculated spectrum is adjusted to the experimental counterpart by multiplication with a factor, found to vary only slightly with $\mathbf{k}$ (standard deviation 10%; see upper panel in Fig.6.15). This underlines the stability of the experimental conditions and the reproducibility of the spectra, which were recorded over a period of several weeks.

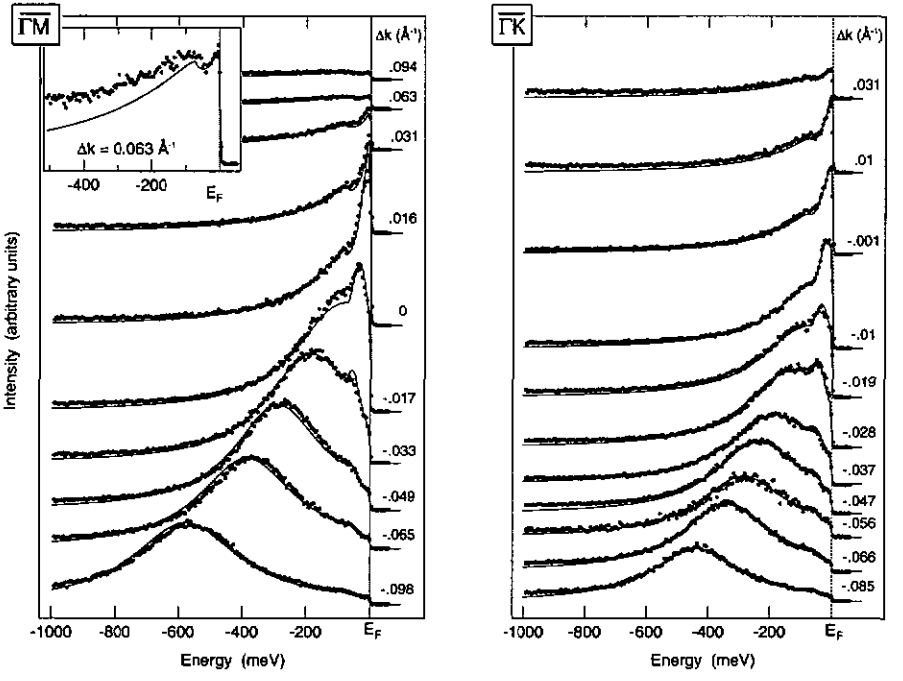

Figure 6.14: *Experimental spectra (dots) from Figs. 6.7 (left panel) and 6.11 (right panel), superimposed to the fitted line shapes (solid lines, see text for details). Spectra are labeled with the wavevectors* $\Delta k = k(E_F) - k_F$. *Insert: spectrum for* $k = 0.063\ \text{Å}^{-1}$, *enhanced in order to show the sharp peak pinned at* E_F.

The final results are superimposed to the experimental spectra as lines in Fig. 6.14 in order

to facilitate comparison. The calculation reproduces almost perfectly the double structure and the intensity ratio between the two main peaks. Anticipating Appendix B we can notice that the sharp peak at E_F for $k > k_F$ does not appear in the spectral function, if only electron-phonon coupling is included, in contrast to the weak structure at slightly higher binding energies (at $\sim \omega_m$, see inset in Fig. 6.14). It was found to be the remnant of the strong quasi-particle peak, centered far above E_F and broadened by Δ. It serves, thereby, as a sensitive probe for the fitting procedure.

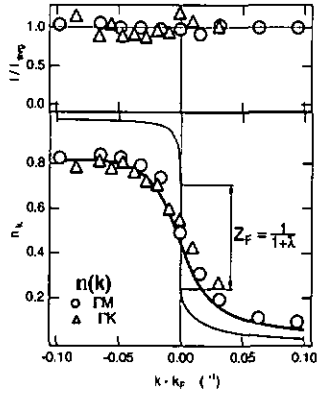

Figure 6.15: *Upper panel: intensity values used to adjust the calculations to the experimental spectra of Fig. 6.7 (open circles) and 6.11 (open triangles). Lower Panel: a comparison of experimental values (symbols) and theory (solid lines) for the momentum distribution $n(k)$. The thin line (a) is calculated for $T = 0$, $\Delta = 0$ and infinite angular resolution, the thick line (b) for $T = 0$, $\Delta(k)$ (from the fit results) and a resolution of* 0.2°.

In the lower panel of Fig.6.15 the theoretical momentum distribution $n(k)$ at $T = 0$, obtained by integration of the spectral function according to section 2.3, is plotted. Curve (a), calculated for the pure electron-phonon coupling, exbibits the expected discontinuity of height $Z = 1/(1 + \lambda)$ at k_F. Curve (b) takes both the experimental resolution and the parameter $\Delta(k)$ into account, the latter coming from the results of the lineshape fits (see below). The experimental values, obtained by integration of the photoemission spectra, are given by the symbols in the plot. The raw spectra have been used without any adjustment of their relative intensities. The errors due to the cutoff of the spectra at high binding energies and the inelastic background were found to be small, compared to the error radius of the experimental normalization procedure. The discontinuity is smeared out, but the intensity excess above k_F, typical for an interacting fermion system, is clearly reproduced.

With known parameter λ, the only variable fit parameter is Δ. The physical meaning of

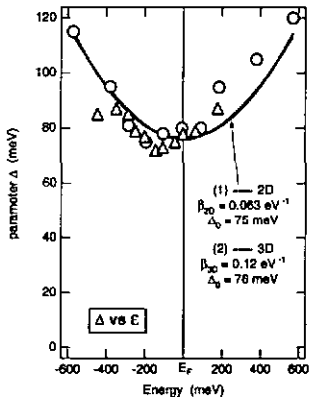

Figure 6.16: *Plot of the fit parameter Δ versus $\varepsilon(\mathbf{k})$; symbols like in Fig.6.15. The lines are fits using a two-dimensional (curve 1, thick line) and a three dimensional (curve 2, thin dashed line) model (see text for detail).*

Δ becomes clearer if one plots the values obtained as a function of the band energy $\varepsilon(\mathbf{k})$ (Fig.6.16). As anticipated above, this term can be decomposed into a constant offset value $\Delta_0 = 75$ meV and a pseudo-parabolic function (with curvature β). Fig.6.16 demonstrates that this functional form of Δ is a good approximation of the experimental values, and that only three parameters, λ, Δ_0, and β, are sufficient to fit the whole set of spectra. Using Eq.(6.5.4), a value of 0.063 eV^{-1} is found for the prefactor β_{2D} [curve (1) in Fig.6.16], whereas the calculation in three dimensions yields $\beta_{3D} = 0.12$ eV^{-1} [curve (2)]. Following the interpretation given in Ref. [24], the plasmon energy of the Coulomb gas can be derived from β_{3D}. A value of 13.3 eV is obtained from our analysis, which compares favorably with both bulk and surface plasmon energies of Be (19.5 eV and 11.3 eV, respectively [214]). A well founded prediction for Δ_0 is more speculative. The contribution of the electron-electron and electron-phonon interactions due to the finite measurement temperature are less than 1 meV and can, therefore, be neglected [213] (see App. B for the phonon part). Scattering due to surface disorder and impurities is taken to be the dominant mechanism. Δ_0 can be translated into a mean-free path λ_{mfp} in the surface plane:

$$\lambda_{\mathrm{mfp}} = v_F \tau = \frac{\partial [Z_{\mathbf{k}} \varepsilon(\mathbf{k})]}{\partial k} [2 Z_{\mathbf{k}} \Delta_0]^{-1} \approx 32 \text{ Å}. \tag{6.5.6}$$

A similar value was obtained in a recent study [188]. Such a correspondence can hardly be accidental and seems to indicate an inherent limitation of the quality of the Be(0001)-surface resulting from the preparation.

6.6 Different Approach, Discrepancies, and Improved Calculations

Quite often, one is confronted with anisotropic systems, where either the electronic dispersion, the coupling matrix element, or the phonon modes are highly dependent on absolute value and direction of k. In particular, this situation is realized in quasi-1D chain structures, where the strong coupling leads to phonon softening and strong nesting of the Fermi surface, so-called Kohn-anomalies. It is then desirable to extract important parameters directly from the experiment without supposing a model phonon DOS, for instance. Recently, photoemission spectra taken from Be(0001) were analyzed in a way allowing the self-energy to be determined experimentally [188]. The basic idea of this approach is to fit peak shapes ob-

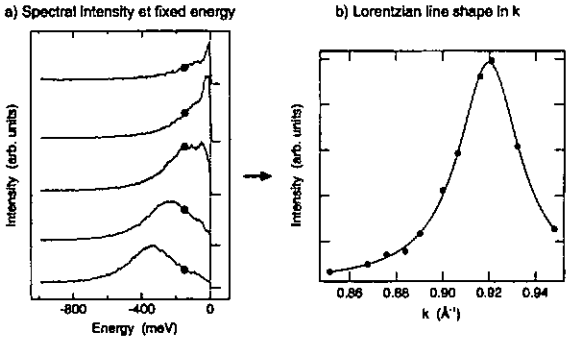

Figure 6.17: *Approach to find the self-energy Σ experimentally [188]: PE intensity is measured at fixed electron energy as function of the emission angle (solid circles in a) and reported vs the properly calculated wave vector (b). The function in k is a lorentzian; width and position can be used to deduce the imaginary and real parts of Σ, respectively.*

tained as function of momentum at fixed energy. This way of analysing the data is sketched in Fig. 6.17: the intensity is taken from the data for a certain energy (a) and reported versus the wave vector (part b). One then speaks of momentum distribution curves. Assuming again that the k-dependence of the self-energy can be neglected for a small range of wavevector around a particular $\mathbf{k}_F$, the spectral intensity depends on k solely by the band energy $\epsilon(\mathbf{k}) = \hbar v_F k$. The peak has lorentzian form. Width Δk and position k_0 of the lorentzian yield the imaginary and real parts of the self-energy, respectively:

$$Re\Sigma(\omega) = \omega - \hbar v_F k_0,$$

$$2Im\Sigma(\omega) = \hbar v_F \Delta k.$$

For Be(0001) along $\overline{\Gamma K}$, this analysis yields the self-energy presented in Fig. 6.18. Note that the instrumental resolution has not be taken into account. The real part can be fitted using a straight line close to $E_F = 0$. The slope was found to be $\lambda = 0.8$, in good agreement with the results in Ref. [188]. It is not clear where the discrepancy in the coupling parameter comes from. The neglected **k**-dependence of Σ or the unknown influence of impurities could cause shifts in both, the energy and momentum distribution curves, and thereby falsify the results. Jensen suggested that the energy range, used in Fig. 6.12 to fit the QP peak dispersion at E_F, could be too large (it was about 30 meV around E_F) [215]. Since this dispersion becomes rapidly flat, the resulting λ could be larger than the real one. An analysis of the momentum distribution curves should therefore yield more reliable quantitative results.

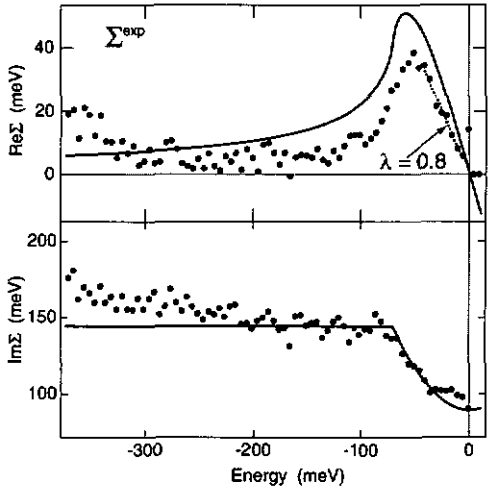

Figure 6.18: Σ, *as found experimentally using our raw data and the approach of LaShell* et al. *[188]. Upper panel: real part (dots) compared to the real part used in the calculations presented above (line); the dashed line is a fit to the real part close to the Fermi energy, from which a value* $\lambda \approx 0.8$ *can be deduced. Lower panel:* idem *for the imaginary part; note that the angular resolution has not be taken into account.*

Such a "measured" self-energy contains information about the structure of the Eliashberg-function. At $T = 0$, the imaginary phonon part of the electron self-energy can be written in

a more simple form[c]:

$$Im\Sigma(\omega) \propto \int_0^{\omega} d\tilde{\omega}\, \alpha^2 F(\tilde{\omega}). \tag{6.6.7}$$

It should thus be possible to extract the Eliashberg-function by calculating the derivative of the imaginary part of the self-energy.

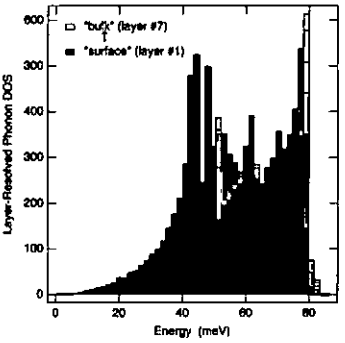

Figure 6.19: *13-layer slab-calculation of the phonon DOS of Be(0001). The DOS is plotted separately for the different layers, visualized by the grey shading: layer #1 and #13 are "surface layers" (dark grey), layer #7 the "bulk" (white). (Courtesy of J.B. Hannon / E. Jensen)*

Furthermore, we can use Eq. (6.6.7) to estimate the influence of the fine structure in the phonon DOS on the self-energy. The imaginary part of the self-energy will be calculated assuming a more realistic phonon DOS. The results will then be compared to those of our simple model presented in the preceding section. For the Be(0001)-surface, the phonon modes have been computed by Hannon using a 13-layer slab. Layers 1 and 13 are the "surfaces" of Be, the central layer (#7) is considered as "bulk". The results are presented in Fig. 6.19. The surface character is given by the grey scale, the dark shaded corresponding to the topmost surface layers. The Eliashberg-function (assuming a constant coupling strength) and the imaginary part of Σ, resulting from Eq. (6.6.7), are displayed in Fig. 6.20. The Eliashberg-function is normalized by its first reciprocal moment, which yields λ, according to Eq. (6.5.1). The results of the simple linear model are added as dashed lines. Despite the differences in the Eliashberg-function, the structure in $Im\Sigma$ is hardly discernible, and data with excellent statistics will be required in order to obtain detailed information about the phonons from the experimentally determined self-energy. The only remarkable difference is

[c]This follows from Eq. (6.5.2) by using the Dirac-identity. The Bose-Einstein factor can be neglected at $T = 0$.

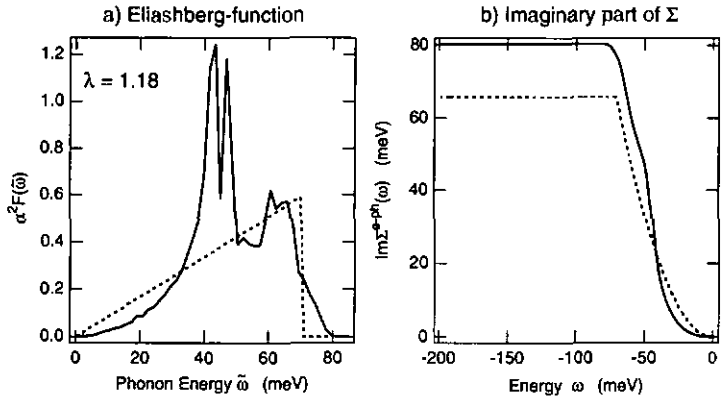

Figure 6.20: *Comparison of Eliashberg-function (a) and imaginary part of the electron-phonon self-energy (b), derived using the calculated surface phonon DOS of Hannon (solid thick line) and the simple model presented in this work (dashed lines).*

the functional form for $\omega \rightarrow 0$, yielding some ω^3-dependence, reminiscent of results for a 3D-system [207]. The apparent similarity between tbe imaginary parts of Σ emerging from the two models, confirms *a posteriori* the correctness of the simple model presented in this work.

6.7 Summary: Electron-Phonon Coupling in Two Dimensions

The results presented in tbis chapter show in an impressive way how many-body interactions influence line shapes in photoemission spectra. A very simple model, which requires only 3 parameters λ, β, and Δ_0 as input parameters, was proven to be sufficient to fit the whole set of spectra. The evolution of the peak shape with wave vector and energy, observed here, is *universal* and allows further systematic studies of interacting systems. This is confirmed by recent findings of other groups [188, 206]. It is interesting to note tbat similar calculations have been presented in order to model the line shapes observed in high-temperature superconductors [200]. Norman *et al.* constructed a somewhat modified Eliashberg-function reflecting electron-electron coupling mediated by collective modes and the energy gap, which opens up at the metal-superconductor phase transition, and they obtained good agreement between calculated and measured spectra.
It would be very interesting to look out for systems related to Be(0001). Some possibilities, which will be tackled in near future, are listed here:

- The Mg(0001)-surface provides a surface state similar to the $\overline{\Gamma}$-state of Be(0001) [176]. The band width was found to be smaller than on Be(0001), and the analysis is rendered difficult by the small band gap in the projected bulk band structure [216].

- Li evaporated onto Be(0001) acts as electron donator [217,218]. The surface undergoes a structural phase transition upon evaporation from the sub-monolayer ($\sqrt{3}\times\sqrt{3}R30°$) to the monolayer (ML) regime [219], where an quasi-commensurate 2×2 structure was found. At the same time, the Be surface state shifts to higher binding energies, reaching a band width of about 4 eV for 1 ML. A second, Li-induced state appears at roughly half a ML, and many-body effects have been shown to be important for the understanding of the observed peak shape [217]. This state is fully unoccupied at low coverages and becomes partially occupied at 1 ML [220].

- Be(0001) can be saturated by exposure to hydrogen [221, 222]. The phonon modes change drastically due to the interaction of H with Be surface atoms [221]. The peak shape of the Be surface state becomes larger upon exposure to H, and disappears at about 1 L[d]. A new surface state, induced by H, appears at slightly higher binding energy (about 4 eV). The latter shows similar dispersive behaviour as the $\overline{\Gamma}$-state on Be(0001) [222].

In all cases, the line shape evolution of similar surface states may be studied systematically as function of band width, phonon modes and coupling strength.

[d] 1 L = 1 Langmuir = 10^{-6} Torr sec.

Appendix A

Spectral Functions and Finite Temperature

As we have seen in Chapter 2.3 many-body problems can be tackled conveniently with the help of the Green's function formalism. It has been anticipated that, aside optical matrix elements, the photoemission spectrum $I(\omega, \mathbf{k})$ is linked to the spectral function $A(\omega, \mathbf{k})$ by

$$I(\omega, \mathbf{k}) \propto A(\omega, \mathbf{k}) f(\omega, T),$$

where $f(\omega, T)$ denotes the Fermi-Dirac distribution at energy ω and temperature T. $\omega = 0$ refers to the Fermi energy. This relation has to be justified for interacting systems, what is the concern of this appendix (a detailed demonstration can be found in Ref. [48].).
Starting point is the Green's function $G^<$, which we will show to yield the electron-removal spectrum. For the sake of simplicity, space and momentum variables will be omitted in the following. Green's functions have 2 time variables t and t', but they can be shown to depend solely on the difference $t - t'$, if the Hamiltonian of the system does not depend on time [47]. We will therefore set $t' = 0$. $G^<$ is then defined by [48]:

$$G^<(t) \equiv i \langle a^\dagger(0) a(t) \rangle, \; t < 0.$$

This means that we annihilate an electron at time $t < 0$ and map the new $(N-1)$-particle state onto the N-particle state at $t = 0$ by recreating the electron. The brackets denote that we have to take the average in the grand-canonical ensemble, yielding:

$$\begin{aligned} G^<(t) &= i \langle a^\dagger(0) a(t) \rangle & \text{(A.0.1)} \\ &= i \frac{1}{\Xi} Tr \left[e^{-\beta(\hat{H} - \mu \hat{N})} a^\dagger e^{i(\hat{H} - \mu \hat{N})t} a e^{-i(\hat{H} - \mu \hat{N})t} \right] \\ &= i \frac{1}{\Xi} \sum_{n,m} |\langle N-1, m | \, a \, | N, n \rangle|^2 \, e^{-\beta[E_n - \mu N]} e^{-i[E_m - \mu(N-1)]t} e^{i[E_n - \mu N]t}. & \text{(A.0.2)} \end{aligned}$$

In the last step we used the representation due to Lehmann by introducing complete sets of eigen states n and m between the operators [48]. Ξ, μ, and $\hat{N}$ denote the partition function,

chemical potential, and number operator, respectively. $\beta = (k_B T)^{-1}$ gives the temperature. Using the Fourier time-frequency transform,

$$G^<(\omega) = \int_{-\infty}^{0} dt\, e^{i\omega t} e^{-\delta t} G^<(t)$$

in the limit $\delta \to 0^+$, Eq. (A.0.2) can be evaluated:

$$G^<(\omega) = \frac{1}{\Xi} \sum_{n,m} |\langle N-1, m| a |N, n\rangle|^2 \, \delta[\omega - (E_n - E_m - \mu)]\, e^{-\beta[E_n - \mu N]}. \qquad \text{(A.0.3)}$$

A comparison of Eq. (A.0.3) to Eq. (2.1.5) in section 2.1 shows that the photoemission spectrum is indeed directly proportional to $G^<$.

On the other hand, the excitation spectrum of the system is given by the spectral function (sometimes called propagator) $A(\omega)$. In simple words, the spectral function gives the probability amplitude at time t that the system is still in the excited state created at time $t = 0$ [43]. It can be found for example by calculating the self-energy by means of diagrammatic techniques or by solution of the equation of motion of a suitable Green's function. Three important kinds of Green's functions are usually found in the literature. G^{adv} and G^{ret} are named advanced and retarded Green's function, respectively, G^c is the causal Green's function. The differences are subtle but important because they influence the analytic properties of the functions. Temperature can be included in any kind of Green's function by calculating the thermal trace instead of the ground state expectation value [48]. For our purpose, we choose the advanced Green's function, which is related to the spectral function by

$$A(\omega) = \frac{1}{\pi} Im G^{adv}(\omega - i\delta)$$

in the limit $\delta \to 0^+$.

Starting from the definition $G^{\mathrm{adv}}(t) \equiv i\Theta(-t) \left\langle \left[a_{\mathrm{k}}^\dagger(t), a_{\mathrm{k}}(0) \right]_+ \right\rangle$ [43], where Θ denotes the unit step function, we obtain:

$$Im G^{adv}(\omega) = \frac{1}{\Xi} \sum_{n,m} |\langle N-1, m| a |N, n\rangle|^2 \, \delta[\omega - (E_n - E_m - \mu)] e^{-\beta[E_n - \mu N]} \left(1 + e^{\beta\omega}\right). \qquad \text{(A.0.4)}$$

It is easily seen that the right-hand-side of Eq. (A.0.4) differs from that of Eq. (A.0.3) just by the factor $(1 + e^{\beta\omega})$, i.e.

$$G^<(\omega) = Im G^{adv}(\omega) \left(1 + e^{\beta\omega}\right)^{-1} = Im G^{adv}(\omega) f(\omega, T) \quad \text{q.e.d.} \; . \qquad \text{(A.0.5)}$$

Hence, even for interacting systems, the occupation probability is given by the Fermi-Dirac distribution at temperature T [43, 48]. Provided that the spectral function $Im G^{adv}(\omega)$ has been properly calculated for temperature T, the photoemission spectrum is obtained by multiplying by the Fermi-function $f(\omega, T)$.

Appendix B

Example Calculation of a Photoemission Spectrum

In a photoemission spectrum, the emission angle is fixed and the momentum varies as function of the measured electron energy. Since we assumed the self-energy to be k-independent, the spectral function depends on k only through $\varepsilon(\mathbf{k})$. Hence, we can start directly with the self-energy given by Grimvall [209]:

$$\Sigma^{\mathrm{ph}}(\omega) = \int_{-E_F}^{\infty} d\epsilon \int_{0}^{\omega_m} d\tilde{\omega}\, \alpha^2 F(\tilde{\omega}) \times \left\{ \frac{1 - f(\epsilon,T) + N(\tilde{\omega},T)}{\omega - \epsilon - \tilde{\omega} + i\delta^{\pm}} + \frac{f(\epsilon,T) + N(\tilde{\omega},T)}{\omega - \epsilon + \tilde{\omega} + i\delta^{\pm}} \right\}. \tag{B.0.1}$$

$f(\epsilon,T)$ and $N(\tilde{\omega},T)$ are the Fermi-Dirac and Bose-Einstein distributions, respectively. The Eliashberg-function $\alpha^2F(\tilde{\omega})$ was approximated by $\alpha^2F(\tilde{\omega}) = \lambda\tilde{\omega}/(2\omega_m)$ with a cut off at ω_m. We will restrict ourselves to $T = 0$ and $\omega \leq 0$, thus $i\delta^{\pm} = -i\delta$. Extension to energies above E_F is trivial due to the symmetry of the self-energy. Moreover, at $T = 0$, the Bose-Einstein factors can be omitted. Exchanging the two integrations in Eq. (B.0.1) over $\tilde{\omega}$ and ϵ leads to

$$\Sigma^{\mathrm{ph}}(\omega) = \frac{\lambda}{2\omega_m} \int_{0}^{\omega_m} d\tilde{\omega}\, \tilde{\omega} \times \int_{-E_F}^{\infty} d\epsilon \left\{ \frac{1 - \Theta(-\epsilon)}{\omega - \epsilon - \tilde{\omega} - i\delta} + \frac{\Theta(-\epsilon)}{\omega - \epsilon + \tilde{\omega} - i\delta} \right\}. \tag{B.0.2}$$

$\Theta(x)$ is the unit step function, i.e. equal to 1 for $x \geq 0$ and 0 otherwise. With Ω as upper limit of the electron band width, the ϵ-integration can be calculated analytically to yield:

$$\int_{-E_F}^{\Omega} d\epsilon \quad \left\{ \frac{1-\Theta(-\epsilon)}{\omega-\epsilon-\tilde{\omega}-i\delta} + \frac{\Theta(-\epsilon)}{\omega-\epsilon+\tilde{\omega}-i\delta} \right\}$$
$$= \frac{1}{2}\ln\left|\frac{(\omega-\tilde{\omega})^2}{(\omega+\tilde{\omega})^2+\delta^2}\right| + \frac{1}{2}\ln\left|\frac{(\omega+\tilde{\omega}+E_F)^2}{(\omega+\tilde{\omega}-\Omega)^2+\delta^2}\right| +$$
$$+ i\left[\arctan\left(\frac{\omega+\tilde{\omega}}{\delta}\right) + \arctan\left(\frac{\omega-\tilde{\omega}}{\delta}\right)\right]. \qquad \text{(B.0.3)}$$

The integration over the phonon frequencies has been evaluated numerically. One interesting property of the real part in Eq. (B.0.3) has to be pointed out: the real part does not vanish on the Fermi surface ($\omega = 0$) unless $\Omega = E_F \gg \omega_m$. This condition means that the band has to be half filled, and that particle-hole symmetry is supposed. The self-energy finally takes the following form:

$$Re\Sigma(\omega) = \frac{\lambda}{4\omega_m}\int_0^{\omega_m} d\tilde{\omega}\,\tilde{\omega}\left[\ln\left|\frac{(\omega-\tilde{\omega})^2}{(\omega+\tilde{\omega})^2+\delta^2}\right| + \ln\left|\frac{(\omega+\tilde{\omega}+E_F)^2}{(\omega+\tilde{\omega}-\Omega)^2+\delta^2}\right|\right], \qquad \text{(B.0.4)}$$

$$Im\Sigma(\omega) = \frac{\lambda}{2\omega_m}\int_0^{\omega_m} d\tilde{\omega}\,\tilde{\omega}\left[\arctan\left(\frac{\omega+\tilde{\omega}}{\delta}\right) + \arctan\left(\frac{\omega-\tilde{\omega}}{\delta}\right)\right]. \qquad \text{(B.0.5)}$$

Extension of the calculation to finite temperature necessitates the solution of the Sommerfeld-expansion [1], which is a rather difficult task. We only note that the imaginary part behaves at $\omega = 0$ to leading order as $(k_BT)^2/\omega_m$ times a factor of order unity. Grimvall showed that, at high temperature and close to E_F, $Im\Sigma \propto \lambda k_BT$ [210].
The photoemission spectrum for emission angle Θ_e is then given by (see e.g. Chapter 2.3 and App. A):

$$G^<(\Theta_e,\omega) = \frac{1}{\pi}\frac{Im\Sigma(\omega)}{[\omega-\varepsilon(k_{\Theta_e})-Re\Sigma(\omega)]^2+[Im\Sigma(\omega)]^2}\,f(\omega,T), \qquad \text{(B.0.6)}$$

with $k_{\Theta_e} = 0.512\sqrt{h\nu+\omega-\phi}\sin(\Theta_e)$. $G^<(\Theta_e,\omega)$ has to be convoluted with a Gaussian of width δk, accounting for the finite angular resolution of the spectrometer. A selection of spectra, calculated in this way, is plotted in Fig. B.1 together with the corresponding experimental curves. As already mentioned in Chapter 6, the sharp peak pinned at E_F for $k > k_F$ is not reproduced. Electron-electron and impurity scattering have to be incorporated, as shown in Chapter 6.

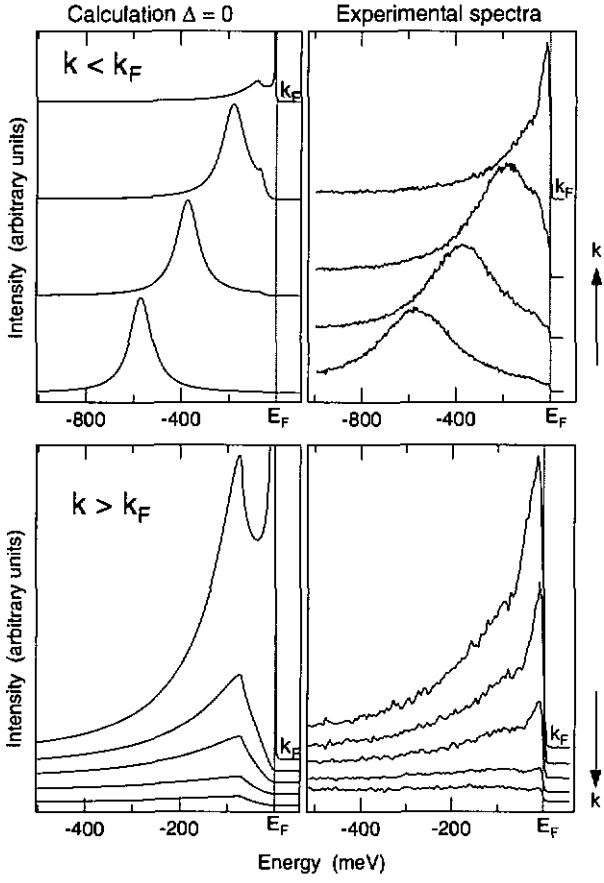

Figure B.1: *Comparison of the spectral function (left panel), calculated using only the phonon part of the electron self-energy, to the experimental spectra for $k < k_F$ (top panel) and $k > k_F$ (bottom panel). Note the directions of increasing k, indicated on the right.*

Bibliography

[1] N.W. Ashcroft and N.D. Mermin, *Solid State Physics*, Saunders College (Philadelphia), 1976.

[2] L.D. Landau, *The Theory of a Fermi Liquid*, Sov. Phys. JETP **3**, 920 (1957).

[3] P. Nozières, *Theory of Interacting Fermi Systems*, W.A. Benjamin (New York, Amsterdam), 1964.

[4] J. Callaway, *Quantum Theory of the Solid State*, student edition, Academic Press (San Diego), 1974.

[5] W.A. Harrison, *Solid State Theory*, Dover Publ. (New York), 1979.

[6] L. Hedin and S. Lundqvist, *Effects of Electron-Electron and Electron-Phonon Interactions on the One-Electron States of Solids*, Vol. 23 of *Solid State Physics: Advances in Research and Applications*, ed. by F. Seitz, D. Turnbull and H. Ehrenreich, Academic Press (New York, London), 1969.

[7] D. Pines and D. Bohm, *A Collective Description of Electron Interactions: II. Collective vs Individual Particle Aspects of the Interactions*, Phys. Rev. **85**, 338 (1952).

[8] O. Madelung, *Introduction to Solid-State Theory*, Vol. 2 of *Springer Series in Solid State Sciences*, ed. by M. Cardona, P. Fulde, and H.J. Queisser, Springer-Verlag (Berlin), 1978.

[9] D. Malterre, M. Grioni, and Y. Baer, *Recent Developments in High-Energy Spectroscopies of Kondo Systems*, Adv. Phys. **45**, 299 (1996).

[10] R.E. Peierls, *Quantum Theory of Solids*, chapter 5, *Int. Series of Monographs on Physics*, ed. by N.F. Mott and E.C. Bullard, Oxford at Clarendon Press (Oxford), 1955.

[11] G. Grüner, *Density Waves in Solids*, Vol. 89 of *Frontiers in Physics*, ed. by D. Pines, Addison Wesley (Reading, Menlo Park, New York), 1994.

[12] J.M. Luttinger, *An Exactly Soluble Model of a Many-Fermion System*, J. Math. Phys. **4**, 1154 (1963).

[13] J. Sólyom, *The Fermi Gas of One-Dimensional Conductors*, Adv. Phys. **28**, 201 (1979).

[14] J. Voit, *One-Dimensional Fermi Liquids*, Rep. Prog. Phys. **57**, 977 (1994).

[15] B. Dardel, D. Malterre, M. Grioni, P. Weibel, and Y. Baer, *Unusual Photoemission Spectral Function of Quasi-One-Dimensional Metals*, Phys. Rev. Lett. **67**, 3144 (1991).

[16] B. Dardel, D. Malterre, M. Grioni, P. Weibel, Y. Baer, J. Voit, and D. Jérôme, *Possible Observation of a Luttinger-Liquid Behaviour from Photoemission Spectroscopy of One-Dimensional Organic Conductors*, Phys. Rev. B **24**, 687 (1993).

[17] B. Dardel, *Etude par Photoémission des Excitations de Basse Energie et Transitions de Phases dans les Composés de Basse Dimension*, PhD thesis, Université de Neuchâtel, 1994.

[18] J.W. Allen, G.-H. Gweon, R. Claessen, and K. Matho, *Fermi Liquids and Non-Fermi Liquids - the View from Photoemission*, J. Phys. Chem. Solids **56**, 1849 (1995).

[19] K. Breuer, *Electronic Structure of Quasi-Low Dimensional Oxide Conductors*, PhD thesis, Boston University, 1996.

[20] C. Kim, Z.-X. Shen, N. Motoyama, H. Eisaki, S. Uchida, T. Tohyama, and S. Maekawa, *Separation of Spin and Charge Excitations in One-Dimensional $SrCuO_2$*, Phys. Rev. B **56**, 15589 (1997).

[21] J.D. Denlinger, G.-H. Gweon, J.W. Allen, C.G. Olsen, J. Marcus, C. Schlenker, and L.-S. Hsu, *Non-Fermi-Liquid Single Particle Line Shape of the Quasi-One-Dimensional Non-CDW Metal $Li_{0.9}Mo_6O_{17}$: Comparison to the Luttinger Liquid*, Phys. Rev. Lett. **82**, 2540 (1999).

[22] J. Xue, L.-C. Duda, K.E. Smith, A.V. Fedorov, P.D. Johnson, S.L. Hulbert, W. McCarroll, and M. Greenblatt, *Electronic Structure near the Fermi Surface in the Quasi-One-Dimensional Conductor $Li_{0.9}Mo_6O_{17}$*, Pbys. Rev. Lett. **83**, 1235 (1999).

[23] P. Segovia, D. Purdie, M. Hengsberger, and Y. Baer, *Observation of Spin and Charge Collective Modes in One-Dimensional Metallic Chains*, Nature (London) **402**, 504 (1999).

[24] R. Claessen, R.O. Anderson, J.W. Allen, C.C. Olson, C. Janowitz, W.P. Ellis, S. Harm, M. Kalning, R. Manzke, and M. Skibowski, *Fermi-Liquid Line Shapes Measured by Angle-Resolved Photoemission Spectroscopy on 1T-$TiTe_2$*, Phys. Rev. Lett. **69**, 808 (1992).

[25] M. Grioni and J. Voit, *Electron Spectroscopies Applied to Low-Dimensional Materials*, ed. by H. Stanberg and H. Hugbes, Kluwer (Dordrecht), 1999.

[26] M. Hengsberger, D. Purdie, M. Garnier, K. Breuer, and Y. Baer, *Observation of Superstructure Periodicity in Angle-Resolved Photoemission from Cu(610)*, Surf. Sci. **405**, L491 (1998).

[27] D. Purdie, M. Hengsberger, M. Garnier, and Y. Baer, *An Outlook for High-Resolution uv Photoelectron Spectroscopy of Solids at Low Temperature*, Surf. Sci. **407**, L671 (1998).

[28] M. Hengsberger, D. Purdie, P. Segovia, M. Garnier, and Y. Baer, *Photoemission Study of a Strongly Coupled Electron-Phonon System*, Phys. Rev. Lett. **83**, 592 (1999).

[29] M. Hengsberger, R. Frésard, D. Purdie, P. Segovia, and Y. Baer, *Electron-Phonon Coupling in Photoemission Spectra*, Phys. Rev. B **60**, 10796 (1999).

[30] P.J. Feibelman and D.E. Eastman, *Photoemission Spectroscopy - Correspondence between Quantum Theory and Experimental Phenomenology*, Phys. Rev. B **10**, 4932 (1974).

[31] R. Courths and S. Hüfner, *Photoemission Experiments on Copper*, Phys. Reports **112**, 53 (1984).

[32] S. Hüfner, *Photoelectron Spectroscopy: Principles and Applications*, Vol. 82 of *Springer Series in Solid State Sciences*, ed. by M. Cardona, Springer-Verlag (Berlin, Heidelberg, New York), 1995.

[33] R. Matzdorf, *Investigation of Lineshapes and Line Intensities by High-Resolution uv-Photoemission Spectroscopy - some Case Studies on Noble Metal Surfaces*, Surf. Sci. Reports **30**, 153 (1998).

[34] M. Grioni, *Photoelectron Spectroscopies for Beginners: a Brief Introduction*, Series of lectures given in Grenoble 1995, unpublished.

[35] T. Miller, W.E. McMahon, and T.-C. Chiang, *Interference between Bulk and Surface Photoemission Transitions in Ag(111)*, Phys. Rev. Lett. **77**, 1167 (1996).

[36] E.D. Hansen, T. Miller, and T.-C. Chiang, *Overlayer Test of Surface Photoemission Effect in Cu(100)*, Phys. Rev. Lett. **78**, 2807 (1997).

[37] P. Thiry, *Photoémission angulaire dans les solides*, PhD thesis, Université Paris-Sud, 1981.

[38] N.V. Smith, *Quasiparticle Lifetimes from Angle-Resolved Photoemission*, Comments Cond. Mat. Phys. **15**, 263 (1992).

[39] N.V. Smith, P. Thiry, and Y. Petroff, *Photoemission Linewidths and Quasiparticle Lifetimes*, Phys. Rev. B **47**, 15476 (1993).

[40] J. Hermanson, *Final State Symmetry and Polarisation Effects in Angle-Resolved Photoemission Spectroscopy*, Solid State Commun. **22**, 9 (1977).

[41] D. Pescia, A.R. Law, M.T. Johnson, and H.P. Hughes, *Determination of Observable Conduction Band Symmetry in Angle-Resolved Electron Spectroscopies: Non-Symmorphic Space Groups*, Solid State Commun. **56**, 809 (1985).

[42] J.J. Quinn and R.A. Ferrell, *Electron Self-Energy Approach to Correlation in a Degenerate Electron Gas*, Phys. Rev. **112**, 812 (1958).

[43] W. Nolting, *Grundkurs Theoretische Physik VII: Viel-Teilchen-Theorie*, Verlag Zimmermann-Neufang (Ulmen), 1991.

[44] S. Harm, R. Dürig, R. Manzke, M. Skibowski, R. Claessen, and J.W. Allen, *Fermi Liquid Spectral Function and Angle Resolved Photoelectron Spectra of the Ti-3d_{z^2}-Band of $TiTe_2$*, J. Electron Spectr. **68**, 11 (1994).

[45] G.A. Sawatzky, *On the Electronic Structure and Related Physical Properties of 3d Transition Metal Compounds*, Proc. of the Spring College in Condensed Matter and Superconductivity, Trieste, 1992.

[46] J.M. Luttinger, *Fermi Surface and Some Simple Equilibrium Properties of a System of Interacting Fermions*, Phys. Rev. **119**, 1153 (1960).

[47] G. Rickayzen, *Green's Functions and Condensed Matter*, in *Techniques of Physics*, ed. by N.H. March and H.N. Daglish, Academic Press (London, New York), 1980.

[48] J.W. Negele and H. Orland, *Quantum Many-Particle Systems*, Frontiers in Physics, Lecture Note Series, Addison-Wesley Publ. (Redwood City), 1988.

[49] M. Garnier, *High Resolution Photoemission Study of Well-Ordered Cerium Surface Compounds*, PhD thesis, Université de Neuchâtel, 1998.

[50] M.A. van Hove, W. H. Weinberg, and C.M. Chan, *Low-Energy Electron Diffraction*, Vol. 6 of *Springer Series in Surface Sciences*, ed. by G. Ertl and R. Gomer, Springer-Verlag (Berlin, Heidelberg, New York, London), 1986.

[51] M. Henzler and W. Göpel, *Oberflächenphysik des Festkörpers*, Teubner-Verlag (Stuttgart), 1991.

[52] L.E. Davis, N.C. McDonald, P.W. Palmberg, G.E. Riach, and R.E. Weber, *Handbook of Auger Electron Spectroscopy*, 1976, Physical Electronics Industries, Inc. (Perkin-Elmer Corp., Eden Prairie), 2nd Ed.

[53] J.A.R. Samson, *Line Broadening in Photoelectron Spectroscopy*, Rev. Sci. Instrum. **40**, 1174 (1969).

[54] P. Baltzer, L. Karlsson, M. Lundqvist, and B. Wannberg, *Resolution and Signal-to-Background Enhancement in Gas-Phase Electron Spectroscopy*, Rev. Sci. Instrum. **64**, 2179 (1993).

[55] E. Principi, *Test Préliminaires d'un Monochromateur uv pour les Mesures de Spectroscopie d'Electrons à Haute Résolution ...* , Master's thesis, Université de Neuchâtel, 1990.

[56] T. Finteis, ... *Messungen an Gasentladungslampen im Vakuum-uv-Bereich*, Master's thesis, Universität des Saarlandes, Saarbrücken/Germany, 1994.

[57] Gammadata AB; Uppsala/Sweden, *User's Guide VUV 5000 Source*, 1995.

[58] T. Pillo, L. Patthey, E. Boschung, J. Hayoz, P. Aebi, and L. Schlapbach, *A Monochromatized Multiple Energy Laboratory uv Source for k-Space Imaging*, J. Electron Spectr. Rel. Phen. **97**, 243 (1998).

[59] Jobin Yvon Instr. SA, Ray Tracing Calculations for a Holographic Grating.

[60] edited by H. Gobrecht, *Bergmann-Schäfer Experimentalphysik III: Optik*, de Gruyter (Berlin), 8th edition, 1987.

[61] P. Baltzer and J.-O. Forsell, *Test Runs Performed with a Toroidal Grating Monochromator*, 1996.

[62] P. Baltzer, B. Wannberg, and M.C. Göthe, *Optimization and Redesign of an Electron Spectrometer for High-Resolution Gas-Phase uv Photoelectron, Auger Electron, and Ion Fragment Spectroscopy*, Rev. Sci. Instrum. **62**, 643 (1991).

[63] Scienta Instrument AB, Uppsala, Sweden, *An Introduction to the Scienta SES-200 Analyser*.

[64] J.P. Eberhart, *Analyse Structurale et Chimique des Matériaux*, BORDAS/Dunod (Paris), 1989.

[65] I.R. Collins, J.T. Moran, P.T. Andrews, R. Cosso, J.D. O'Mahony, J.F. McGilp, and G. Margaritondo, *Angle-Resolved Photoemission from an Unusual Quasi-One-Dimensional Metallic System: a Single-Domain Au-Induced 5x2 Reconstruction of Si(111)*, Surf. Sci. **325**, 45 (1995).

[66] F.J. Himpsel, J.E. Ortega, G.J. Mankey, and R.F. Willis, *Magnetic Nanostructures*, Adv. Phys. **47**, 511 (1998).

[67] J. Heremans and O.P. Hansen, *Influence of Non-Parabolicity on Intravalley Electron-Phonon Scattering; the Case of Bismuth*, J. Phys. C: Solid State Phys. **12**, 3483 (1979).

[68] X. Gonze, J.-P. Michenaud, and J.-P. Vigneron, *First-Principles Study of As, Sb, and Bi Electronic Properties*, Phys. Rev. B **41**, 11827 (1990).

[69] Z. Zhang, X. Sun, M.S. Dresselhaus, J.Y. Ying, and J.P. Heremans, *Magnetotransport Investigations of Ultrafine Single-Crystalline Bismuth Nanowire Arrays*, Appl. Phys. Lett. **73**, 1589 (1998).

[70] J. Heremans, C.M. Thrush, Z. Zhang, X. Sun, M.S. Dresselhaus, J.Y. Ying, and D.T. Morelli, *Magnetoresistance of Bismuth Nanowire Arrays: a Possible Transition from One-Dimensional to Three-Dimensional Localization*, Phys. Rev. B **58**, R10091 (1998).

[71] J.M. Krans and J.M. van Ruitenbeek, *Subquantum Conductance Steps in Atom-Sized Contacts of the Semimetal Sb*, Phys. Rev. B **50**, 17659 (1994).

[72] J.L. Costa-Krämer, N. García, and H. Olin, *Conductance Quantization in Bismuth Nanowires*, Phys. Rev. Lett. **78**, 4990 (1997).

[73] N. Garcia, Y.H. Kao, and M. Strongin, *Galvanomagnetic Studies of Bismuth Films in the Quantum-Size-Effect Region*, Phys. Rev. B **5**, 2029 (1972).

[74] V. de Renzi, M.G. Betti, and C. Mariani, *Quantum Size Effects and Temperature Dependence of Low-Energy Electronic Excitations in Thin Bi Crystals*, Phys. Rev. B **48**, 4767 (1993).

[75] Y.F. Komnik, E.I. Bukhshtab, Y.V. Nikitin, and V.V. Andrievskiĭ, *Features of Temperature Dependence of the Resistance of Thin Bismuth Films*, Sov. Phys. JETP **33**, 364 (1971).

[76] R.A. Hoffman and D.R. Frankl, *Electrical Transport Properties of Thin Bismuth Films*, Phys. Rev. B **3**, 1825 (1971).

[77] Y. Hu, T.J. Wagener, M.B. Jost, and J.H. Weaver, *Evolution of Empty-State Bands for Bi/GaAs(110): from Bi zigzag Chains to Ordered Overlayers*, Phys. Rev. B **40**, 1146 (1989).

[78] Y. Hu, M.B. Jost, T.J. Wagner, and J.H. Weaver, *Long-Range Ordering of Sb Multilayers on GaAs(110): Evolution of Resonant Inverse Photoemission*, Phys. Rev. B **42**, 7050 (1990).

[79] J.C. Patrin, Y.Z. Li, M. Chander, and J.H. Weaver, *Sb and Bi on GaAs(110): Substrate-Stabilized Overlayer Structures Studied with Scanning Tunneling Microscopy*, Phys. Rev. B **46**, 10221 (1992).

[80] M.C. Betti, V. Corradini, U. del Pennino, V. de Renzi, P. Fantini, and C. Mariani, *Gap-State Formation in Two-Dimensional Ordered Bi Layers on InAs(110)*, Phys. Rev. B **58**, R4231 (1998).

[81] F.Y. Yang, K. Liu, D.H. Reich, P.C. Searson, and C.L. Chien, *Large Magnetoresistance of Electrodeposited Single-Crystal Bismuth Films*, Science **284**, 1335 (1999).

[82] L. Gavioli, M.G. Betti, and C. Mariani, *Electronic Properties of the Bi/Si(100) Interface*, Surf. Sci. **409**, 207 (1998).

[83] K. Miki, D.R. Bowler, J.H.G.Owen, G.A.D. Briggs, and K. Sakamoto, *Atomically Perfect Bismuth Lines on Si(001)*, Phys. Rev. B **59**, 14868 (1999).

[84] L.M. Falicov and S. Golin, *Electronic Band Structure of Arsenic. I. Pseudopotential Approach*, Phys. Rev. **137**, A871 (1965).

[85] L.M. Falicov and P.J. Lin, *Band Structure and Fermi Surface of Antimony: Pseudopotential Approach*, Phys. Rev. **141**, 562 (1966).

[86] S. Golin, *Band Structure of Bismuth: Pseudopotential Approach*, Phys. Rev. **166**, 643 (1968).

[87] R.J. Needs, R.M. Martin, and O.H. Nielsen, *Total-Energy Calculations of the Structural Properties of the Croup-V Element Arsenic*, Phys. Rev. B **33**, 3778 (1986).

[88] J. Rose and R. Schuchardt, *A Theoretical Investigation of the Fermi Surfaces of Bismuth and Antimony*, Phys. Status Solidi B **117**, 213 (1983).

[89] X. Gonze, J.-P. Michenaud, and J.-P. Vigneron, *Ab Initio Calculations of Bismuth Properties, including Spin-Orbit Coupling*, Phys. Scripta **37**, 785 (1988).

[90] V.S. Édel'man, *Electrons in Bismuth*, Adv. Phys. **25**, 555 (1976).

[91] B. Weitzel and H. Micklitz, *Superconductivity in Granular Systems Built from Well-Defined Rhombohedral Bi Clusters: Evidence for Bi-Surface Superconductivity*, Phys. Rev. Lett. **66**, 385 (1991).

[92] G. Jezequel, Y. Petroff, R. Pinchaux, and F. Yndurain, *Electronic Structure of the Bi(111) Surface*, Phys. Rev. B **33**, 4352 (1986).

[93] G. Jezequel, J. Thomas, and I. Pollini, *Experimental Band Structure of Semimetal Bismuth*, Phys. Rev. B **56**, 6620 (1997).

[94] A. Tanaka, M. Hatano, K. Takahashi, H. Sasaki, S. Suzuki, and S. Sato, *Bulk and Surface Electronic Structure of the Semimetal Bi Studied by Angle-Resolved Photoemission Spectroscopy*, Phys. Rev. B **59**, 1786 (1999).

[95] F. Patthey, W.-D. Schneider, and H. Micklitz, *Photoemission Study of the Bi(111) Surface*, Phys. Rev. B **49**, 11293 (1994).

[96] R.M. Goodman and G.A. Somorjai, *Low-Energy Electron Diffraction Studies of Surface Melting and Freezing of Lead, Bismuth and Tin Single-Crystal Surfaces*, J. Chem. Phys. **52**, 6325 (1970).

[97] G. Kittel, *Einführung in die Festkörperphysik*, 8th edition, Oldenbourg (München, Wien), 1989.

[98] G. Jezequel, A. Barski, P. Steiner, F. Solal, P. Rouhin, R. Pinchaux, and Y. Petroff, *Indirect Transitions in Angle-Resolved Photoemission*, Phys. Rev. B **30**, 4833 (1984).

[99] L. Ley, R.A. Pollack, S.P. Kowalczyk, R. McFeely, and D.A. Shirley, *Evidence for Covalent Bonding in Crystalline and Amorphous As, Sb, and Bi from Valence-Band Photoelectron Spectra*, Phys. Rev. B **8**, 641 (1973).

[100] F. Manghi and E. Molinari, *Aspects of Self-Consistent Procedures in Surface Pseudopotential Calculations*, J. Phys. C: Solid State Phys. **15**, 3627 (1982).

[101] R. Zeller, *Band Structure Methods*, Vol. 69 of *Topics in Applied Physics*, ed. by J.C. Fuggle and J.E. Inglesfield, Springer-Verlag (Berlin, Heidelberg), 1992.

[102] A.A. Abrikosov and L.A. Falkovskiĭ, *Theory of the Electron Energy Spectrum of Metals with a Bismuth Type Lattice*, Sov. Phys. JETP **16**, 769 (1963).

[103] J.G. Slater and G.F. Koster, *Simplified LCAO Method for the Periodic Potential Problem*, Phys. Rev. **94**, 1498 (1954).

[104] Y. Liu and R.E. Allen, *Electronic Structure of the Semimetals Bi and Sb*, Phys. Rev. B **52**, 1566 (1995).

[105] M.H. Cohen, *Energy Bands in the Bismuth Structure. I. A Nonellipsoidal Model for Electrons in Bi*, Phys. Rev. **121**, 387 (1961).

[106] R.J. Dinger and A.W. Lawson, *Cyclotron Resonance and the Cohen Nonellipsoidal Model for Bismuth. III. Experimental Results*, Phys. Rev. B **7**, 5215 (1973).

[107] J. Heil, M. Primke, K.U. Würz, and P. Wyder, *Real Space Imaging of Ballistic Carrier Propagation in Bi Single Crystals*, Phys. Rev. Lett. **74**, 146 (1995).

[108] J. Heil, M. Primke, A. Böhm, A. Gröger, and P. Wyder, *Elektronenfokussierung in Metallen*, Phys. Blätter **53**, 877 (1997).

[109] R.A. Herrod, C.A. Cage, and R.G. Goodrich, *Fermi Surface of Antimony: Radio-Frequency Size Effect*, Phys. Rev. B **4**, 1033 (1971).

[110] M.P. Vecchi and M.S. Dresselhaus, *Temperature Dependence of the Band Parameters of Bismuth*, Phys. Rev. B **10**, 771 (1974).

[111] M.S. Dresselhaus and J.G. Mavroides, *Observation of Interband Transitions in Antimony*, Phys. Rev. Lett. **14**, 259 (1965).

[112] F. Jona, *Low-Energy Electron Diffraction Study of Surfaces of Antimony and Bismuth*, Surf. Sci. **8**, 57 (1967).

[113] V. Anishchik, L.M. Falicov, and F. Yndurain, *Electronic Surface Properties of Group V Semimetals*, Surf. Sci. **57**, 375 (1976).

[114] L.S. Lerner, K.F. Cuff, and L.R. Williams, *Energy-Band Parameters and Relative Band-Edge Motions in the Bi-Sb Alloy System near the Semimetal-Semiconductor Transition*, Rev. Mod. Phys. **40**, 770 (1968).

[115] H.B. Michaelson, *The Work Function of the Elements and its Periodicity*, J. Appl. Phys. **48**, 4729 (1977).

[116] L.M. Falicov and F. Yndurain, *Model Calculation of the Electronic Structure of a (111) Surface in a Diamond-Structure Solid*, J. Phys. C: Solid State Phys. **8**, 147 (1975).

[117] T. Greber, T.J. Kreutz, and J. Osterwalder, *Photoemission above the Fermi Level: the Top of the Minority d Band in Nickel*, Phys. Rev. Lett. **79**, 4465 (1997).

[118] M.G. Priestley, L.R. Windmiller, J.B. Ketterson, and Y. Eckstein, *De Haas-van Alphen Effect and Fermi Surface in Arsenic*, Phys. Rev. **154**, 671 (1967).

[119] S.G. Davison and J.D. Levine, *Surface States*, Vol. 25 of *Solid State Physics: Advances in Research and Applications*, ed. by H. Ehrenreich F. Seitz, and D. Turnbull, Academic Press (New York, London), 1970.

[120] I. Tamm, *Über eine mögliche Art der Elektronenbindung an Kristalloberflächen*, Z. Phys. **76**, 849 (1932).

[121] W. Shockley, *On the Surface States Associated with a Periodic Potential*, Phys. Rev. **56**, 317 (1939).

[122] S.D. Kevan, N.G. Stoffel, and N.V. Smith, *Spin-Orbit Effects on the Bulk Penetration and Energy Shift of Tamm States on Cu(001) and Ag(001)*, Phys. Rev. B **32**, 4956 (1985).

[123] J. Braun, J.P. Toennies, and G. Witte, *A SPALEED Structural Study of Cesium Adsorption on Stepped Copper Surfaces Cu(211) and Cu(511)*, Surf. Sci. **340**, 265 (1995).

[124] V. Marsico, M. Blanc, K. Kuhnke, and K. Kern, *Discrete Row Growth at Vicinal Surfaces*, Phys. Rev. Lett. **76**, 94 (1997).

[125] R.K. Kawakami, E.J. Escorcia-Aparicio, and Z.Q. Qiu, *Symmetry-Induced Magnetic Anisotropy in Fe Films Grown on Stepped Ag(001)*, Phys. Rev. Lett. **77**, 2570 (1996).

[126] H. Namba, N. Nakanishi, T. Yamaguchi, and H. Kuroda, *Electronic States Localized at Step Edges on Ni(7 9 11) Surfaces Studied by Angle-Resolved Photoelectron Spectroscopy*, Phys. Rev. Lett. **71**, 4027 (1993).

[127] J.E. Ortega, F.J. Himpsel, R. Haight, and D.R. Peale, *One-Dimensional Image State on Stepped Cu(100)*, Phys. Rev. B **49**, 13859 (1994).

[128] K. Flipse, *The Electronic Structure of Stepped Metal Surfaces*, PhD thesis, Rijksuniversiteit de Groningen, 1987.

[129] R. Matzdorf and A. Goldmann, *High-Resolution Angle-Resolved Photoemission from Cu(610)*, Surf. Sci. **400**, 329 (1998).

[130] H. Eckardt, L. Fritsche, and J. Noffke, *Self-Consistent Relativistic Band Structure of the Noble Metals*, J. Phys. F: Met. Phys. **14**, 97 (1984).

[131] S. Müller, A. Kinne, M. Kottcke, R. Metzler, P. Bayer, L. Hammer, and K. Heinz, *In-Plane Lattice Reconstruction of Cu(100)*, Phys. Rev. Lett. **75**, 2859 (1995).

[132] C. Cohen, A. L'Hoir, J. Moulin, D. Schmaus, M. Sotto, J.-L. Domange, and J.-C. Bouillard, *Study of Atomic Relaxations on Clean and Oxygen Covered (100), (410), and (510) Copper Surfaces by Channeling*, Surf. Sci. **339**, 41 (1995).

[133] Private Communication between J.E. Ortega and D. Purdie, 1993.

[134] J. Wollschläger, *Simple Analysis of Spot Splitting due to Diffraction at Surfaces with Atomic Steps*, Surf. Sci. **363**, 103 (1997).

[135] M. Henzler, *Quantitative Evaluation of Random Distributed Steps at Interfaces and Surfaces*, Surf. Sci. **73**, 240 (1978).

[136] F. Theilmann, R. Matzdorf, G. Meister, and A. Goldmann, *Influence of Surface Structural Disorder on Line Widths in Angle-Resolved Photoemission Spectra*, Phys. Rev. B **56**, 3632 (1997).

[137] X.Y. Wang, X.J. Shen, R.M. Osgood, Jr., R. Haight, and F.J. Himpsel, *Observation of Lateral Superlattice Effects on Stepped Cu(001)*, Phys. Rev. B **53**, 15738 (1996).

[138] R. Smoluchowski, *Anisotropy of the Electronic Work Function of Metals*, Phys. Rev. **60**, 661 (1941).

[139] M.D. Thompson and H.B. Huntington, *Adatom Binding at the Surface Ledges of a Jellium Metal*, Surf. Sci. **116**, 522 (1982).

[140] L.C. Davis, M.P. Everson, R.C. Jaklevic, and W. Shen, *Theory of the Local Density of Surface States on a Metal: Comparison with Scanning Tunneling Microscopy of a Au(111) Surface*, Phys. Rev. B **43**, 3821 (1991).

[141] M.F. Crommie, C.P. Lutz, and D.M. Eigler, *Imaging Standing Waves in a Two-Dimensional Electron Gas*, Nature (London) **363**, 524 (1993).

[142] Y. Hasegawa and P. Avouris, *Direct Observation of Standing Wave Formation at Surface Steps Using Scanning Tunneling Microscopy*, Phys. Rev. Lett. **71**, 1071 (1993).

[143] A. Beckmann, K. Meinel, M. Heiler, C. Ammer, and H. Neddermeyer, *Influence of Randomly Distributed Surface Steps on Photoemission Lineshape*, Phys. Status Solidi B **198**, 665 (1996).

[144] A. Beckmann, K. Meinel, C. Ammer, M. Heiler, and H. Neddermeyer, *Asymmetric Peak Broadening in Photoemission of Surface States as a Consequence of Lateral Electron Confinement*, Surf. Sci. **375**, L363 (1997).

[145] F. Theilmann, R. Matzdorf, and A. Goldmann, *High-Resolution Photoemission Studies at Rough Cu(111) Surfaces: the Influence of Defect Scattering and Disorder-Dependent Dephasing Processes*, Surf. Sci. **420**, 33 (1999).

[146] W. Chen, V. Madhavan, T. Jamneala, and M.F. Crommie, *Scanning Tunneling Microscopy Observation of an Electronic Superlattice at the Surface of Clean Gold*, Phys. Rev. Lett. 80, 1469 (1998).

[147] J. Frohn, M. Giesen, M. Poensgen, J.F. Wolf, and H. Ibach, *Attractive Interaction Between Steps*, Phys. Rev. Lett. **67**, 3543 (1991).

[148] M. Giesen, *Step-Step Interaction Energy on Vicinal Copper Surfaces*, Surf. Sci. **370**, 55 (1997).

[149] S. Singh, *Kronig-Penney Model in Reciprocal Space*, Am. J. Phys. **51**, 179 (1983).

[150] O. Sánchez, J.M. García, P. Segovia, J. Alvarez, A.L. Vásquez de Parga, J.E. Ortega, M. Prietsch, and R. Miranda, *Lateral Confinement of Surface States on Stepped Cu(111)*, Phys. Rev. B **52**, 7894 (1995).

[151] X.Y. Wang, X.J. Shen, and R.M. Osgood, Jr., *Surface Electron Motion near Monatomic Steps: Two-Photon Photoemission Studies on Stepped Cu(111)*, Phys. Rev. B **56**, 7665 (1997).

[152] G. Hörmandinger and J.B. Pendry, *Interaction of Surface States with Rows of Adsorbed Atoms and other One-Dimensional Scatterers*, Phys. Rev. B 50, 18607 (1994).

[153] B.G. Briner, P. Hofmann, M. Doering, H.-P. Rust, E.W. Plummer, and A.M. Bradshaw, *Observation of Interfering Bloch Waves*, Europhys. Lett. **39**, 67 (1997).

[154] R.S. Williams, P.S. Wehner, S.D. Kevan, R.F. Davis, and D.A. Shirley, *[ARUPS-Study of the Surface Electronic Structure of Stepped Cu(221)]*, Phys. Rev. Lett. **41**, 323 (1978).

[155] A.P. Shapiro, T. Miller, and T.-C. Chiang, *Angle-Resolved Photoemission Studies of a Surface State on a Stepped Cu(332) Surface*, Phys. Rev. B **38**, 1779 (1988).

[156] J.E. Ortega, S. Speller, A.R. Bachmann, A. Mascaraque, E.G. Michel, A. Närmann, A. Mugarza, A. Rubio, and F.J. Himpsel, *The Electron Wave Function at a Vicinal Surface: Switch from Terrace to Step Modulation*, Phys. Rev. Lett. (1999), submitted.

[157] P. Heimann, J. Hermanson, H. Miosga, and H. Neddermeyer, *d-like Surface State Bands on Cu(100) and Cu(111) Observed with Angle-Resolved Photoelectron Spectroscopy*, Phys. Rev. B **20**, 3059 (1979).

[158] P.L. Wincott, N.B. Brookes, D. S.-L. Law, and G. Thornton, *Relativistic Effects of the Surface Electronic Structure of Cu(001): Observation of a Spin-Orbit-Gap Surface State*, Phys. Rev. B **33**, R4373 (1986).

[159] D.W. Bullet, *Electron States at Cu Surfaces*, J. Phys. C: Solid State Phys. **14**, 4521 (1981).

[160] S.D. Kevan and D.A. Shirley, *High-Resolution Angle-Resolved Photoemission Studies of the $\overline{M}$-Point Surface State on Cu(001)*, Phys. Rev. B **22**, 542 (1980).

[161] R.G. Jordan, G.Y. Guo, and L.R. Masliah, *Surface States at the $\overline{M}$-Point on Cu(100)*, Solid State Commun. **99**, 73 (1996).

[162] A. Beckmann, C. Ammer, K. Meinel, and H. Neddermeyer, *The Modification of the $\overline{M}$-Point Tamm State of Cu(001) at the Corresponding Vicinal Faces*, Surf. Sci. **432**, L589 (1999).

[163] S.T. Inoue and J. Yamashita, *Electronic Structure of Metallic Beryllium*, J. Phys. Soc. Japan **35**, 677 (1973).

[164] E.W. Plummer and J.B. Hanooo, *The Surfaces of Beryllium*, Prog. Surf. Sci. **46**, 149 (1994).

[165] N.E. Alekseevskii and V.I. Nizhankovskii, *Investigation of Coherent Magnetic Breakdown*, Adv. Sci. Techn. USSR (Engl. Transl.), ed. by A.S. Borovik-Romanov, MIR Publ. (Moscow), 1985.

[166] M.Y. Chou, P.K. Lam, and M.L. Cohen, *Ab Initio Study of Structural and Electronic Properties of Beryllium*, Phys. Rev. B **28**, 4179 (1983).

[167] E. Jensen, R.A. Bartynski, T. Custafsson, E.W. Plummer, M.Y. Chou, M.L. Cohen, and G.B. Hoflund, *Angle-Resolved Photoemission Study of the Electronic Structure of Beryllium: Bulk Band Dispersion and Many-Electron Effects*, Phys. Rev. B **30**, 5500 (1984).

[168] E. Jensen, R.A. Bartynski, T. Gustafsson, and E.W. Plummer, *Distortion of an Unoccupied Band in Be by the Electron-Plasmon Interaction*, Phys. Rev. Lett. **52**, 2172 (1984).

[169] P. Hofmann, K. Pohl, R. Stumpf, and E.W. Plummer, *Geometric Structure of Be($10\bar{1}0$)*, Phys. Rev. B **53**, 13715 (1996).

[170] P. Hofmann, R. Stumpf, V.M. Silkin, E.V. Chulkov, and E.W. Plummer, *The Electronic Structure of Be($10\bar{1}0$)*, Surf. Sci. **355**, L278 (1996).

[171] P. Hofmann, B.G. Briner, M. Doering, H.-P. Rust, E.W. Plummer, and A.M. Bradshaw, *Anisotropic Two-Dimensional Friedel Oscillations*, Phys. Rev. Lett. **79**, 265 (1997).

[172] B.G. Briner, P. Hofmano, M. Doering, H.-P. Rust, E.W. Plummer, and A.M. Bradshaw, *Charge-Density Oscillations on Be($10\bar{1}0$): Screening in a Non-Free Two-Dimensional Electron Gas*, Phys. Rev. B **58**, 13931 (1998).

[173] H.L. Davis, J.B. Haonoo, K.B. Ray, and E.W. Plummer, *Anomalous Interplanar Expansion at the (0001) Surface of Be*, Phys. Rev. Lett. **68**, 2632 (1992).

[174] N.A.W. Holzwarth and Y. Zeng, *Density-Functional Calculation of the Bulk and Surface Geometry of Beryllium*, Phys. Rev. B **51**, 13653 (1995).

[175] J.B. Hannon and E.W. Plummer, *Shear Horizontal Vibrotions at the (0001) Surface of Beryllium*, J. Electron Spectr. Rel. Phen. **64/65** , 683 (1993).

[176] E.V. Chulkov, V.M. Silkin, and E.N. Sbirykalov, *Surface Electronic Structure of Be(0001) and Mg(0001)*, Surf. Sci. **188**, 287 (1987).

[177] U.O. Karlsson, S.A. Flodström, R. Engelhardt, W. Gädeke, and E.E. Koch, *Intrinsic Surface State on Be(0001)*, Solid State Commun. **49**, 711 (1984).

[178] R.A. Bartynski, E. Jensen, T. Gustafsson, and E.W. Plummer, *Angle-Resolved Photoemission Investigation of the Electronic Structure of Be: Surface States*, Phys. Rev. B **32**, 1921 (1985).

[179] P.J. Feibelman and R. Stumpf, *Physics of the Be(0001) Surface Core Level Spectrum*, Phys. Rev. B **50**, 17480 (1994).

[180] L.I. Johansson, H.I.P. Johansson, J.N. Andersen, E. Lundgren, and R. Nyholm, *Three Surface-Shifted Core Levels on Be(0001)*, Pbys. Rev. Lett. **71**, 2453 (1993).

[181] M. Aldén, H.L. Skriver, and B. Johansson, *Deep Layer-Resolved Core-Level Shifts in the Beryllium Surface*, Phys. Rev. Lett. **71**, 2457 (1993).

[182] L.I. Johansson, P.-A. Glans, and T. Balasubramanian, *Fourth-Layer Surface Core-Level Shift on Be(0001)*, Phys. Rev. B **58**, 3621 (1998).

[183] L.I. Johannson and B.E. Sernelius, *Electron Mean Free Path in Be Metal*, 1994.

[184] P.T. Sprunger, L. Petersen, E.W. Plummer, E. Lægsgaard, and F. Besenbacher, *Giant Friedel Oscillations on the Beryllium (0001) Surface*, Science **275**, 1764 (1997).

[185] L. Petersen, P. Laitenberger, E. Lægsgaard, and F. Besenbacher, *Screening Waves from Steps and Defects on Cu(111) and Au(111) Imaged with STM: Contribution from Bulk Electrons*, Phys. Rev. B **58**, 7361 (1998).

[186] L. Petersen, P.T. Sprunger, P. Hofmann, E. Lægsgaard, B.G. Briner, M. Doering, H.-P. Rust, A.M. Bradshaw, F. Besenbacher, and E.W. Plummer, *Direct Imaging of the Two-Dimensional Fermi Contour: Fourier-Transform STM*, Phys. Rev. B **57**, R6858 (1998).

[187] T. Balasubramanian, E. Jensen, X.L. Wu, and S.L. Hulbert, *Large Value of the Electron-Phonon Coupling Parameter ($\lambda = 1.15$) and the Possibility of Surface Superconductivity at the Be(0001) Surface*, Phys. Rev. B **57**, R6866 (1998).

[188] S. LaShell, E. Jensen, and T. Balasubramanian, *Observation of Non-Quasiparticle Structure in the Photoemission Spectra from the Be(0001) Surface and Determination of the Electron Self-Energy*, Phys. Rev. B (1999), submitted.

[189] P.A. Lee, T.M. Rice, and P.W. Anderson, *Fluctuation Effects at a Peierls Transition*, Phys. Rev. Lett. **31**, 462 (1973).

[190] F. Zwick, H. Berger, I. Vobornik, G. Margaritondo, L. Forró, C. Beeli, M. Onellion, G. Panaccione, A. Taleb-Ibrahimi, and M. Grioni, *Spectral Consequences of Broken Phase Coherence in 1T-TaS_2*, Phys. Rev. Lett. **81**, 1058 (1998).

[191] T. Pillo, J. Hayoz, H. Berger, M. Grioni, L. Schlapbach, and P. Aebi, *Remnant Fermi Surface in the Presence of an Underlying Instability in Layered 1T-TaS_2*, Pbys. Rev. Lett. **83**, 3494 (1999).

[192] D. Purdie, I.R. Collins, H. Berger, G. Margaritondo, and B. Reihl, *Observation of a Fluctuating Charge-Density Wave in the Unoccupied Electronic Structure of $(TaSe_4)_2I$*, Phys. Rev. B **50**, 12222 (1994).

[193] E. Jensen and E.W. Plummer, *Experimental Band Structure of Na*, Phys. Rev. Lett. **55**, 1912 (1985).

[194] A.W. Overhauser, *Photoemission from the Charge-Density Wave in Na and K*, Phys. Rev. Lett. **55**, 1916 (1985).

[195] K. W.-K. Shung and G.D. Mahan, *Calculated Photoemission Spectra of Na*, Phys. Rev. Lett. **57**, 1076 (1986).

[196] A.W. Overhauser, *Comment on 'Calculated Photoemission Spectra of Na'*, Phys. Rev. Lett. **58**, 959 (1987).

[197] K. W.-K. Shung and G.D. Mahan, *Reply to Comment on 'Calculated Photoemission Spectra of Na'*, Phys. Rev. Lett. **58**, 960 (1987).

[198] J.C. Campuzano, H. Ding, M.R. Norman, M. Randeria, A.F. Bellman, T. Yokoya, T. Takahashi, H. Katayama-Yoshida, T. Mochiku, and K. Kadowaki, *Direct Observation of Particle-Hole Mixing in the Superconducting State by Angle-Resolved Photoemission*, Phys. Rev. B **53**, R14737 (1996).

[199] M.R. Norman, H. Ding, J.C. Campuzano, T. Takeuchi, M. Randeria, T. Yokoya, T. Takahashi, T. Mochiku, and K. Kadowaki, *Unusual Dispersion and Line Shape of the Superconducting State Spectra of $Bi_2Sr_2CaCu_2O_{8+\delta}$*, Phys. Rev. Lett. **79**, 3506 (1997).

[200] M.R. Norman and H. Ding, *Collective Modes and the Supereonducting State Spectral Function of $Bi_2Sr_2CaCu_2O_8$*, Phys. Rev. B **57**, R11089 (1998).

[201] Z.-X. Shen and J.R. Schrieffer, *Momentum, Temperature, and Doping Dependence of Photoemission Lineshape and Implications for the Nature of the Pairing Potential in High-T_c Superconducting Materials*, Phys. Rev. Lett. **78**, 1771 (1997).

[202] S.G. Louie and M.L. Cohen, *Superconducting Transition Temperatures for Weak and Strong Electron-Phonon Coupling*, Solid State Commun. **22**, 1 (1977).

[203] D. Purdie, M. Garnier, M. Hengsberger, and Y. Baer, *A Fundamental Limitation for uv-Photoemission from Solids at Low Temperature*, J. Electron Spectr. Rel. Phen. **101-103** , 223 (1999).

[204] B.A. McDougall, T. Balasubramanian, and E. Jensen, *Phonon Contribution to Quasiparticle Lifetimes in Cu Measured by Angle-Resolved Photoemission*, Phys. Rev. B **51**, 13891 (1995).

[205] P. Hofmann, Y.-Q. Cai, C. Grütter, and J.-H. Bilgram, *Electron-Lattice Interaction on α-Ga(010)*, Phys. Rev. Lett. **81**, 1670 (1998).

[206] T. Valla, A.V. Fedorov, P.D. Johnson, and S.L. Hulbert, *Many-Body Effects in Angle-Resolved Photoemission: Quasiparticle Energy and Lifetime of a Mo(110) Surface State*, Phys. Rev. Lett. **83**, 2085 (1999).

[207] S. Engelsberg and J.R. Schrieffer, *Coupled Electron-Phonon System*, Phys. Rev. **131**, 993 (1963).

[208] G. Grimvall, *Numerical Calculations on the Electron-Phonon System in Sodium*, Phys. Kond. Mat. **8**, 15 (1967).

[209] G. Grimvall, *New Aspects on the Electron-Phonon System at Finite Temperatures with an Application on Lead and Mercury*, Phys. Kond. Mat. **9**, 283 (1969).

[210] G. Grimvall, *Electron-Phonon Interaction in Metallic Systems*, lecture notes (*Troisième Cycle de la Physique en Suisse Romande*), EPF Lausanne, 1988.

[211] S.Y. Savrasov and D.Y. Savrasov, *Electron-Phonon Interactions and Related Physical Properties of Metals from Linear-Response Theory*, Phys. Rev. B **54**, 16487 (1996).

[212] A.B. Migdal, *Interaction between Electrons and Lattice Vibrations in a Normal Metal*, Sov. Phys. JETP **34**, 996 (1958).

[213] C. Hodges, H. Smith, and J.W. Wilkins, *Effect of Fermi Surface Geometry on Electron-Electron Scattering*, Phys. Rev. B **4**, 302 (1971).

[214] H. Höchst, P. Steiner, and S. Hüfner, *The Conduction Electron Hole Coupling in Beryllium Metal*, Phys. Lett. A **60**, 69 (1977).

[215] E. Jensen, private communication.

[216] R.A. Bartynski, R.H. Gaylord, T. Gustafsson, and E.W. Plummer, *Angle-Resolved Photoemission Study of the Surface and Bulk ELectronic Structure of Mg(0001) and Mg(11$\bar{2}$0)*, Phys. Rev. B **33**, 3644 (1986).

[217] G.M. Watson, P.A. Brühwiler, E.W. Plummer, H.J. Sagner, and K.H. Frank, *Two-Dimensional Band Structure of a Li Layer: Li/Be(0001)*, Phys. Rev. Lett. **65**, 468 (1990).

[218] G.M. Watson, *Electronic Properties of Lithium*, PhD thesis, University of Pennsylvania, Philadelphia, 1992.

[219] G.M. Watson, P.A. Brühwiler, H.J. Sagner, K.H. Frank, and E.W. Plummer, *Observation of a Discontinous Nonmetal-to-Metal Disorder-to-Order Transition in an Alkali Overlayer*, Phys. Rev. Lett. **50**, 17678 (1994).

[220] P.A. Brühwiler, G.M. Watson, E.W. Plummer, H.-J. Sagner, and K.-H. Frank, *The Surface Continuum in Inverse Photoemission*, Europhys. Lett. **11**, 573 (1990).

[221] K.B. Ray, J.B. Hannon, and E.W. Plummer, *An Experimental Study of Hydrogen Adsorption on Beryllium*, Chem. Phys. Lett. **171**, 469 (1990).

[222] K.B. Ray, X. Pan, and E.W. Plummer, *The Interaction of H with Be(0001): a Photoemission Investigation*, Surf. Sci. **285**, 66 (1993).

Acknowledgments

Honour to whom honour is due! First of all, I would like to thank my thesis supervisor, Professor Yves Baer, for the possibility to realize this thesis, for his steady encouragement, his ideas and enthusiasm, and all the discussions we had about physics and anything else.

Further, I would like to acknowledge Hans Beck, Stefan Hüfner, and Daniel Malterre for having accepted the task to referee my thesis work. During the past years, I profited much from invaluable correspondence with Alexander Menzel and Eminald Bertel (Innsbruck), René Matzdorf (Kassel), Enrique Michel (Madrid), Enrique Ortega (San Sebastian), Ward Plummer (Knoxville), Ralph Claessen (Augsburg), Piero Martinoli (Neuchâtel), and, in particular, with Andreas Beckmann (Halle) and Eric Jensen (Brandeis).
Much theoretical help and insight into the "way of thinking of a theorist" came from the 3rd floor of our institute, namely from Hans Beck and Raymond Frésard. They merit lots of acknowlegdments for all the questions I had about electronic correlations!
I am very pleased to thank the group members for the excellent atmosphere (inside and outside the institute) and for all the help necessary to accomplish this work: Pilar Segovia, Klaus Breuer (we had many debates about German 3rd division soccer teams), Oliver Gallus, Nicolas Paul, and especially Douglas "William S." Purdie and Michael Gunnar Garnier, who have, amongst others, the merit of having built up our spectrometer. Much thanks to Pascal Weibel and Marco Grioni for their "starting assistance" on the ResBIS, and Marco again for the development of the monochromator. I would like to thank furtbermore the staff of the beamline SU3 at L.U.R.E., especially to Giancarlo Panaccione and Christoph Grupp, for their help during the beamtimes, and Thorsten Pillo (Fribourg, now Neuchâtel) for all the discussions, not only about physics.
For the remainder of the acknowledgments, I apologize for switching to French.
Je tiens beaucoup à remercier ...

- Françoise Baer pour le soutien morale qu'elle apporte à notre chef d'équipe et pour toutes les soirées passées "chez les Baer" (les excellents petits plats ont été très appréciés!),

- Jacques Weber, Jean-Pierre Egger et toutes les équipes d'assistants des TPD pour la bonne ambiance qui y régnait toujours et pour les nombreux apéros,

- les ateliers d'électronique et de mécanique pour toutes les pièces fabriquées, modifiées (de maintes fois) et réparées, en particulier Christian Hêche, Daniel Varidel et André Cornu,

- les secrétaires et notre administrateur, Jean-Luc Duport, pour toute leur aide lors des démarches administratives nécessaires,

- les doctorants et les postdocs de cet institut pour la bonne collaboration,
- tous les amis qui m'ont accompagné pendant ces dernières années à Neuchâtel, ainsi que mes amis d'Allemagne, fidèles malgré la distance, et plus particulièrement: Jean-Marc et Stéphanie, Bertrand et Céline, Pascal "P9" et Isabelle, Pascal "P20", Gunnar et Carine, Roland et Diane, Pierre, Philippe, Alain et Sabine, Douglas, Pilar et Oscar, Thorsten et Daniela, Benny, Chefche, Hanno, Schlager, Ulrich, Ziegel, Markus, et André !

Last but not least, il y a "tonton" Stefan et mes parents que je remercie particulièrement pour leur soutien pendant toutes ces années, ainsi que mes beaux-parents Alain et Alexandra, et enfin, ... merci infiniment à

ma petite famille, Cynthia et Lucas, pour leur présence, pour leur amour et pour toute la joie qu'ils m'apportent chaque jour !

Curriculum Vitae

date of birth: 30.01.1968
place of birth: Saarbrücken/Germany
nationality: German
marital status: married

present address:
Institut de Physique
Université de Neuchâtel
1, Rue A.-L. Breguet
CH - 2000 Neuchâtel/Switzerland

phone: +41 32 718 2987
fax: +41 32 718 2901
e-mail: matthias.hengsberger@iph.unine.ch

July 1974 - June 1987	primary school and gymnasium Homburg/Saar maturity 1987
Oct 1987 - Dec 1988	military service
Oct 1988 - Mar 1995	studies of physics at the Universität des Saarlandes, Saarbrücken, including:
Oct 1993	Summer University for Plasma Physics, Max Planck-Institut für Plasmaphysik München - Garching
Sept 1992 - Jan 1995	diploma work in the group of Prof. Dr. S. Hüfner title: *Measurements on Au and WSe_2 by means of angle-resolved inverse photoemission and target-current spectroscopy.*
Mar 1995	physics diploma
May 1992 - Mar 1995	teaching assistant, Universität Saarbrücken
Apr 1995 - Aug 1995	research assistant in the group of Prof. Dr. S. Hüfner
since Sept 1995	in the group of Prof. Dr. Y. Baer, Université de Neuchâtel
Feb 2000	PhD thesis title: *Unusual aspects of surface electronic structure studied with photoelectron spectroscopy.* teaching assistant, Université de Neuchâtel

List of Publications

1996

1. Straub, Th., Fauth, K., Finteis, Th., Hengsberger, M., Claessen, R., Steiner, P., Hüfner, S., and Blaha, P.:

   Valence band maximum in the layered semiconductor WSe_2: application of constant-energy contour mapping by photoemission,

   Physical Review B **53**, R 16152-155 (1996).

1997

2. Finteis, Th., Hengsberger, M., Straub, Th., Fauth, K., Claessen, R., Auer, P., Steiner, P., Hüfner, S., Blaha, P., Vögt, M., Lux-Steiner, M., and Bucher, E.:

   Occupied and unoccupied electronic band structure of WSe_2,

   Physical Review B **55**, 10400-411 (1997); Erratum: Physical Review B **59**, 2461 (1999).

3. Medarde, M., Purdie, D., Grioni, M., Hengsberger, M., Baer, Y., and Lacorre, P.:

   A photoemission spectroscopy study of $PrNiO_3$ through the metal-insulator transition,

   Europhysics Letters **37**, 483-488 (1997).

4. Garnier, M., Breuer, K., Purdie, D., Hengsberger, M., Baer, Y., and Delley, B.:

   Applicability of the single impurity model to photoemission spectroscopy of heavy fermion Ce compounds,

   Physical Review Letters **78**, 4127-130 (1997);

   Reply to Comment of A. J. Arko and J. J. Joyce: *$CeSi_2$ photoemission spectra at 5meV resolution,*

   Physical Review Letters **81**, 1349 (1998).

5. Breuer, K., Messerli, S., Purdie, D., Garnier, M., Hengsberger, M., Baer, Y., and Mihalik, M.:

   Observation of a gap opening in FeSi with photoelectron spectroscopy,

   Physical Review B **56**, R 7061-64 (1997).

6. Garnier, M., Purdie, D., Breuer, K., Hengsberger, M., and Baer, Y.:

   Momentum resolved photoemission of the Kondo peak in an ordered Ce-containing alloy,

   Physical Review B **56**, R 11399-402 (1997).

1998

7. Garnier, M., Purdie, D., Breuer, K., Hengsberger, M., and Baer, Y.:
   Comparative photoemission study of Pt(111)($\sqrt{3} \times \sqrt{3}R30°$)Ce and Pt(111)(2 × 2)La,
   Physical Review B **58**, 9697-699 (1998).

8. Hengsberger, M., Purdie, D., Garnier, M., Breuer, K., and Baer, Y.:
   Observation of super-structure periodicity in angle-resolved photoemission from Cu(610),
   Surface Science **405**, L 491-496 (1998).

9. Purdie, D., Garnier, M., Breuer, K., Hengsberger, M., Baer, Y., Panaccione, G., Indlekofer, G., and Grupp, Ch.:
   Resonant photoemission from $CeNi_x$ (x=1, 2 and 5),
   Solid State Communications **230**, 799-803 (1998).

10. Breuer, K., Messerli, S., Purdie, D., Garnier, M., Hengsberger, M., Baer, Y.,Takahashi, T., Kasaya, M., and Takabatake, T.:
    Photoemission study of the Kondo insulator $Ce_3Bi_4Pt_3$,
    Europhysics Letters **41**, 565-570 (1998).

11. Garnier, M., Purdie, D., Breuer, K., Hengsberger, M., and Baer, Y.:
    High resolution photoemission from an ordered Ce/Be alloy,
    Physical Review B **58**, 3515-517 (1998).

12. Purdie, D., Hengsberger, M., Garnier, M., and Baer, Y.:
    An outlook for high-resolution uv-photoelectron spectroscopy of solids at low temperature,
    Surface Science **407**, L 671-675 (1998).

1999

13. Garnier, M., Purdie, D., Hengsberger, M., Breuer, K., and Baer, Y.:
    Photoemission from Ce alloys at high resolution,
    Physica B **259-261**, 1095-99 (1999)
    (Proceedings of the Conference on Strongly Correlated Electron Systems SCES, Paris, 1998).

14. Purdie, D., Garnier, M., Hengsberger, M., and Baer, Y.:
A fundamental limitation for uv-photoemission from solids at low temperature,
Journal of Electron Spectroscopy and Related Phenomena **101-103**, 223-226 (1999)
(Proceedings of Vacuum Ultra-Violet VUV-XII, San Francisco, 1998).

15. Grioni, M., Weibel, P., Hengsberger, M., and Baer, Y.:
Resonant inverse photoemission in 4f systems,
Journal of Electron Spectroscopy and Related Phenomena **101-103**, 713-719 (1999)
(Proceedings of Vacuum Ultra-Violet VUV-XII, San Francisco, 1998).

16. Hengsberger, M., Purdie, D., Segovia, P., Garnier, M., and Baer, Y.:
Photoemission study of a strongly coupled electron-phonon system,
Physical Review Letters **83**, 592-595 (1999).

17. Hengsberger, M., Frésard, R., Purdie, D., Segovia, P., and Baer, Y.:
Electron-phonon coupling in photoemission spectra,
Physical Review B **60**, 10796-802 (1999).

18. Segovia, P., Purdie, D., Hengsberger, M., and Baer, Y.:
Observation of spin and charge collective modes in one-dimensional metallic chains,
Nature (London) **402**, 504-507 (1999).